

Investigations on the fragmentation and ionization of endohedral fullerenes using synchrotron radiation

Inaugural-Dissertation

zur

Erlangung des Doktorgrades der Naturwissenschaftlichen
Fakultät der Justus-Liebig-Universität Gießen

vorgelegt dem

Fachbereich 07

(Mathematik und Informatik, Physik, Geographie)

der

Justus-Liebig-Universität Gießen

von

Dipl. Phys. Jonas Hellhund

Institut für Atom- und Molekülphysik
Gießen, 2015

Parts of the present thesis work have been published previously [1,2].

Dekan: Prof. Dr. Bernhard Mühlherr
Erstgutachter: Prof. Dr. Alfred Müller
Zweitgutachter: Prof. Dr. Stefan Schippers

Contents

1. Deutsche Zusammenfassung	7
2. Abstract	9
3. Introduction and definition of the project	10
4. Experimental techniques	16
4.1. Synthesis of Xe@C ₆₀	16
4.1.1. Modifications of the ion source	18
4.1.2. Modifications concerning the fullerene-deposition substrate	22
4.1.3. Using other starting substances for the synthesis	25
4.1.4. Changes in the synthesis / production process	26
4.1.5. Differences to the ALS-based synthesis apparatus	27
4.1.6. Mass analyzing a high-yield sample	28
4.1.7. Conclusion on the synthesis of Xe@C ₆₀	30
4.2. Measurements at synchrotron facilities	33
4.2.1. The merged-beams technique	33
4.2.2. The ion-photon beamline at the ALS	36
4.2.3. The endstation PIPE at PETRAIII	39
4.2.4. Ion beam preparation	42
4.2.5. Sample evaporation performance plots	46
5. Triple photoionization and photofragmentation of Xe@C₆₀	48
5.0.1. Endohedral excess cross section and absolute calibration	50
5.0.2. Previous measurements of double ionization of Xe@C ₆₀ ⁺	51
5.1. Triple ionization of Xe@C ₆₀ ⁺	53
5.2. Results for Xe@C ₅₈ ⁺⁴ products	54
5.3. Results for Xe@C ₅₆ ⁺⁴ products	56
5.3.1. Comparison with double ionization product channels	58
5.3.2. Comparing the Xe@C ₅₆ ⁺ and Xe@C ₅₈ ⁺ product channels	59
5.4. Closing discussion on the triple ionization	61
6. Double photoionization and fragmentation of fullerene anions Xe@C₆₀⁻	63
6.1. Double ionization of Xe@C ₆₀ ⁻ ions with fragmentation	65

6.2. Double ionization of Xe@C_{60}^- ions without fragmentation	68
6.3. Double ionization of C_{70}^- ions	70
6.4. Closing discussion of the results for fullerene anions	71
7. Photoionization and photofragmentation of $\text{Lu}_3\text{N@C}_{80}$	72
7.1. Ionization-threshold energy predictions	74
7.2. Photoreaction measurements of $\text{Lu}_3\text{N@C}_{80}$	75
7.2.1. Experimental conditions	76
7.2.2. Results for photon energies 280 to 330 eV	77
7.2.3. Ionization threshold shift	83
7.2.4. Comparison with other fullerene species	84
7.2.5. Results for higher photon energies	86
7.2.6. Comparison with $\text{Sc}_3\text{N@C}_{80}$ measurements	89
8. Summary and conclusions	91
9. Bibliography	97
A. Appendix	106

1. Deutsche Zusammenfassung

Deutscher Titel:

Untersuchungen zur Fragmentation und Ionisation endohedraler Fullerene durch Synchrotronstrahlung

Wirkungsquerschnitte für die Photoionisation und Photofragmentation der endohedralen Fullerene Xe@C_{60} und $\text{Lu}_3\text{N@C}_{80}$ durch Synchrotronstrahlung im Energiebereich zwischen extrem ultraviolettem Licht und weicher Röntgenstrahlung, gemessen mit der sogenannten ‚Photon-Ion merged-beams Methode‘, werden gezeigt. Ein Teil des dafür erforderlichen Xe@C_{60} -Materials wurde an der Produktionsapparatur synthetisiert, die im Gießener Institut für Atom- und Molekülphysik (IAMP) vorhanden ist. Eine Reihe von Modifikationen an Apparatur und Herstellungsmethodik ermöglichte eine Steigerung des endohedralen Anteils im Material um den Faktor 30.

Die Messungen mit Xe@C_{60} wurden an der Synchrotronlichtquelle ‚Advanced Light Source‘ (ALS) des Lawrence Berkeley National Laboratory (LBNL) in Berkeley durchgeführt. Die vorliegende Studie knüpft an vorhergehende experimentelle Forschung auf dem Gebiet von Einfach- und Doppelionisation von Xe@C_{60}^+ -Ionen sowie deren Fragmentationskanälen an und erweitert die Untersuchungen auf die Dreifachionisation sowie Fragmentation von Xe@C_{60}^+ -Ionen und auf die Doppelionisation sowie Fragmentation negativer Xe@C_{60}^- -Ionen im Energiebereich 60–150 eV. Relative Wirkungsquerschnitte wurden entweder direkt anhand von Absolutmessungen normiert oder indem sie an absolute Messdaten von regulären, d.h. nicht-endohedralen, Fullerenen in Energiebereichen angepasst wurden, wo nur der Fullerenkäfig, nicht aber das eingeschlossene Atom, zum Wirkungsquerschnitt beiträgt. Die vom eingeschlossenen Atom verursachte Überhöhung des Wirkungsquerschnitts wurde durch einen Vergleich zwischen den Spektren von endohedralen und ‚leeren‘ Fullerenen ermittelt. Die experimentellen Ergebnisse werden weiterhin mit bereits publizierten Ergebnissen für die Doppelionisation von Xe@C_{60}^+ verglichen.

1. Deutsche Zusammenfassung

Die relativen Wirkungsquerschnitte von $\text{Lu}_3\text{N}@C_{80}$ wurden an der Synchrotronlichtquelle PETRAIII des Deutschen Elektronen-Synchrotrons (DESY) in Hamburg gemessen. Dabei wurden markante Strukturen im Energiebereich 280–330 eV beobachtet, die mit der Kohlenstoff-K-Ionisationsschwelle zusammenhängen. Die Resonanzstrukturen wurden in sieben verschiedenen Reaktionskanälen analysiert und mit bereits bekannten Spektren anderer Fullerenpezies verglichen. Anders als bei $\text{Xe}@C_{60}$ konnten für $\text{Lu}_3\text{N}@C_{80}$ keine Hinweise auf die N-1s- und Lu-3d-Ionisationsschwellen der eingeschlossenen Atome in den Energiebereichen 390–435 eV und 1500–1700 eV gefunden werden. Die Kohlenstoff-K-Kante tritt in der Doppelionisation von $\text{Lu}_3\text{N}@C_{80}^{2+}$ um $\Delta E = (2.90 \pm 0.24)$ eV verschoben gegenüber ihrer Energie in der Doppelionisation von $\text{Lu}_3\text{N}@C_{80}^+$ auf. Diese Verschiebung wird anhand des unterschiedlichen Coulomb-Potentials der unterschiedlichen Ladungszustände erklärt. Mittels der Verschiebungsenergie wird auf einen äußeren Fulleren-Radius $R = (5.0 \pm 0.4) \times 10^{-10}$ m geschlossen. Messungen mit $\text{Sc}_3\text{N}@C_{80}$ ergibt sich die Vermutung, dass das eingeschlossene Molekül Lu_3N den gleichen Einfluss auf den C_{80} -Käfig ausübt, wie Sc_3N .

2. Abstract

Cross-section measurements employing the photon-ion merged-beam technique for photoionization and photofragmentation of ions of endohedral fullerenes Xe@C_{60} and $\text{Lu}_3\text{N@C}_{80}$ exposed to synchrotron-generated extreme ultraviolet light and soft x-rays are presented. A part of the required Xe@C_{60} material was synthesized with the production apparatus available at the Institute for Atomic and Molecular Physics (IAMP) in Gießen. A list of modifications to apparatus and production methods facilitated an increase in the endohedral yield by a factor of 30.

Xe@C_{60} measurements were carried out at the synchrotron facility Advanced Light Source (ALS) at the Lawrence Berkeley National Laboratory (LBNL) in Berkeley. The current study extends previous efforts on single and double ionization of Xe@C_{60}^+ as well as fragmentation channels towards triple ionization with fragmentation of Xe@C_{60}^+ and towards double ionization with fragmentation of negative Xe@C_{60}^- ions in the photon energy range 60–150 eV. The relative cross-section data were normalized to absolute measurements either directly or the relative cross sections were scaled to match absolute cross-section data of pristine fullerenes in the respective channels at energies where the encapsulated xenon does not contribute. The excess cross section due to the encapsulated atom is determined by comparison of pristine and endohedral fullerene. The experimental results are compared to previously published measurements for Xe@C_{60}^+ double ionization.

Relative cross-section measurements for $\text{Lu}_3\text{N@C}_{80}$ were carried out at the synchrotron facility PETRAIII of the Deutsches Elektronen-Synchrotron (DESY) in Hamburg. Prominent structures related to the carbon K-shell ionization threshold were observed in the energy range 280–330 eV. These resonance structures have been analyzed in seven product channels and are compared with previously known absorption spectra of several fullerene species. Unlike for Xe@C_{60} , no signatures of the encapsulated atoms have been found particularly searching for the N-1s and Lu-3d thresholds in the energy ranges 390–435 eV and 1500–1700 eV. The carbon K-shell threshold seen in double ionization of $\text{Lu}_3\text{N@C}_{80}^{2+}$ is shifted by $\Delta E = (2.90 \pm 0.24)$ eV with respect to the carbon K-shell threshold in double ionization of $\text{Lu}_3\text{N@C}_{80}^+$. The shift is explained by the difference in the Coulomb potentials of singly and doubly charged and $\text{Lu}_3\text{N@C}_{80}$. An outer endohedral fullerene radius $R = (5.0 \pm 0.4) \times 10^{-10}$ m is inferred. Comparison with $\text{Sc}_3\text{N@C}_{80}$ indicates that Lu_3N has an identical influence on the C_{80} behavior at the carbon K-shell as Sc_3N .

3. Introduction and definition of the project

The first technological usage of carbon¹ dates back to the ancient Elam and Sumer cultures [3] yet carbon keeps on surprising on a regular basis with a variety of new compounds discovered in the recent years. Due to its half-filled L shell, carbon exhibits a great versatility in how it bonds allowing carbon to form more compounds than any other element [4].

Carbon occurs in nature as diamond or graphite in pure native deposits and in a vast variety of compounds from minerals to the life-forming proteins and even in the highly symmetric form of fullerenes. The fullerenes C_{60} and C_{70} have been found in soot and flames [5] and from early on it was suspected that they are present in interstellar matter [6]. Lately, the ion C_{60}^+ has been identified as the carrier of two interstellar bands [7]. In meteors, pristine fullerenes [8] and even endohedral fullerenes [9] have been found. When including laboratory-made substances, the range of carbon modifications is extended to nanotubes, graphene sheets, the so-called fullerene peapods (ordered assemblies of fullerenes inside nanotubes) until recently even a C_{60} fullerene derivative with a heptagonal ring in addition to the otherwise solely prevailing hexagon and pentagon ring structures was synthesized and proven [10].

Among the range of carbon-based compounds, endohedral fullerenes are nanoscale systems that have received much attention in the last decade. Numerous ideas for applications ranging from medical usage [11–14] (such as in imaging or drug delivery) to their employment in devices for quantum computing [15] and the prospect of possibly finding novel fundamental effects [16–18] make their examination a focus of research.

Shortly after Kroto et al. had discovered fullerenes in 1985 [19], they found indications suggesting the existence of the endohedral compound $La@C_{60}$ [20]. The existence of such compounds has been confirmed by Kroto et al. several years later [21]. This finding has stimulated intense theoretical research in the field of endohedral fullerenes. One direction of this research has addressed the screening effects of the fullerene cage

¹ Starting from early bronze age, the purposeful production of charcoal for the metallurgical use in reducing copper ore in smelters is documented for the Elam, Sumer and surrounding Mesopotamian cultures.

on the electron or photon emission of an encapsulated atom [16–18, 22–30]. The common prediction of these screening models is a redistribution of photoionization resonance strengths from the cage to the encapsulated atom or vice versa. One of the predicted effects of such a redistribution are the oscillations of the photoionization cross sections of encapsulated atoms [16, 17].

In spite of the increasing number of theoretical studies, there are relatively few experimental measurements to compare with. The limited access to endohedral substances impeded experimental studies. First experimental results on photoionization of neutral metallofullerenes Ce@C_{82} and Dy@C_{82} in the gas phase were obtained by Mitsuke et al. [31, 32] in 2005. In photoionization experiments with Ce@C_{82}^+ and C_{82}^+ ions, a Gießen-Reno-Berkeley collaboration could demonstrate the excess cross section due to the presence of the encapsulated Ce atom compared to the empty-shell fullerene [33]: On top of the smooth, monotonically decreasing C_{82} cross section, a feature resembling the cerium-4d resonance in the energy range 115–140 eV was evident. The shape of the feature was closest to that of the 2+ charge state of cerium in this energy range but the endohedral-excess cross section appeared broadened and smoothed compared with that of the free Ce^{2+} ion. The identification of the cerium 4d resonance in the endohedral excess cross section was supported further in that it contains about 85% of the oscillator strength found for the free ion. While the photoionization measurements with the metallofullerene Ce@C_{82} confirmed the presence of an excess cross section due to the encapsulated cerium atom, the cross sections showed no signs of confinement oscillations. In further investigations on the photoionization of $\text{Sc}_3\text{N@C}_{80}^+$ ions, the same collaboration found an excess amplitude with a maximum at 38 eV associated with the presence of scandium [34–36]. However, the resonance is substantially broadened as well as smoothed and distinct structures observed for free scandium ions are absent in the measurements with $\text{Sc}_3\text{N@C}_{80}^+$ ions. Again, there was no sign of confinement oscillations in the photoionization cross sections. In the following the ongoing experimental progress in the field of endohedral fullerenes in return led to intensified theoretical efforts. While confinement resonances in the photoionization of endohedral atoms were already predicted in 1993 [16, 17] and intensely discussed, their existence was questioned again in 2010 [37].

Within the larger scheme of the long-term agenda of the Reno-Berkeley-Gießen collaboration, net single and double ionization of Xe@C_{60}^+ ions as well as their prominent fragmentation channels have been investigated, delivering a first answer to the question of the existence of confinement resonances: Kilcoyne et al. presented experimental data which suggested that the excess cross section originating from the encapsulated xenon atom is modulated due to the atom's confinement within the fullerene cage [38]. At the beginning of and simultaneously with the present thesis project, Phaneuf et al. have consolidated this finding with even more thorough measurements of double photoionization cross sections of Xe@C_{60}^+ of unprecedentedly low statistical uncertainty [1]. Along their experimental results there is an extensive discussion of a variety

3. Introduction and definition of the project

of theoretical models for the confinement oscillations. A further remarkable finding of that study is that a reaction channel with fragmentation of the carbon cage and the loss of two dimers C_2 exhibits the strongest endohedral cross section contribution.

Goals

Studying characteristic photoionization signatures of specific elements encapsulated in endohedral fullerenes as well as the modification of these signatures due to the chemical and physical environment using synchrotron radiation are the topic of the present experimental work. The scope of the current effort was to extend previous studies on photoionization of fullerenes [39–41] as well as endohedral fullerenes [1, 33–36, 38, 42] to new species or different photoreaction channels. Continuing the above mentioned efforts, one of the two primary goals of this doctorate project was to investigate triple ionization of $Xe@C_{60}^+$ on one hand and double ionization of negatively charged $Xe@C_{60}^-$ anions on the other hand.

The investigations on triple ionization of $Xe@C_{60}^+$ wanted to answer the questions: Is there an endohedral signature in the triple photoionization of $Xe@C_{60}^+$ ions? Does the excess cross section exhibit confinement oscillations? How do these oscillations compare to the observations for double ionization? Is the oscillator strength distributed among double and triple ionization of encapsulated xenon in the same proportions as it is distributed among double and triple ionization of free atomic xenon?

In contrast, the investigations on negatively charged ions $Xe@C_{60}^-$ started with the more fundamental questions if a sufficiently intense beam of ions can be generated and if this negatively charged endohedral fullerene species is stable enough to be used for measurements. Since measurements with anions of the pristine fullerene C_{60} had been possible [41], the idea was to look for an endohedral-excess cross-section contribution in the double ionization of negatively charged $Xe@C_{60}^-$. Which effects would the change of the sign have on a potential xenon-4d feature in this situation otherwise symmetric to that of the established double ionization of $Xe@C_{60}^+$? Would this new reaction channel show signs of confinement oscillations? How would these compare to the double ionization of the positively charged counterpart $Xe@C_{60}^+$ in terms of shape and in terms of absolute intensity?

As a necessary prerequisite for studying photoreactions of $Xe@C_{60}$, sufficient quantities of that endohedral substance needed to be acquired. Preceding efforts [38] had made clear that the concentration of the endohedral fraction within the used fullerene samples had to be increased drastically to facilitate measurements with sufficiently good statistics: For double photoionization channels of $Xe@C_{60}$, improved sample quality and the resulting higher levels of statistics were required to provide unambiguous experimental proof of the predicted confinement resonances. In the case of triple

ionization of Xe@C_{60}^+ or reactions of negatively charged ions, however, an increased sample quality was needed to even establish a first quantitative result. Consequently, the reliable and reproducible production of endohedral fullerene samples with an increased endohedral fraction was set as a subsidiary goal of this project.

Besides the investigations concentrating on Xe@C_{60} , a further primary goal was to extend the photoionization studies towards exploring another species of endohedral fullerenes looking for both endohedral excess and confinement oscillations. While the research experience with Xe@C_{60} and the results from the previous investigations allowed to pre-establish the scope of further experiments with Xe@C_{60} ions quite precisely, for other endohedral fullerenes to be investigated the situation was very open. First, an endohedral species had to be selected for the study. The choice of the specific endohedral fullerene substances to be investigated was determined by the availability of substance material and the energy range of the synchrotron light sources where the experiments could be conducted: An interesting endohedral fullerene system would contain atoms of an element for which a broad and intense cross section feature was predicted at an accessible (photon) energy. The heavier species $\text{Lu}_3\text{N@C}_{80}$ with a planar-trigonal rare-earth-element molecule encapsulated was chosen due to the suitable lutetium 3d ionization threshold at about 1500 eV. A central goal was to search for a signature of the encapsulated atoms in the photoionization cross section spectra, specifically a lutetium-3d threshold. If present, further questions would address the potential modifications of the spectral shape of the encapsulated atoms due to confinement. Besides the effect of the confinement on the encapsulated atoms, the $\text{Lu}_3\text{N@C}_{80}$ study also addressed the question how the carbon cage in turn is affected by the presence of the encapsulated atoms. For this purpose, investigations covering an energy range including the prominent carbon K-shell resonances appeared to be promising. How would the $\text{Lu}_3\text{N@C}_{80}$ behavior at the carbon-K threshold compare to other fullerene species?

3. Introduction and definition of the project

Overview of measurements

In this dissertation, the focus is on cross section measurements for photoionization and photofragmentation of endohedral fullerene ions Xe@C_{60}^- , Xe@C_{60}^+ , and $\text{Lu}_3\text{N@C}_{80}^{q+}$ ($q=1, 2, 3$). Table 3.1 gives an overview of the substances investigated. The Xe@C_{60} results are compared with the accompanying empty-cage spectra. The Xe@C_{60} measurements were carried out using the permanent end-station IPB (Ion-Photon Beam) [43,44] at beamline 10.0.1 [45] of the synchrotron ALS (Advanced Light Source) at the Lawrence Berkeley National Laboratory in Berkeley. The available photon energies ranged from 17 – 340 eV at this beamline.

The $\text{Lu}_3\text{N@C}_{80}$ measurements were carried out using the permanent end-station PIPE (Photon-Ion spectrometer at PETRAIII) [46] at the Variable Polarization XUV Beamline P04 [47] of the synchrotron PETRA III at DESY in Hamburg. At the time of the present experiment, photons with energies between 250 eV and (at the time of the experiment) about 2000 eV were available at this beamline. These energies are considerably larger than those that were previously available for photon-ion merged-beam experiments, e.g., for the above mentioned Xe@C_{60} studies.

Substance name	Molecular mass	Encapsulated particle	Origin of substance	Purity grade
C_{60}	720 u	none	commercial	99.5–99.99%
C_{70}	840 u	none	commercial	<0.5% *
Xe@C_{60}	~ 852 u	atom	own preparation	$\frac{1}{100000} - \frac{1}{2000}$
$^{136}\text{Xe@C}_{60}$	856 u	atom	own preparation	$\frac{1}{100000} - \frac{1}{2000}$
$\text{Sc}_3\text{N@C}_{80}$	1109 u	molecule	commercial	35%
$\text{Lu}_3\text{N@C}_{80}$	1499 u	molecule	commercial	35%

Table 3.1.: Fullerene substances that have been investigated within this project.

*: C_{70} was present as an admixture in C_{60} samples. The class of endofullerenes called trimetaspheres (such as $\text{Sc}_3\text{N@C}_{80}$) can be produced in a modified Krätschmer-Huffmann process after which they can be separated and purified due to their chemical properties [48]. This separation is not possible for the noble-gas containing endofullerenes (Xe@C_{60} etc.) because their chemical properties are identical to those of their pristine counterparts. As a consequence, a different production method is required to achieve improved yields of these noble-gas endofullerenes. One possibility is kinematic implantation (see section 4.1). An alternative approach is to squeeze Xe atoms into the C_{60} fullerene cage utilizing extremely high pressures [49].

Characteristic features of atoms in the photoionization cross sections were expected at the well-established xenon 4d giant resonance for Xe@C_{60} and in the vicinity of subshell ionization edges of carbon, nitrogen, and lutetium for $\text{Lu}_3\text{N@C}_{80}$. Accordingly, the respective excitation energies of these features had to be matched with the accessible photon energies. In particular, the range of photon energies available at the IPB endstation include the xenon 4d giant resonance at about 100 eV and the carbon K edge near 295 eV. The nitrogen K edge near 410 eV and some lutetium M edges above 1500 eV are in the photon energy range accessible at the PIPE endstation. The present measurements with Xe@C_{60} focussed on an energy range covering the whole region of the xenon 4d giant resonance and its surroundings while the $\text{Lu}_3\text{N@C}_{80}$ measurements concentrated mainly on the energy range of the carbon K-edge.

Layout

The layout of this dissertation is as follows: Chapter 4 details the development of the apparatus and methods used for the production of Xe@C_{60} and briefly introduces the experimental setups where the photoreaction measurements have been carried out. Chapter 5 presents and discusses the experimental results obtained for triple ionization of Xe@C_{60}^+ followed by the experimental results for negative ions Xe@C_{60}^- and their discussion in chapter 6. Chapter 7 deals with the experimental investigations of $\text{Lu}_3\text{N@C}_{80}$ and discusses the results. Chapter 8 finally provides a summary and conclusions.

4. Experimental techniques

4.1. Synthesis of Xe@C₆₀

This section deals with advances in the means and methods for producing endohedral Xe@C₆₀ fullerenes by ion implantation (also called kinematic synthesis) carried out in the laboratories of the Gießen-based IAMP. Some of the photoreaction measurements presented and discussed in chapters 5 and 6 were obtained using samples that were produced in Gießen. The basic principle of this kinematic method for producing endohedral fullerenes is to irradiate them with ions. In this respect, the aim is to implant the ions while keeping the fullerene cage intact. The general concept of this method was first published by Tellgman et al. [50] for implanting Li alkali metal atoms and by Shimshi et al. [51] for implanting He atoms. Kilcoyne et al. were the first to publish results of research work using this synthesis layout with xenon ions [38].

The design of the production apparatus and the synthesis of the first three batches of endohedral fullerene material are part of preceding efforts: The original setup and the first measurements are described extensively in previous M.Sc. theses [52, 53] and another study has dealt with investigating some of the parameters of the setup as well as with the production and analysis of 12 more sample batches [54]. Therefore, only a very compact description of the synthesis setup is provided here: Inside a vacuum chamber, fullerene vapor is emitted from an evaporation oven. The vapor travels to a cylindrical, rotating substrate where it deposits. In the course of the rotation, the deposited fullerenes pass through an ion beam and are irradiated. An ion thruster for space propulsion acts as a powerful ion source in the Gießen synthesis setup. The simultaneous evaporation and irradiation process is continued for period of hours to weeks until finally the product substance is collected from the substrate. A brief overview of the setup and synthesis operation are presented in figure 4.1.

Within the present doctorate project, a total of 33 sample batches of endohedral fullerene material have been produced. The endohedral fullerene samples were analyzed using mass spectrometry. The composition of some of the samples has been determined at the ion-beam test bench apparatus in Gießen and others have been analyzed at the atomic, molecular, and optical physics (AMO) endstation of beamline 10.0.1 at the ALS/LBNL (see section 4.2.2).

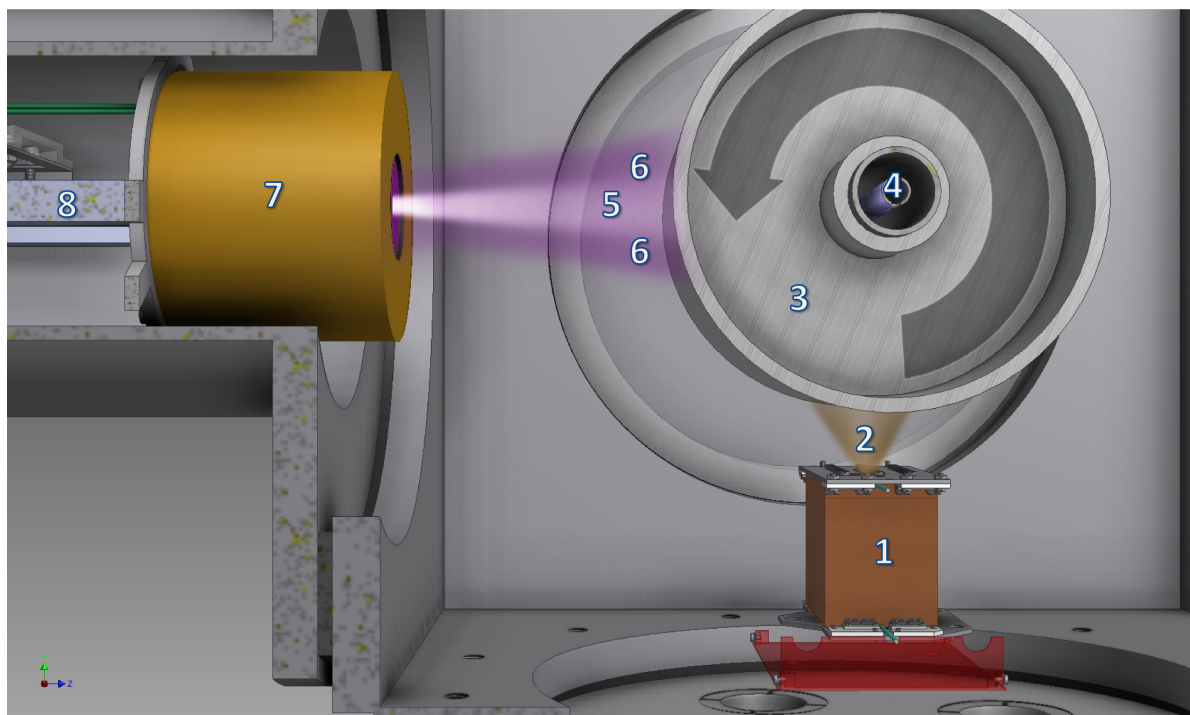


Figure 4.1.: Side view of the synthesis setup in the original realization [53] before the list of modifications had been applied. The image originates from the three-dimensional CAD model and illustrates the key components of the apparatus in the original state during endohedral-fullerene synthesis. The numbers have been added to identify components. Fullerenes are evaporated inside an oven **1**. The fullerene vapor **2** is deposited on the rotating substrate **3**. The substrate is attached to a drive shaft **4** which in turn is connected to a rotary feedthrough, a reduction gear, and a motor (not shown). The hollow coaxial drive shaft facilitated water cooling of the deposition substrate in the shown state. The fullerene layers deposited on the substrate are bombarded by a xenon ion beam **5, 6** emitted by the ion thruster **7** fixed to a water cooled support **8**. (The xenon ion beam consists of an inner, more intense **5** and of an outer, less intense **6** part.) Endohedral fullerenes are formed when a xenon ion penetrates and stays inside with the fullerene still intact.

During a period of three years, the fraction of endohedral fullerenes contained in a sample could be increased by a factor of 30 or more. A number of modifications both at the apparatus as well as of the production process were necessary to increase the endohedral fullerene yields. For the purpose of keeping this section compact, maintenance issues and minor improvements such as better pumping and more accurate pressure monitoring will not be dealt with.

4. Experimental techniques

The following list gives an overview of the most relevant modifications of methods and apparatus for the synthesis of endohedral fullerenes resulting in an improved sample quality and faster, more reliable production operation:

- Modifications at the ion source:
 - Adding a third, grounded grid to the thruster
 - Reducing the number of extraction holes from 37 to seven
- Modifications concerning the fullerene-deposition substrate:
 - Using a 'hot' substrate instead of a cooled substrate
 - Fast substrate rotation
- Using different starting substances for synthesis:
 - Sublimed-fullerenes powder
 - Using isotopically pure ^{136}Xe instead of natural xenon
- Changes in the endohedral fullerene synthesis process:
 - Starting up the evaporation before ion extraction

A separate technical report will deal with the details that are not discussed here.

4.1.1. Modifications of the ion source

The Gießen-based endohedral-fullerene synthesis setup uses a radio-frequency ion thruster (RIT) as a powerful ion source. A compact account on the functional principle of such an ion thruster is given in the following (aided by Fig. 4.2):

Xenon gas, which acts as a propellant, enters an insulating vessel(6) via a gas inlet (7). An electric generator(not shown) feeds radio-frequency signals to a coil(not shown) which is wrapped around that vessel(7). Three grids(1,2,3) are arranged in front of the aperture of the vessel and can be subjected to high voltage. Ignited by a spark from the grids, free electrons are continuously accelerated by the radio-frequency thus further ionizing the xenon present inside the vessel. A suitable configuration of potentials on the grids (e.g., +200 V at grid (1), -500 V at grid (2), and grid (3) grounded) allows for the extraction and focusing of the ions generated inside the vessel. For further details on the ion thruster, see reference [52]. The figure was created by Alban Voss [55].

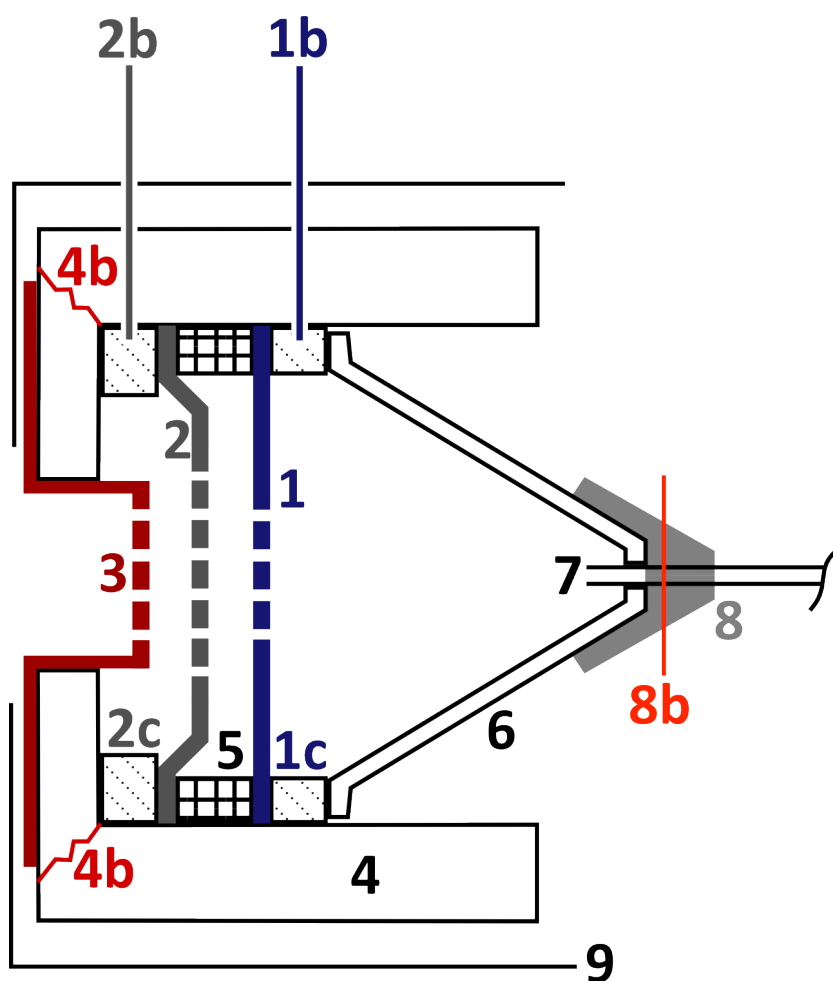


Figure 4.2.: Schematic cross-section drawing (side view) of the RIT ion thruster. **1** first high-voltage grid made of molybdenum with **1b** contact pin and **1c** contact ring, **2** second HV grid made from carbon with **2b** contact pin and **2c** contact ring, **3** grounded third grid made from steel, **4** thruster body with **4b** fissures, **5** insulating spacer, **6** plasma vessel, **7** gas inled, **8** flexible high-temperature putty fixing the gas inlet to the plasma vessel with **8b** a rupture, **9** grounded steel casing. (The items **4b** and **8b** will not be treated in this dissertation but in a separate technical report.)

Ion energy as a parameter for endohedral fullerene synthesis

Shimshi et al. [51] have reported an increased probability for ions to penetrate the fullerene cage when increasing the ion energy. On the other hand, along with increasing ion energy the ions start damaging the fullerenes irreversibly. For helium, the situation appears to be clear: Increasing the ion energy from 30 eV to 60 eV only increases the endohedral production yield but leaves the fullerenes intact. Further increasing

4. Experimental techniques

of the ion energy reduces the endohedral yield due to destruction of the fullerene cages starting from about 100 eV. For heavier noble gases, the situation is not as clear because the energy regions for implantation and destruction do overlap. Shimshi et al. have demonstrated this finding with neon as an example: At an ion energy of 130 eV, fullerene cages are destroyed but no neon is implanted. At 230 eV ion energy they have found endohedral fullerenes. In conclusion, the threshold for the neon ions to destroy a fraction of the fullerenes must be significantly lower than the threshold for implanting them into the fullerene. Another finding of their study is that both implantation and destruction with heavier noble gas atoms require higher ion energies. Since xenon is significantly heavier than neon, one would expect a much higher ion energy necessary to implant Xe into C₆₀.

Kilcoyne et al. [38] have reported to be using ion energies of 150 - 200 eV in 2010. Within the Reno-Berkeley-Gießen collaboration, our experience has shown that slightly lower ion energies (about 130 eV) can result in a higher endohedral production yield (see Phaneuf et al. [1] from 2013).

At the start of this study, the lowest voltage for ion extraction under stable conditions was 200 V. Ions extracted from the radio-frequency thruster at this energy would additionally have gained about 20 - 32 eV due to the plasma potential (see Modulbericht Scholz [54]). Accordingly, the **primary goal** of the thruster modifications was to enable ion extraction at lower energies.

The secondary goal of the thruster modifications was raised by the other finding mentioned above: For noble gases heavier than helium, implantation into fullerenes can only happen at energies that can also destroy the fullerene cages. It was unclear if the current of ions bombarding the substrate cylinder was so high that it would destroy significant fractions of the target fullerenes although the ion energy was comparatively low: One could imagine that intensified bombardment of the fullerenes with an increased Xe ion current could lead to increasing fullerene destruction. In this case, the time period between consecutive xenon ion impacts could be a crucial parameter. At the beginning of the present doctorate project, the minimum current output of the thruster in stable operation was two to three orders of magnitude higher than what Kilcoyne et al. had used. Consequently, the **secondary goal** of the thruster modifications was to enable the thruster to operate with an extended range of extractable ion currents including substantially smaller currents.

Adding a third, grounded grid

In a first attempt, a simple steel sheet with a 20 mm wide hole was fixed to the thruster cage at a distance of about 10 - 15 mm. This improvised third grid did hardly change the thruster behavior and the usage of the neutralizer was still required for operation at low extraction voltages.

In a second step, a proper third grid was added to the extraction grid array of the thruster. For this purpose, the whole extraction grid array had to be modified. The new third grid is the outermost grid and it is grounded, thus screening the potential of the second grid that otherwise attracts the ions extracted from the thruster. A consequence is that the extracted ions travel away from the thruster more quickly, effectively reducing the space charge in front of the thruster outlet. As a result, the problem of the hemispheric discharge (reported in [53]) does not occur anymore and there is less leakage current on the second grid during routine operation. Additionally, there is no need for further usage of the neutralizer (emitting free electrons reducing the effective space charge) anymore.

This measure has proven to be the crucial modification to allow for lower extraction voltages. It has enabled operating the synthesis apparatus at an extraction voltage as low as 80 V resulting in an effective ion energy of about 100 - 110 eV. This is lower than the expected threshold for Xe to penetrate the fullerene C₆₀.

Reducing the number of extraction holes from 37 to seven

To reduce the current of ions extracted from the thruster, using extraction grids with fewer holes is the straight forward approach because the extracted current scales almost linearly with the number of extraction holes (if the ion energy remains fixed). Since this modification was not carried out separately but together with a number of other modifications, its isolated influence is not clarified. However, it was observed that with 37 extraction holes, extraction currents were typically slightly less than 1 mA (at about 200 V extraction voltage) whereas with only seven holes extraction currents were in the range of about 35-50 μ A (at about 80 V extraction voltage).

Provided that the extraction geometry did not change, one can make the following estimate for the extracted ion current I in comparison with the extracted ion current in the initial state I_0 . The effect of reducing the extraction voltage U_0 to a lower value U can be described as

$$\frac{I}{I_0} = \left(\frac{U}{U_0} \right)^{\frac{3}{2}} \approx \left(\frac{110}{230} \right)^{\frac{3}{2}} \Rightarrow I \approx \frac{I_0}{3}.$$

Reducing the number of extraction holes from 37 to seven leads to a further reduction of the extracted ion current. A linear approach for the reduced extraction current I_{7h}

4. Experimental techniques

for seven holes in comparison with the original extraction current I_{37h} for 37 holes delivers

$$I_{7h} \approx \frac{7}{37} I_{37h} .$$

The combined estimate for the reduction of the extraction current results in

$$I_{\text{res}} \approx \frac{I_0}{3} \cdot \frac{7}{37} = \frac{950}{3} \cdot \frac{7}{37} \mu\text{A} \approx 60 \mu\text{A}$$

The estimated current for the reduced voltage and the reduced number of extraction holes is slightly higher than the observed current. This outcome is satisfactory given the simplicity of the estimate. More subtle effects such as the voltage-dependent deformation of the plasma meniscus or the voltage setting of the focusing grid at the center of the grid array were neglected. Considering that the thruster was designed for substantially higher extraction voltages of about 1000–2000 V, the amount of ion current extractable at a very low extraction voltage like 80 V is satisfactory as well.

The downside of using fewer extraction holes is an increased amount of non-ionized propellant gas present in the volumes between the grids with the consequence of the thruster getting hotter during operation. After operation with seven holes it turned out that the first and second extraction grid sometimes become warped. At this time, high grid temperatures are the only explanation at hand for this deformation. Nevertheless the two modifications to the grid system are of crucial importance: All successful synthesis operations were carried out after reducing the number of extraction holes and adding a third grid to the thruster.

4.1.2. Modifications concerning the fullerene-deposition substrate

The fullerene vapor from the oven is deposited on the surface of the rotating cylindrical metal piece in the center of the main chamber of the apparatus (as shown in fig. 4.1). In the context of the present thesis, this metal cylinder is referred to as 'substrate' following the nomenclature of physical vapor deposition. The thin film of fullerene material that is deposited on the surface of the substrate acts as the target for the subsequent ion bombardment. Thus, substrate and target form a mechanical unit.

An electrical motor outside the synthesis chamber drives the rotation of the substrate. For this purpose, the substrate is fixed to a drive shaft. This drive shaft is connected to a rotary feedthrough which itself consists of another bearing-supported drive shaft and a planetary reduction gear. The motor is directly connected to the reduction gear.

Using a 'hot' substrate instead of a cooled substrate

Previously, the substrate cylinder of the synthesis apparatus had been kept at room temperature using water cooling. Saunders et al. [56] had proposed the so-called window mechanism to explain their observation that encapsulated atoms can leave their fullerene cages at high temperatures (e.g. 600° C) still significantly lower than the limit for temperature-driven bond breakup of the cages. They found that the residual substance consisted almost entirely of (still) intact fullerenes but at the same time most of the formerly encapsulated atoms could be extracted. In succession, Murry et al. [57] have presented a model to calculate the 'window energy'. Their approach proposes windows to form at the corners where the carbon rings are joining rather than the centers of the pentagon and hexagon carbon rings favored by Saunders et al. [58] in a later publication. Both groups of researchers have suggested that the window mechanism that assists encapsulated atoms in leaving a fullerene cage without breaking the cage might as well help bringing an atom to the inside of a fullerene cage without breaking the cage.

Consequently, using a hot substrate cylinder for the synthesis was the goal of the substrate modifications. The first step was simply not to use the substrate water cooling anymore. Together with the desired fast-paced rotation (described in the prior subsection), the high temperatures at the substrate resulted in many breakdowns of gaskets and bearings around the drive shaft of the substrate cylinder, sometimes quite early during a production run. To gain long-term stability of production runs, a major redesign of the substrate cylinder was inevitable.

The redesign of the substrate cylinder and its supporting structure aimed at low thermal capacity as well as weak thermal coupling to the chamber walls, thus allowing the substrate cylinder and the fullerene molecules deposited on its surface to be passively heated by the infrared radiation that the evaporation oven emits. The distance between oven and substrate cylinder ascertains that the substrate is not as hot as the oven so that the fullerene molecules on the substrate are subliming more slowly in comparison with the evaporation mass flow from the oven during production.

Using a hot substrate has proven to be crucial for the improvement of the synthesis of endohedral fullerenes.

Fast substrate rotation

With a higher mass output of the evaporation oven, a higher rotation speed of the substrate is desired. Putting it the other way around, if the oven output is constant and the substrate rotates at a higher speed, the freshly deposited layer is thinner when it is irradiated by the ion beam from the thruster. Increasing the rotation speed of the substrate results in the deposition of an increased number of layers (which are thinner). One can assume that a fullerene ion gets the bigger part of its ion irradiation dose while passing through the ion beam for the first time. Thereafter it moves past the evaporation oven again and is covered by further fullerenes depositing on the substrate. Consequently, an increased rotation speed of the substrate results in a reduced time an individual fullerene layer is directly irradiated. However, the substrate rotation speed does not affect the time elapsing between two consecutive ion impacts on an individual fullerene. The period of time between two consecutive ion impacts is depending on ion current intensity and density at the substrate. Summing up, an increased substrate rotation results in an increased number of thinner fullerene layers. Additionally, the irradiation duration per layer is reduced. The idea is to achieve a more homogeneous irradiation and a better dose distribution of the ion irradiation. The advantages of thin layers of target fullerenes for the kinematic synthesis have been discussed in depth by Campbell et al. [59, 60].

There have been two successive upgrades of the substrate actuation system aiming at higher rotation speeds. Before these, the maximum rotation speed of the substrate was 4.4 rpm. For the first upgrade, the former motor and gearbox have been replaced by a much larger motor and a new gearbox but the substrate holder was kept (see figure 4.3 right panel). This upgrade has increased the maximum rotation speed by a factor of 25, thus allowing for up to 109 rpm.

Soon after this first substrate-rotation speed upgrade, the mode of operation moved on to using a hot substrate and target. As a consequence, the bearings and gaskets of the substrate drive shaft were a lot hotter during operation. Under these production conditions, the Teflon-lined Viton gaskets only lasted a few hours of operation even at lower rotation speeds. A new type of vacuum lubricant based on so-called liquid Teflon was used at the gaskets around the drive shaft. The new lubricant slightly improved the conditions but the effect was not sufficient. To enable a reasonable gasket lifetime, a rotation speed of about 50 rpm was typically used in this configuration until the second and more fundamental modification had been carried out.

The second modification effort was more fundamental than the first and included designing a new substrate holder, drive shaft, and reduction gear. The new substrate holder cannot be water cooled unlike the original one. In the absence of the water cooling, a small motor and a low-friction rotary feedthrough can be used (see figure 4.3 left panel). As a result, the substrate can rotate with speeds of up to 160 rpm.

4.1.3. Using other starting substances for the synthesis

Sublimed fullerene powder

Looking to enhance the fullerene output of the evaporation oven, using C₆₀ prepared by sublimation was tested. In comparison to the non-sublimation fullerene powder, the sublimed fullerenes have a distinctly different appearance: While the non-sublimed substance looks like micro-crystalline powder, the sublimed substance is of a much finer granularity resulting in an almost oily 'greasiness'. Using sublimed fullerene as starting material, the evaporation oven output at a certain temperature was much higher and more predictable than with non-sublimed fullerenes. Following this test, only 99.99% pure sublimed C₆₀ powder was used. The finer granularity and the more homogeneous physical appearance of the sublimed fullerene powder might be a reason for the higher evaporation output.

For all C₆₀ manufacturers' products and purity levels that were employed in the endohedral-fullerene production, it was observed that heating (for sublimation) even at



Figure 4.3.: **Left panel:** The dual stage reduction gear together with the massive motor of the first upgrade fixed to the outside of the chamber flange. The drive shaft connects the gear unit with the substrate passing through a rotary feedthrough. **Right panel:** After abandoning the water cooling of the substrate, a small motor with a single-stage reduction gear are sufficient for rotation at higher speed.

4. Experimental techniques

comparatively low temperatures leads to the formation of some material insoluble in toluene left behind inside the oven. It appears that a small fraction of fullerene material disintegrates into soot at temperatures considerably lower than the temperatures of thermal disintegration. This finding is in agreement with what Saunders et al. [56] reported.

Using isotopic ^{136}Xe instead of natural xenon

Natural xenon consists of eight stable isotopes of which the most abundant, ^{132}Xe , accounts for only about 27%. Isotope masses range from 124 u to 136 u. Endohedral fullerenes $\text{Xe}@C_{60}$ prepared using natural xenon are spread out in mass according to the mass distribution of xenon isotopes. This can be observed, e.g., by mass spectroscopy. Using isotopically enriched xenon concentrates the intensity to a narrower mass range. The advantages of using ^{136}Xe for the synthesis of endohedral fullerenes have been described by Phaneuf et al. [1]. Figure 4.4 is an excerpt of this publication demonstrating the current increase of $\text{Xe}@C_{60}^+$ ions resulting from switching to ^{136}Xe . Furthermore, Phaneuf et al. [1] mention that the endohedral fullerene mass is further separated from C_{70} when using ^{136}Xe , thus allowing for using a lower mass resolution realized by larger analyzer-magnet slit widths which results in an increase of current. Three liters of ^{136}Xe with a purity of 99,92% have been used for the synthesis of endohedral fullerene samples Nos. 29 through 36.

4.1.4. Changes in the synthesis / production process

Starting up the evaporation before ion extraction

The evaporation oven deposits fullerene vapor on the substrate which is exposed to bombardment by xenon ions from the thruster. If the ion extraction is already in progress while the evaporation oven starts heating up, the substrate is blackened by the fullerenes but it is difficult, sometimes even impossible, to scrape the deposited and processed materials off the substrate. It appears that the fullerenes (or rather fullerene fragments of all sizes) are implanted into the surface of the substrate by the xenon ion impact. Consequently, hardly any sample material is produced in this mode of operation. This problem can be solved by beginning the production process with fullerene evaporation and waiting for about 30 minutes until a visible layer of fullerene material has deposited on the substrate before extracting ions.

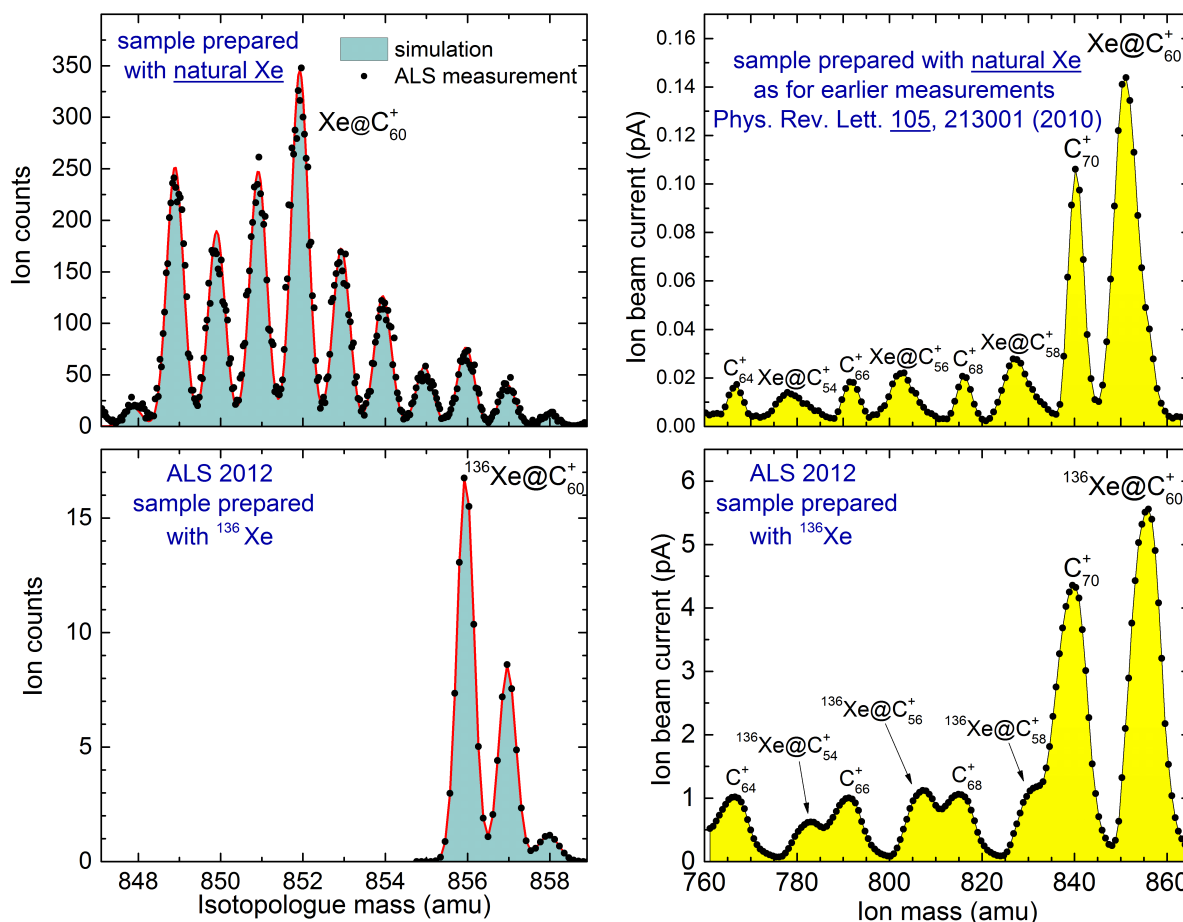


Figure 4.4.: Figure and caption from Phaneuf et al. [1]. Quoting Phaneuf et al.: “Ion beam mass spectra measured at high mass resolution (left panels), and low mass resolution (right panels). Upper panels are for samples prepared with a natural mixture of Xe isotopes, and lower panels for samples prepared with highly enriched ¹³⁶Xe. The three peaks in the lower left spectrum correspond to ¹³⁶Xe@C₆₀⁺ containing zero, one and two ¹³C atoms. The top right panel corresponds to the conditions for the merged-beams experiment of Kilcoyne et al. [38] and the lower right for the current measurements [1].”

4.1.5. Differences to the ALS-based synthesis apparatus

The Gießen-based apparatus for kinematic synthesis of endohedral fullerenes was inspired by a similar apparatus at the ALS [38] in Berkeley which has repeatedly produced samples with high endohedral fractions yielding several pA of positive ions extracted from an electron-cyclotron-resonance (ECR) ion source. Although the two setups have many similarities, there are also some differences looking at which might help to further improve the technique.

4. Experimental techniques

- For ion generation, the Gießen setup uses a space-propulsion ion thruster while the Berkeley setup uses one or two spark ion guns releasing pulsed ion beams.
- At the Berkeley setup, the residual gas inside the comparatively small synthesis chamber is almost entirely made up of ^{136}Xe which is not strongly pumped: The base pressure is in the 10^{-8} -mbar range before operation but during the endohedral fullerene synthesis the valve between chamber and pump is closed almost completely so that the chamber pressure rises to the 10^{-5} -mbar range due to the constant supply of ^{136}Xe . Since the type of ion guns used are fed by the residual gas, the presence of a stationary xenon atmosphere is required. In contrast, at the Gießen setup there is intense pumping and a more than ten times bigger volume. The base pressure is in the upper 10^{-7} -mbar range. During synthesis operation, the pressure rises to pressures between the upper 10^{-6} -mbar range and the to lower 10^{-5} -mbar range. Furthermore, the xenon is fed into the thruster directly, thus resulting in a dynamic atmospheric situation in which a the xenon flows from the thruster to the pumps continuously. Here, the residual gas is mostly air leaking into the process chamber.
 - ALS setup: Spark source, stationary chamber atmosphere: small and slow pressure changes, small pressure gradients inside the synthesis chamber, atmosphere contains 99.9% ^{136}Xe
 - Gießen setup: Ion thruster as ion source, dynamic atmosphere: big pressure gradients inside the synthesis chamber during production process, drastic pressure changes possible, atmosphere contains very little ^{136}Xe
- At the Gießen setup the mass flow of both the fullerene evaporation and the ion bombardment are stronger. While a production run in Berkeley takes one to three weeks, it is a couple of days in Gießen.

4.1.6. Mass analyzing a high-yield sample

Figure 4.5 shows a mass spectrum from a small test quantity of sample No. 26 (left panel) in comparison with a mass spectrum from previous work [53] (right panel). A $\text{Xe}@C_{60}^+$ ion current of 3.1 pA could be extracted from sample No. 26 whereas less than 100 fA could be extracted from early samples at best. This is an effective increase by a factor greater than 30 for extracting positive ions.

Using a full crucible load of sample No. 26 in an ECR ion source for the production of $\text{Xe}@C_{60}^-$ anions, 0.98 pA were measured for $\text{Xe}@C_{60}^-$ while C_{60}^- was 1.71 nA. At this time, the ratio of endohedral $\text{Xe}@C_{60}^-$ to pristine C_{60}^- was about one in two thousand. Since the ECR source and beam guides are designed for positive ions, it can be assumed

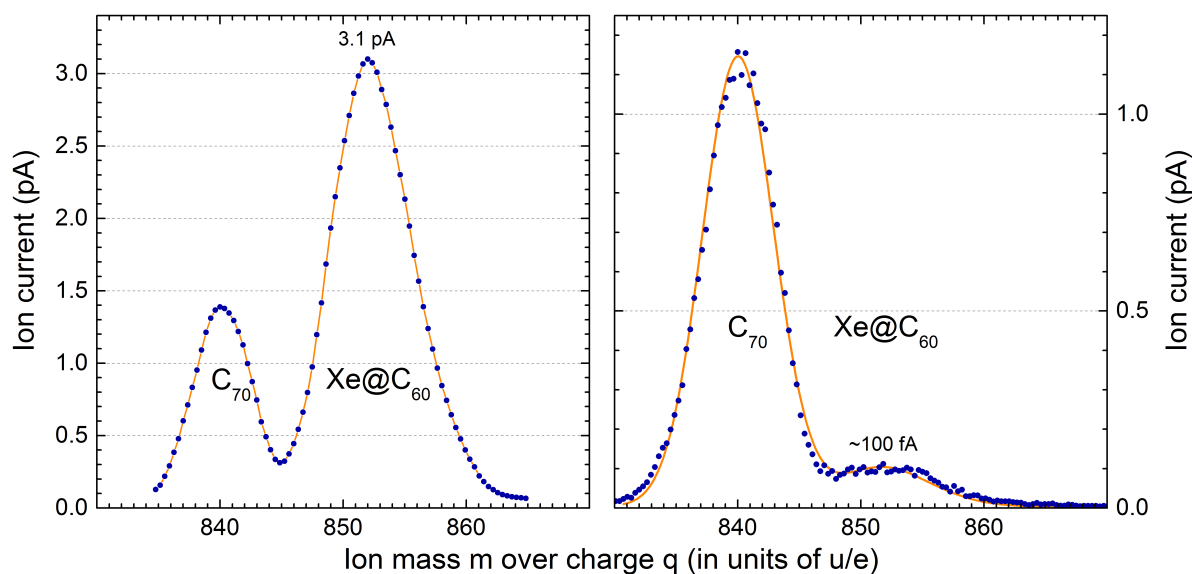


Figure 4.5.: Left Panel: Mass spectrum of sample No. 26 recorded using the IPB endstation at the ALS. Right panel: Figure taken from prior work [53] showing a mass spectrum of sample No. 3 recorded at the crossed-beams setup of the IAMP in Gießen. The ion current that could be extracted from sample No. 26 is more than 30 times bigger than the current extracted from sample No. 3.

that sample No. 26 would have yielded at least a factor three or five more current for positive ions.

Sample No. 26 turned out to be the best Gießen-made sample to be used in Berkeley so far but in fact it was only a part of the sample: The profile of the ion beam emitted by the thruster shows two zones with different intensities (see items 5 and 6 in figure 4.1). The part of sample No. 26 that was collected from the strongly bombarded central region consisted of very hard splinters and it was almost impossible to harvest this part. At the time immediately after removing the substrate with sample No. 26 from the synthesis chamber, only the part of the sample located outside the central region could be collected while the part in the central region remained on the substrate.

With an unconventional method that part of the sample could be collected later: The substrate cylinder was wrapped in aluminum foil and left in a laboratory storage for several weeks. Ambient air humidity or maybe some other atmospheric influence caused the black substance at the center to detach from the substrate cylinder after few weeks. However, the substance from the central part of the substrate was practically insoluble in toluene and, thus, probably only soot.

Which conclusions can be drawn from the observation that the part of the sample extracted from the central irradiation area was only soot while the part extracted from

4. Experimental techniques

the less irradiated area has a high endohedral fraction and is mostly made up of intact fullerenes?

- The ion energy (100 V extraction voltage + plasma potential = 120 - 132 eV) must have been about right for synthesis. Reducing the extraction voltage by 5 V appears to be still right (samples No. 28 and 33) but synthesis with only 90 V extraction voltage produced only samples with very small endohedral fractions (samples No. 25 and 35) which yielded hardly any extractable endohedral ion currents.
- The ion current in the central region was too intense but it could not be quantified. Only the total current on the substrate could be measured. The current was between 80 and 100 μA .
- Since there is intact fullerene material in one zone touching another zone of destroyed fullerenes only, the presence of a chain reaction spatially propagating the destruction of fullerenes can be excluded. A chain reaction would spread out through the whole substance body instead of staying well confined to the central region covering about 2 cm of the 10 cm wide substrate.

Efforts to produce more endohedral fullerene substance exhibiting the quality of No. 26 lead to mixed success: Synthesis operation with conditions that appeared to be identical to that of sample No. 26 sometimes resulted in good samples but it also resulted in samples with almost no endohedral fraction. However, several months after the production of the final sample (No. 36), it turned out that one of the backing pumps had a problem resulting in sub-second pressure bursts occurring at irregular time intervals. These bursts might have pushed shock waves of pressure backwards through the oil-diffusion pumps thus leading to contamination of chamber walls and substrate or to irregularities in thruster operation. The impact on the synthesis of samples cannot be estimated. This finding might be an explanation for the difficulties which were faced when attempting to reproduce sample No. 26.

4.1.7. Conclusion on the synthesis of Xe@C₆₀

The apparatus and technique for the kinematic synthesis of endohedral fullerenes has been improved by a list of modifications. As a result, the fraction of endohedral fullerenes of the samples produced could be increased by more than a factor of 30. An overview table of the endohedral samples produced can be found in appendix A.

Considering the high endohedral fraction of sample No. 26, one can conclude that the modifications of methods and apparatus for the synthesis made before its production were crucial for the improvement. Among these modifications, using a hot substrate, using a three-grid seven-hole extraction grid array that allows for ion energies of about

120–130 eV at the ion thruster, and starting the synthesis process by depositing a visible amount of target fullerene material on the substrate before extracting ions from the thruster are the most relevant modifications. It is out of question that the other changes made have also contributed to the improvement, especially in terms of stability of long-term operation.

The latest modifications include using highly enriched ¹³⁶Xe and sublimed fullerenes as starting substances for the synthesis process as well as very high substrate rotation speeds. Potential improvements of the endohedral yield resulting from these latest modifications could not be investigated because the quality of the latest samples was compromised due to a faulty pump and/or a short at the thruster (which will be detailed in a separate technical report).

Outlook for the synthesis of Xe@C₆₀

The production capabilities of the synthesis apparatus have been explored and the influence of operational parameters and methods has been investigated thoroughly. There is little room left for systematic investigations extending beyond the present study for the apparatus in its current state. Taking into consideration that two causes¹ for irregularities and instabilities have been identified and fixed recently, the synthesis of endohedral fullerenes could quite possibly yield high quality samples more predictably and further systematic studies of operational parameters would probably benefit from reduced statistical spread of sample parameters.

To take the search for an improved kinematic synthesis of endohedral fullerenes to the next level, however, it would be necessary to set up a completely new apparatus. Ideas for another synthesis apparatus are listed in the following:

- Monitoring the fullerene deposition on the substrate: The oven heating power, the fill amount, and the granularity of the C₆₀ powder determine the evaporation mass flow of the oven but the direct effects of varying these parameters could not be studied quantitatively so far. To devise means of controlling the fullerene evaporation rate more accurately, feedback from deposition monitoring is very helpful. Accurate control of the fullerene evaporation is a significant improvement when aiming at full reproducibility of the synthesis process.
- Using, e.g., an electrostatic cylindrical 90° deflector to guide only the desired singly-charged xenon ions to the substrate. The consequence could be a significant

¹A leakage current at the second thruster grid and the pressure bursts caused by one of the backing pumps which will be detailed in a separate technical report

4. Experimental techniques

reduction of neutral xenon atoms², ions in other charge states, and potential UV light³ reaching the substrate.

- Using a defocussing lens to achieve a more homogeneous substrate irradiation by redistribute a part of the intense ion current from the central substrate area to the less irradiated outer area.
- Using a smaller ion thruster, e.g., RIT 2.5 to maintain a more stable operation and better propellant efficiency: The currently used RIT 4.0 was designed to use a 137-hole grid but the best results were obtained employing a 7-hole grid. The RIT 2.5 is designed to use a 37-hole grid and, therefore, needs less propellant. Furthermore, it is designed to operate at smaller extraction voltages which are closer to the parameters of synthesis.
- Adding shutters between thruster and substrate as well as between evaporation oven and substrate to disentangle the operation of the different devices. This could be realized without requiring more room using light-weight rotatable parts made of steel sheet.
- Realizing the setup with a much smaller vacuum volume and oil-free pumping. This is not contradicting the usage of shutters: Switching to modern turbomolecular pumps instead of oil diffusion pumps allows to place pumps at horizontal flanges and upside down. As a consequence, a smaller main chamber could be used and one of the two sideways chambers would not be needed. This way oil contamination of the sample could be avoided and the base pressure in the chamber could be improved.

It appears imaginable that fullerene samples could be synthesized reliably with a further improved endohedral fraction with the next generation of a production apparatus of the kinematic type. To date, no fundamental limit for the endohedral fraction was evident. Maybe it will be possible to obtain macroscopic sample quantities with endohedral fractions of about one in 1000 yielding ion currents of 10 pA in the future.

²Xenon ions emitted from the thruster that became neutral due to charge exchange with non-ionized propellant or residual gas

³It is possible that the ion thruster emits UV light during operation

4.2. Measurements at synchrotron facilities

4.2.1. The merged-beams technique

For all photoionization and photofragmentation cross-section measurements presented in this work, the experimental setups both at the ALS and at DESY were operated using the so-called ion-photon "merged-beam technique" [61, 62]. The technique is named after its functional principle: A beam of the ions to be studied is merged coaxially with a photon beam. Photoreactions of the parent ions are studied by collecting the reaction products (e.g. higher charge states of the parent ions and fragmented ions in the case of molecular ions) in correlation to the photon energy of the incident light.

In an operation-focused picture, one can very briefly summarize the procedure along the stages which the ion beam passes: With a dipole bending magnet, the primary ion beam is mass selected and, thereafter, merged with the incoming photon beam using electrostatic deflection. In the case of the present setups, the ion beam and the photon beam are antiparallel in the merging region. Product ions of photon-ion interactions are separated from the primary beam employing a second dipole bending magnet. After leaving the interaction region, product ions are guided off the photon axis and transported to a single particle detector. A drift tube to which a bias voltage can be applied defines the interaction region. The voltage labeling of ions produced in this region can be used to distinguish photoion signal from inside and outside the interaction region. For normalization, the primary ion-current is collected in a Faraday cup and a calibrated photo diode registers the photon flux.

In conclusion, the present merged-beam measurements consist of four stages:

- Ion generation in a suitable ion source, ion extraction, and electrostatic acceleration.
- Mass selection and beam shaping of the parent ion with a dipole bending magnet, beam-defining slits, and electrostatic or magnetic lenses and steerers.
- Merging ions and photons: The ion beam is merged with the incoming photon beam using electrostatic or magnetic deflection. A fraction of the parent ions exposed to the photon beam reacts with photons. The overlap of beams is a crucial parameter for the reaction rate.
- Measurement of the unchanged fraction of the parent ion beam and detection of the product ions after separating them from the parent ions using a second magnet. Only a very small fraction (e.g. 3.7×10^{-8} at a photon energy of 292 eV in the case of single ionization of $\text{Lu}_3\text{N}@C_{80}^+$ [will be discussed in section 7.2.2]) undergoes a photoreaction.

4. Experimental techniques

Figure 4.7 in section 4.2.3 illustrates the procedure for the example of the setup at DESY that has been used for the measurements presented in chapter 7. A detailed description of the ion beam preparation is provided in section 4.2.4.

Determination of absolute cross sections

For the determination of absolute cross sections of a certain photoreaction, knowledge of the participating reactands and of the interaction region geometry is required: One has to know how many reaction partners etc. enter into the reaction and to what extent the beams overlap with respect to characteristics (such as energy dependence) of the entering reaction partners. A compact description of the measurement of absolute data points is given below.

The ions exposed to the photon beam can be ionized and/or fragmented. To determine cross section spectra $\sigma(E)$, the photon energy E is varied while the settings for the primary ion-beam remain unchanged. Simultaneously, product ions are counted as a function of the photon energy.

It is necessary to know the geometrical overlap of the two beams to be able to measure absolute cross sections. The beams can overlap in the whole region between the electrostatic deflector unit and the demerging magnet (partly even inside the magnet). For the purpose of defining the interaction length, the interaction region consists of a drift tube to which a potential of -1000 V to +1000 V can be applied. As a result, the ions produced inside the drift tube carry a different kinetic energy than the ions produced outside. At PIPE, the length of the drift tube is 50.0 cm and at IPB it is 29.4 cm. The product ions that have been voltage-tagged in this way are selected with the demerging magnet and transported to the detection unit.

At both ends of the drift tube, there are finely adjustable 4-jaw slits. These slits are used to cut the ion beam down to a size matching the photon beam profile (which can be as narrow as, e.g., 15 μm horizontally at PIPE). The overlap length z is defined by the length of the drift tube. To obtain the overlap factors in x and y direction along the z axis, translational slit scanners are employed at three different positions. (At the beginning, the center, and the end of the drift tube.) Performing a full set of slit scans can take several minutes.

The cross section $\sigma(E)$ can be determined from

$$\sigma(E) = \frac{R(E)qe^2Q(E)v_{ion}}{I_{ion}I_{\gamma}(E)F(E)}.$$

$R(E)$ is the reaction rate. The elementary charge e is multiplied with q accounting for the charge state of the primary ions. v_{ion} is the velocity of the primary ion traversing the

interaction region. $Q(E)$ corresponds to the quantum efficiency (number of electrons released per photon) of the photo diode. I_{ion} quantifies the electrical current of the primary ion beam. $I_{\gamma}(E)$ is the current which the photon beam releases inside the photo diode. $F(E)$, finally, is the geometrical overlap of the merged beams [61, 62].

In the actual practice, the determination of absolute data is a “static” mode of operation. That is, unlike for recording relative cross section spectra, the photon energy is not varied continuously but set to a certain value and it remains there for, e.g., 1000 s for counting of photons, parent ions, product ions, and so on. As a consequence, it is very time consuming to acquire absolute data and, hence, typically only few absolute points are acquired to scale relative cross sections to match the absolute cross sections and bridge the gaps between the absolute values.

The distinction made here between “static” and “dynamic” acquisition refers to the variation rate of the energy of incident photons.

Relative cross sections

Since the allocated beamtime at synchrotron facilities is limited, obtaining absolute cross sections is not always possible. There is a viable way to still draw quantitative conclusions from a set of non-absolute spectra: If all quantities with the exception of the form factors $F(E)$ can be determined for a set of data, and the assumption of identical conditions in terms of overlap is valid, the different spectra within that set are on identical scales. The spectra obtained in this fashion are not quantified in an absolute way but relative comparison is meaningful. Therefore, the spectra are termed relative cross sections. Consequently, the distribution of oscillator strength among the different product channels, for example, can be extracted from a set of relative cross section spectra although not on an absolute scale. The data presented in section 7.2 and part of the data shown in section 5.0.2 have been quantified in this way. The practical approach to obtain the **relative calibration** for those sets of spectra was the following: The photoreaction count rates at a single photon energy were measured in the various reaction channels within a short period of time during which the experimental conditions did not change. As stated above, it is a crucial requirement for determining relative cross sections with this method that the beam overlaps are the same in the different reaction channels. Especially for the product channels of the same primary ion, the overlap is the same.

Additionally, there is a **hybrid mode** which combines measuring relative cross-section spectra with applying a bias voltage to the interaction region like in absolute mode. The advantage of this hybrid mode is the suppression of background by utilizing the bias voltage to discard ions formed outside the interaction region. On the other hand, limiting the interaction length of the beams to the interaction region comes at the cost

4. Experimental techniques

of count rate. In a situation with a strong signal on top of a massive background the hybrid mode might be the better choice. In case of a small background, however, not applying a bias voltage to the interaction region might lead to better results.

This hybrid mode has been employed for measuring the spectra shown in section 5.1. These data as well as the data in section 5.0.2 could be put to an absolute scale by either directly using absolute points for reference or in the absence of absolute data by an indirect method which is described in chapter 5.0.1.

4.2.2. The ion-photon beamline at the ALS

The primary design goal of the undulator beamline BL10.0.1 [45] at the ALS was the capability for very high photon energy resolution (e.g. few meVs at 20 eV photon energy). Over the years, the growing experience and the beamline scientists continually working on the maintenance of the beamline (e.g. by the iterative optimization of undulator gap/energy tables for maximum flux) made the very high photon energy resolution accessible. There are three endstations at BL10.0.1 and the ion-photon beamline (IPB) is the endstation 10.0.1.1 in forward direction. A detailed description of the methods and experimental setup at the IPB endstation has been provided by Covington et al. [63]. Some modifications to the experimental layout have been detailed by Alna'Washi et al. [44] and more recent technological developments of the endstation have been discussed by Müller et al. [64].

Monochromator gratings

The monochromator of beamline 10.0.1 covers the photon energy range 17 – 340 eV [63]. There are three gratings covering different energy ranges: The so-called low-energy grating (LEG), the medium-energy grating (MEG), and the high-energy grating (HEG).

Modes of data acquisition and monochromator operation

IPB data acquisition features two modes for how the monochromator slits are operated when acquiring a photon-energy spectrum.

Fixed-slits mode: Entrance and exit slit of the monochromator stay in the same setting while the photon energy is varied. As a consequence, the resolution changes continuously from point to point.

Constant-resolution mode: Entrance and exit slit of the monochromator are moved in a way that the photon energy resolution stays the same when varying the photon energy. This mode has limits: For certain photon energies the mechanical range of the slits is not sufficient to allow for keeping a desired resolution constant for all energies.

Undulator gap compensation

The software controls of beamline 10.0.1 feature automated on-line undulator-gap adjustment so that the undulator provides the optimum photon flux over the whole range of a photon-energy scan. The undulator is ~ 10 m long and features two rows of magnets. The adjustment of the undulator gap requires the heavy undulator components to be actuated at micrometer levels repeatedly, resulting in substantial overhead adding to the measurement time. For time efficient measurements at maximum resolution it is possible to perform a series of narrow scans (≤ 0.5 eV photon energy range each) instead of a single scan spanning the photon energy range of interest. In that case the undulator gap is set to a fixed value providing the optimum photon flux at the midpoint of the energy range of the narrow scan. The on-line undulator-gap compensation is switched off to save the overhead time that otherwise was needed for gap adjustment during scans over wider photon energy ranges.

Photoreaction spectra extending over more than one grating

It is possible to merge photon-energy scan data from different gratings to one meaningful continuous photoreaction spectrum. Assembling scan data from different gratings is only valid if a list of requirements is met:

1. Data have to be acquired in *constant resolution* mode.
2. The photon energy resolution must be identical during photon energy scans operating the different monochromator gratings.

[The choice of a certain photon energy resolution can limit the total photon energy range that is covered by a set of photon energy scans carried out using different monochromator gratings: With the given monochromator geometry, the different monochromator gratings provide very different photon energy resolutions. Resolutions shared by two or three gratings might not be available for the full energy range of a grating. As a consequence, the photon energy range of the spectrum will probably be limited because by the chosen resolution setting.]

3. The ranges of the photon energy scans must have an overlap thus allowing one to merge the individual scans to one spectrum.

4. Experimental techniques

4. The data have to be corrected for dark counts, ion-induced background counts, artifacts, Doppler shift etc. independently before forming the joint spectrum.

The above requirements for merging data obtained using different monochromator gratings are formulated in the most stringent way. There are occasions, however, in which it is valid to merge data from different gratings although not all requirements have been met: In the special case of a cross section without structures or with only very broad structures, a compatible resolution (item 3) is not required as long as the photon flux is correctly used for normalization of the photoreaction signal. The issue of beam overlaps (item 1), however, is crucial for all cases except when *absolute data points* are available for the whole photon energy range.

Si-artifact correction

For normalization of both continuous relative spectra and absolute photoreaction data points, the photon flux is measured using a silicon photo diode. At a photon energy of about 100 eV, there is a dip in the sensitivity function of the diode because the silicon bulk absorbs part of the light due to the silicon L edge. Using this photon flux curve for normalization without correcting for the dip causes the occurrence of an artifact in the cross section spectra.

This 'Si artifact' was taken care of by measuring continuous cross sections of photoreactions of, e.g., C_{60}^- . The artifact can be identified unambiguously and corrections are applied restoring the known smooth cross section. Figure 4.6 shows the artifact correction at the example of $C_{60}^- \rightarrow C_{56}^+$ photoreactions.

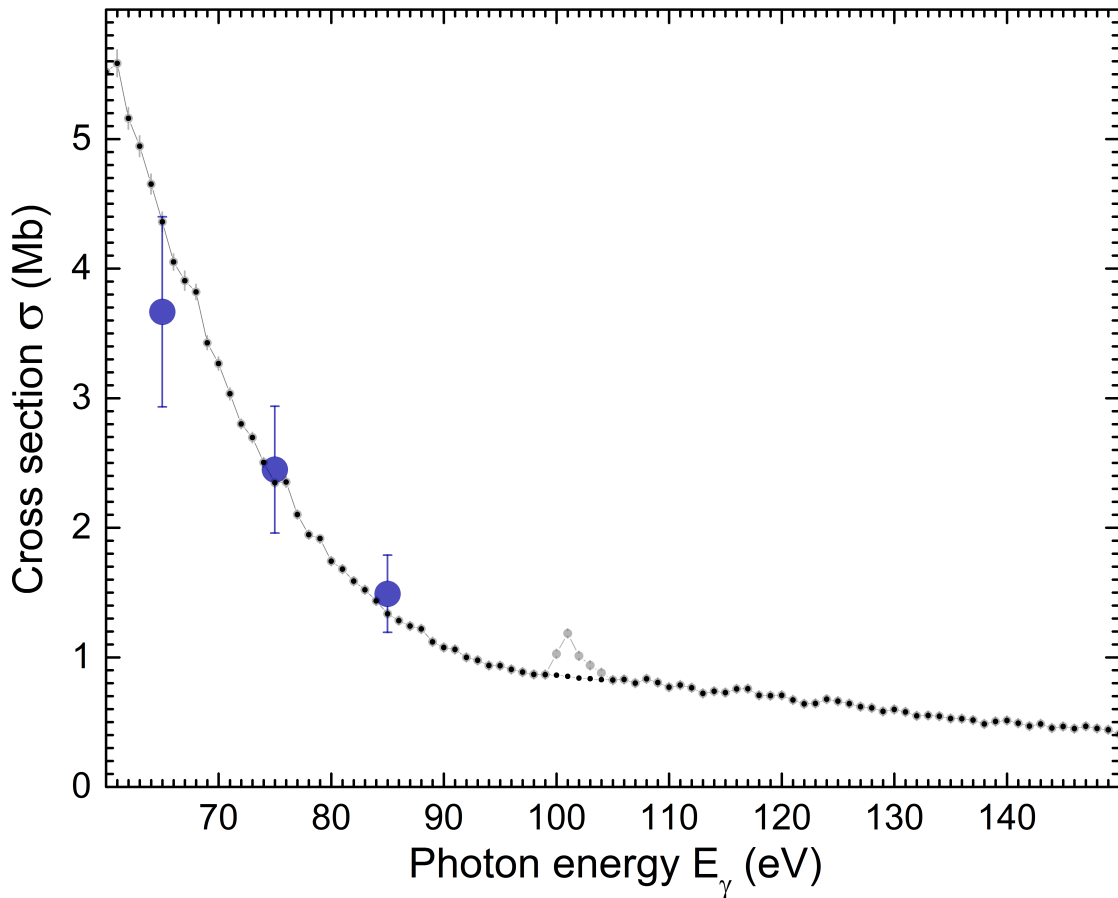


Figure 4.6.: Illustration of the normalization artifact that arises in cross-section spectra due to the silicon of the photo diode. As an example, the cross section for double photoionization with fragmentation $C_{60}^- \rightarrow C_{56}^+$ is shown. The artifact is visible at a photon energy of about 101 eV. The spectrum is shown before (solid gray circles with statistical error bars) and after (solid black circles with statistical error bars) applying the correction function. In addition, the absolute measurements (big, solid blue circles with statistical error bars) which were used for the normalization of the spectrum are shown.

4.2.3. The endstation PIPE at PETRAIII

The permanent end station PIPE is located at Beamline P04 of the PETRA III synchrotron of DESY in Hamburg. Beamline P04 was designed to reach an energy resolving power of 10000 while still providing 10^{12} photons per second. Beamline characteristics have been described by Viefhaus et al. [47]. Schippers et al. have provide a detailed description of the endstation PIPE [46].

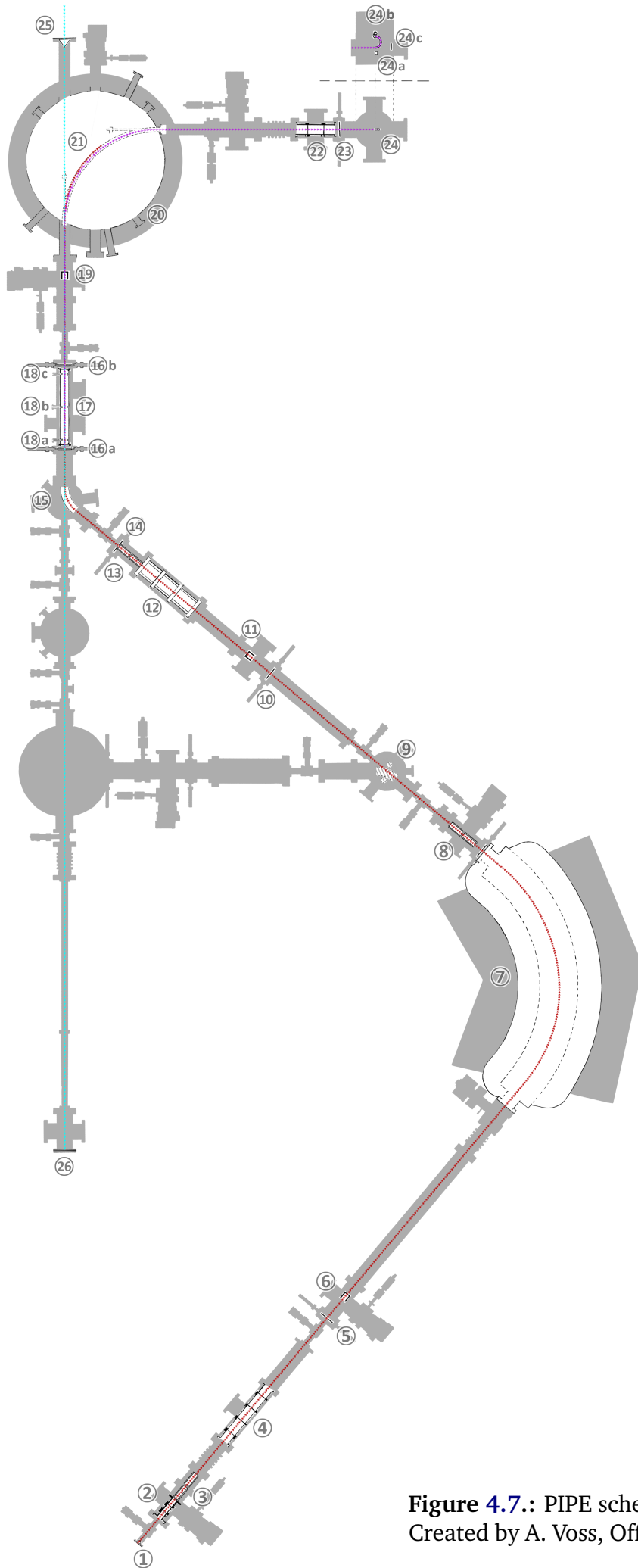


Figure 4.7.: PIPE schematics top view
 Created by A. Voss, Offenbach, 2015

Beamline components along the flight path of an ion

Figure 4.7 shows a schematic top view of the PIPE endstation layout. Key components are accompanied by numbers and drawn with black lines around white areas whereas the chamber walls are indicated with a solid gray area. The drawing does not show an ion source because several types of ion sources can be used at PIPE. The flight path of the parent ions is indicated by a red dotted line. A light cyan dotted line represents the photon beam. The trajectory of product ions is symbolized with a violet dotted line. The figure was created by Alban Voss⁴ on the basis of the available model drawings from a computer-aided-design program.

1. The ions leave the ion source and enter PIPE tubing
2. Einzel lens for beam focusing
3. Electrostatic steering of the beam
4. A five-element lens for focusing
5. 4-jaw slits in the first focus of the analyzing magnet
6. Retractable Faraday cup
7. Double-focusing dipole analyzer magnet for selecting the parent ions by mass-per-charge separation
8. Electrostatic steering
9. Retractable 40°-degree deflector for switching the ion path (not used in the present context)
10. 4-jaw slits in the second focus of the analyzing magnet
11. Retractable Faraday cup
12. Electrostatic triple-quadrupole lens
13. Electrostatic steering
14. 4-jaw slits
15. 50°-degree deflector merging the ion beam onto the photon-beam axis
16. Finely adjustable 4-jaw beam-defining slits which the ions pass through (a) before and (b) after moving through the drift tube 16
17. Drift tube that can be subjected to a potential
18. Translational x-y-profile slit scanners: (a) at the front, (b) in the center, and (c) at the back end of the drift tube
19. Retractable Faraday cup
20. Double-focusing dipole magnet for demerging parent ions and product ions

⁴Communication Designer, Offenbach am Main, Germany [55]

4. Experimental techniques

21. Faraday cup for collecting the parent ions: There are two chambers with individual pumping inside the demerging magnet. The circular outline in the drawing resembles the outer chamber whereas the inner chamber was realized using a bent tube. The wall of the inner magnet chamber is used as a Faraday cup that collects the parent ions. In the current status of the apparatus, the tube-based inner chamber has been replaced by new chamber which looks like a curved box (not shown).
22. Einzel lens
23. 4-jaw slits
24. In addition to the top view, the detector chamber is also shown in a side view to illustrate the arrangement of detectors inside (the dashed lines connect the side view with the corresponding part of the overall scheme). The detector chamber is equipped with (a) a Faraday Cup, (b) a highly sensitive single particle detector, and (c) a position-sensitive single-particle detector (not used in the present context).
25. Photons enter PIPE far downstream of the undulator
26. A calibrated photodiode registers the photon flux

4.2.4. Ion beam preparation

The following section describes the ion beam preparation, reaction, and transportation from the source (1) to the detector (24) during PIPE operation. The procedure described for $\text{Lu}_3\text{N}@C_{80}$ serves as an example for similar procedures for other ions as well as for operation of the IPB endstation. Numbers in brackets (n) refer to the respective beamline components displayed in Fig. 4.7.

For the preparation of $\text{Lu}_3\text{N}@C_{80}^{q+}$ ion beams, the sample material was introduced into the ion source (1) as a solid powder inside a small stainless-steel crucible. This crucible was inserted into a resistively heated oven which can reach temperatures above 1500°C at a heating power of about 35 W. The vapor that was generated from the sample powder was ionized by electron bombardment inside a permanent-magnet electron-cyclotron-resonance (ECR) source [65] operated at a potential of +6 kV. After extraction and acceleration of the ions, the ion beam was focused and steered by a series of electrostatic lenses and deflectors (2,3,4). A double-focusing dipole [analyzing] magnet (7) in combination with two four-jaw slits located in front (5) of and behind (10) the magnet (7) was used for the mass-over-charge selection of the primary ion species to be investigated.

In the first phase after the source chamber had reached operating pressure (better than 10^{-5} mbar), the inserted crucible loaded of sample material (containing 35% of

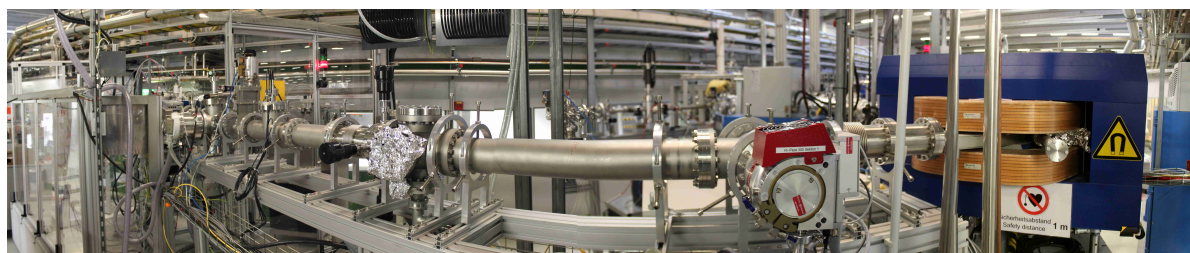


Figure 4.8.: PIPE from the ion source platform (on the left) to the analyzer magnet (see Fig. 4.7).

$\text{Lu}_3\text{N}@C_{80}$ and 65% of other fullerenes, mainly C_{60}) was heated with a low power (2.7 W) such that the crucible remained well below the sublimation temperature of C_{60} . This phase of constant low-power heating took several days during which unwanted volatile contaminants were removed from the sample material while leaving the endohedral component of the sample largely untouched. During this phase, a continuous ECR plasma discharge of argon as carrier gas was sustained to warm up and clean the chamber walls of the source as well as to condition the source for measurement operation. During this conditioning phase, the source chamber reached a base pressure of some 10^{-7} mbar.

In a second phase of source operation, the oven power was slowly increased and first weak beams of C_{60}^+ (which evaporates at lower oven temperatures than $\text{Lu}_3\text{N}@C_{80}$) were extracted from the ion source. The characteristic operating pressure inside the ion source then was in the lower 10^{-6} mbar region. The aim of this second phase was to obtain an ion beam with high intensity and narrow beam profile while maintaining long-term stability. Optimization of conditions for the extraction of the desired primary ion focused on both tuning the source conditions and the beam optics.

In all phases of operation, mass spectrometry was an important tool for monitoring the ion beam composition. Mass spectra of primary ions were obtained by measuring the primary ion current collected in a Faraday cup directly behind the analyzer magnet as a function of magnetic field strength. The mass spectrum shown in Fig. 4.9(a) was recorded after 50 hours of low-power outgassing and 12 hours of carefully powering up the source. At this time, with about 5 W heating power, the spectrum was dominated by a plethora of peaks from pristine light fullerene ions (C_{60}, C_{70}) and their fragments (C_{58}, C_{56}, \dots). The current of C_{60}^+ ions peaked at 160 pA. Under the specific conditions during this phase of ion-source operation, C_{60}^+ was about 30 times more abundant than $\text{Lu}_3\text{N}@C_{80}^+$ although the sample contained about 35% of $\text{Lu}_3\text{N}@C_{80}$ and probably about 50% of C_{60} . Over time, the balance shifted towards higher masses when the lighter molecules had been evaporated selectively off the sample and the oven temperature was increased further.

4. Experimental techniques

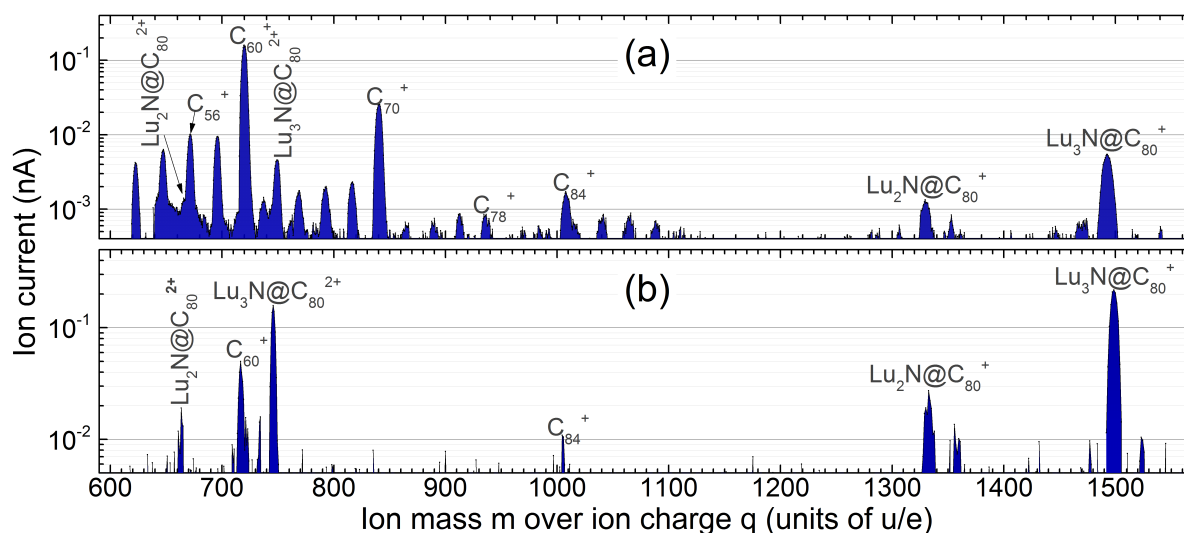


Figure 4.9.: Two primary-ion mass spectra of the same sample at different times: (a) recorded after 50 h of outgassing followed by 12 h of slowly increasing the heating power of the oven to 5 W, (b) recorded 48 h after (a) at a heating power of 12.75 W. The spectra have been measured using two different Faraday cups. With the cup [(18) in figure 4.7] used for the measurement displayed in panel (b) the statistical-noise background is higher than for the other cup [(11) in figure 4.7].

Fig. 4.9(b) depicts a mass spectrum from the same sample but 48 hours later after a further continuous increase of the oven power to 12.75 W. Now $\text{Lu}_3\text{N@C}_{80}^+$ dominated the spectrum with an ion current of about 220 pA. The second-strongest peak originated from doubly charged $\text{Lu}_3\text{N@C}_{80}^{2+}$ ions. Higher charge states, i.e., 3+ and 4+, were also found (not shown in Fig. 4.9). In addition to the various fragments and charge states of $\text{Lu}_3\text{N@C}_{80}$, there are also peaks matching m/q of $\text{Lu}_2\text{N@C}_{80}^+$ and $\text{Lu}_2\text{N@C}_{80}^{2+}$ but at this time it remains unclear whether $\text{Lu}_2\text{N@C}_{80}$ exists in the initial powder or is formed in the plasma. Obviously $\text{Lu}_2\text{N@C}_{80}^+$ and $\text{Lu}_2\text{N@C}_{80}^{2+}$ are sufficiently stable to survive the harsh plasma environment in the source as well as the flight time to their detection at the back end of the apparatus. Furthermore, it is remarkable that the sample seemed not to contain any intact empty C_{80} . This supports a conjecture formulated by Ross et al. that pristine C_{80} molecules are unstable but the presence of Lu_3N inside does strongly stabilize the compound [66].

Behind the mass-over-charge analyzing magnet (7), the ion beam passed through further steering (8,13) and focusing elements including an electrostatic quadrupole lens (12). It was then directed onto the photon axis by a cylindrical electrostatic deflector (15). In the interaction region (18), currents of up to 210 pA of singly charged, 20 pA of doubly charged and 18 pA of triply charged $\text{Lu}_3\text{N@C}_{80}$ primary ions could be made available.

Photon-ion interaction

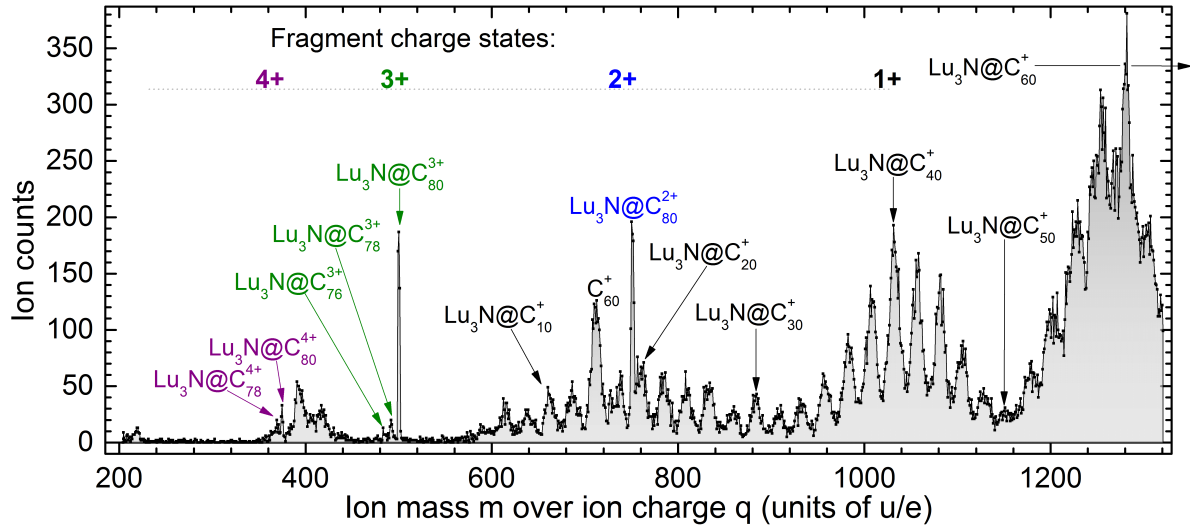


Figure 4.10.: Product-ion mass-spectrum obtained by sweeping the demerging magnet field while the photon energy remained at 300 eV. The mass scan could not be extended to include the primary $\text{Lu}_3\text{N}@C_{80}^{+}$ beam because its intensity would have saturated the single-particle detector.

The interaction between photons and $\text{Lu}_3\text{N}@C_{80}^{p+}$ ions led to ionization and fragmentation of the primary ions. Relative cross sections $\sigma(E)$ for these processes were measured by recording the $\text{Lu}_3\text{N}@C_{80-x}^{q+}$ production rate as a function of photon energy ($p=1,2,3$; $q=2,3,4,5,6$; $x=0,1,3,4$). For the photon-ion interaction studies, the photon flux was measured with a calibrated photodiode (26). It ranged from 10^{12} s^{-1} up to 10^{13} s^{-1} depending on photon energy and the selected resolving power. In order to obtain relative cross sections from the measured ion yields, these were normalized on the simultaneously recorded photon flux and primary ion current.

Product-ion detection

The various reaction products were separated by a second mass-over-charge analyzing dipole magnet (21, demerging magnet) following the photon-ion interaction region (18). Prior to the selection of specific reaction products, an overview over the product beam composition was obtained by simultaneously scanning the demerging-magnet (21) field strength and recording the product count rate employing a single particle detector (24b) [67, 68].

4. Experimental techniques

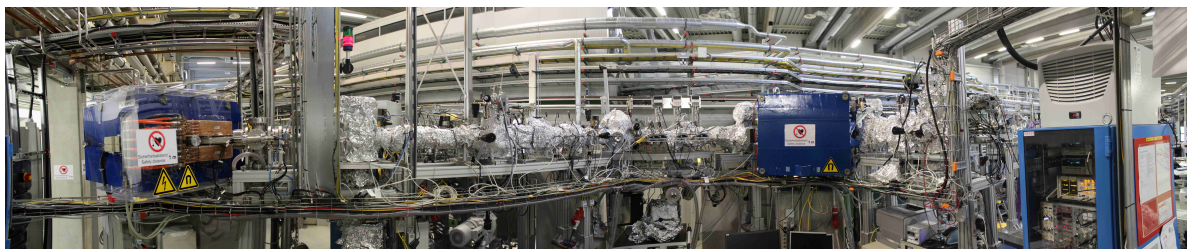


Figure 4.11.: PIPE from the analyzer magnet to the detector chamber (see Fig. 4.7).

Figure 4.10 shows the product-ion spectrum resulting from interactions of a $\text{Lu}_3\text{N}@C_{80}^+$ ion beam with 300-eV photons and with the residual gas. Various fragment ions and different charge states of $\text{Lu}_3\text{N}@C_{80}$ can be identified. Two classes of peaks with different widths can be distinguished: There are few narrow peaks whereas the vast majority of peaks are broader. The narrow peaks originate from photo reactions resulting in $\text{Lu}_3\text{N}@C_{80}^{2+,3+,4+}$ and fragments. This was verified by blocking the photon beam upstream of the interaction region (25): The narrow peaks vanished. A consistent mass calibration was obtained from the three photoion species present. The broad peaks originate from collisions of the primary ions with residual gas particles along their flight path. There are three contributions to the widths of the wider peaks: First, collisions with residual gas can also happen off the photon axis, thus allowing products originating from a larger spatial region to contribute to the detector signal. Second, inelastic collisions (and elastic collisions as well) involve an exchange of momentum resulting in a momentum spread. Third, fragmentation of molecules is accompanied by an internal energy transfer resulting in a kinetic energy release (KER). The distribution of broad peaks follows a periodic pattern where one peak corresponds to a fragment with one carbon dimer more (or less, respectively) than the neighboring peak. One can unambiguously assign mass-over-charge ratios to these peaks which correspond to fragments of $\text{Lu}_3\text{N}@C_{80}$ primary particles.

4.2.5. Sample evaporation performance plots

In a novel yet simple approach, the endohedral ion current was monitored together with the heating power of the evaporation oven and the time elapsed since starting the oven heating several times an hour during the complete sample lifetime. One way to present these data in a two dimensional graph is to plot the current vs. the elapsed time. This type of “performance plot” has proven to be quite useful: After monitoring a couple of samples this way, it appeared that the area of the current integrated over the time almost stayed the same within a group of samples produced together. In this case monitoring the sample performance could possibly allow one to estimate a

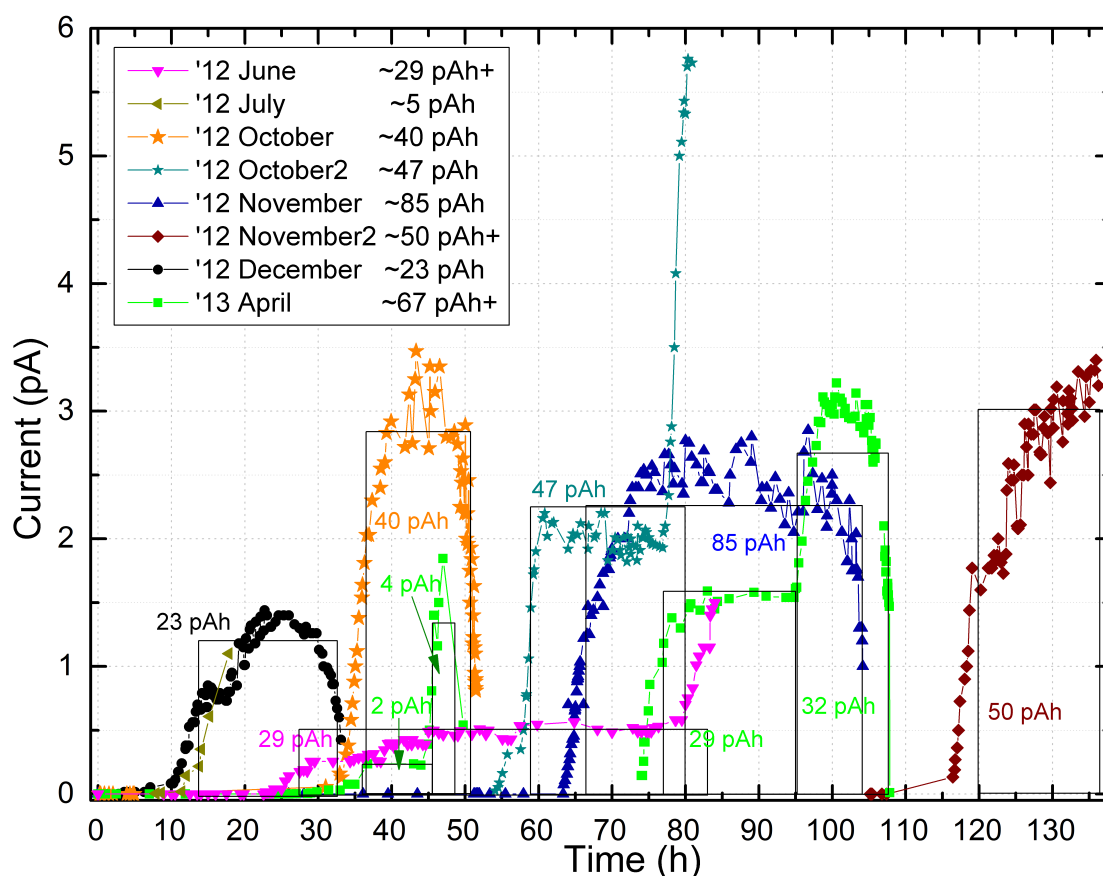


Figure 4.12.: Ion current performance plots of Xe@C₆₀ samples used for ion beam generation at the IPB endstation.

remaining sample lifetime depending on the emitted current, thus also allowing to schedule beamtime operations more accurately.

Furthermore, it appeared that some samples did not follow the pattern but yielded less total integrated current \times time if the pace of the increases of oven heating power was distinctly higher. Unfortunately, these insights cannot be proven because for obvious reasons one cannot use / evaporate a sample twice. Figure 4.12 shows several sample performance plots from the IPB endstation.

The increase in endohedral ion current due to improved sample yields and performance monitoring also led to another synergistic factor for an increased endohedral ion current: Since the increased endohedral currents under improved conditions were intense enough, beam transport of endohedral ions could directly be optimized. Previously, beam transport had to be optimized for C₆₀ ions and the settings then had to be scaled to Xe@C₆₀ settings.

5. Triple photoionization and photofragmentation of Xe@C₆₀

Particularities of the endohedral fullerene substance Xe@C₆₀ have been introduced in chapter 3 and detailed in previous publications [1, 38, 53] and references therein. In short: Xe@C₆₀ is an interesting substance to investigate endohedral fullerenes because the noble gas xenon does not form strong bonds with the carbon cage, thus, allowing 'independent' behavior of cage and encapsulated atom as well as preventing exohedral bonding to the investigated species. Besides, the encapsulated xenon is very likely centered inside the cage due to its size. Furthermore, xenon exhibits a well known very strong 4d resonance for absorbing photons at an energy E_γ of about 100 eV. This 'giant' resonance is related to 4d \rightarrow ϵ f transitions and strong electron-electron correlations. Almost the total oscillator strength of the ten 4d electrons of xenon is concentrated in this shape resonance ($f=10$).

Throughout prior studies investigating photoionization reactions of Xe@C₆₀⁺, no signature of the encapsulated xenon atom could be identified in **single**-ionization reaction channels. In **double**-ionization reaction channels of Xe@C₆₀⁺, however, a very clear xenon signature was verified in the energy range 70–140 eV related to the Xe 4d resonance. Accordingly, a central question of the present investigations on **triple**-ionization reactions of Xe@C₆₀⁺ was to clarify if a xenon-4d signature is present. Since for double ionization of Xe@C₆₀⁺ ions the excess cross section due to the encapsulated xenon atom was found to be redistributed and exhibiting confinement oscillations, the present investigations also searched for such confinement oscillations in triple ionization channels of Xe@C₆₀⁺ primary ions. Additionally, it was in question how the oscillator strength is redistributed due to confinement oscillations as compared to the situation of double ionization.

In contrast to the free xenon atom there is an increased number of product channels for a xenon atom encapsulated inside a carbon cage: The photoreactions of an endohedral fullerene can also involve it losing carbon dimers C₂. In the case of double ionization of Xe@C₆₀⁺, the xenon-4d oscillator strength was found to be diverted to several product channels Xe@C_{60-2n}³⁺ ($n=0,1,2,3$) and, surprisingly, with the biggest intensity in the Xe@C₅₆³⁺ product channel.

For atomic xenon it is known that the triple-ionization cross section also exhibits the same 4d resonance with the same shape covering the same energy range of that of double-ionization while the absolute cross section of triple ionization accounts to about 37% of the double-ionization cross section. This leads to the question if the oscillator strength of the encapsulated xenon atom is distributed among double and triple ionization of encapsulated xenon in the same proportions as it is distributed among double and triple ionization of free atomic xenon.

All measurements presented in this chapter were carried out at the IPB endstation (see chapter 4.2.2) of beamline 10.0.1 at the ALS in Berkeley. The majority of photoionization and photofragmentation measurements of Xe@C₆₀ ions presented in this chapter have been obtained using samples of endohedral fullerene material produced by Dr. A. L. David Kilcoyne at the ALS at Lawrence Berkeley National Laboratory. A minor part of the measurements were made using samples produced in Gießen (see section 4.1). Previously published results on double ionization of Xe@C₆₀⁺ including fragmentation channels as well as theoretical predictions cited therein are presented as a reference for comparison with the current results.

Four different 'classes' of photoreactions of Xe@C₆₀ ions have been investigated during numerous beamtimes over the years at the IPB endstation:

1. Single ionization without and with fragmentation of singly charged positive ions
 $\text{Xe@C}_{60}^{+} \rightarrow \text{Xe@C}_{60-2n}^{2+}$ (n=0,1)
2. Double ionization without and with fragmentation of singly charged positive ions
 $\text{Xe@C}_{60}^{+} \rightarrow \text{Xe@C}_{60-2n}^{3+}$ (n=0,1,2,3,4)
3. Triple ionization with fragmentation of singly charged positive ions
 $\text{Xe@C}_{60}^{+} \rightarrow \text{Xe@C}_{60-2n}^{4+}$ (n=1,2)
4. Double ionization without and with fragmentation of singly charged **negative** ions
 $\text{Xe@C}_{60}^{-} \rightarrow \text{Xe@C}_{60-2n}^{+}$ (n=0,2)

As stated above, there was hardly any signature of the encapsulated xenon in the photoreactions of type 1. Those data are unpublished. Data of type 2 have been published by Kilcoyne et al. [38] and with much better statistical quality by Phaneuf et al. [1]. For the purpose of comparison those data will be introduced briefly. The current work presents new results for photoreactions of type 3 (in the present chapter) and type 4 (see chapter 6).

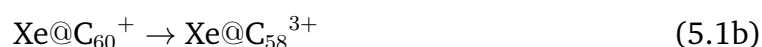
5.0.1. Endohedral excess cross section and absolute calibration

The measured photoionization cross sections are the sum of the individual cross-section contributions from the different individual elements and ions present in the interaction. That is, the measured cross section is constituted by the contribution from xenon and sixty carbon atoms in this case. The term 'endohedral-excess cross section' refers to the contribution in the cross section that caused by the presence of an encapsulated atom or molecule, thus 'exceeding' the cross section of an empty fullerene. In case no separate absolute cross-section measurements for photoreactions of endohedral fullerenes are available, a direct intensity calibration of the cross sections is not possible. However, indirect adjustment to absolute data points of pristine fullerenes can be achieved in a two-step procedure: The relative cross sections for endohedral fullerenes are scaled to match absolute cross-section data of pristine fullerenes in energy ranges where there is no endohedral excess and, thus, identical (for encapsulated xenon, e.g., below 70 eV and above 140 eV) in the respective channels. The excess cross section due to the encapsulated atom is determined by subtracting the endohedral fullerene cross section from the respective pristine fullerene cross section. The particular advantage of extracting the endohedral excess cross sections in this differential way is the instant removal of potential systematic errors possibly present in the individual channels due to their occurring in both subtrahend and minuend. The artifact discussed in the next section is an example for such a systematic error.

The photon-energy uncertainty for double and triple ionization measurements of endohedral fullerenes Xe@C₆₀ carried out at the endstation 10.0.1.1 of the ALS was $\Delta E_\gamma = 0.2$ eV in the photon-energy range 60–150 eV (as reported by Kilcoyne et al. [38]). Due to the ion velocities in the interaction region, the photons are Doppler shifted in the range of 0.007–0.022 eV when hitting the fullerene ions. This energy shift is small in comparison with the above mentioned uncertainty but it was nevertheless corrected for.

5.0.2. Previous measurements of double ionization of Xe@C_{60}^+

In this section, experimental results for double-ionization photoreactions of Xe@C_{60}^+ published Phaneuf et al. [1] are introduced in a compact way for the purpose of comparison with the more recent results for other reaction channels that are presented in the following sections. The conducted measurements cover the following reaction channels:



From the difference of the cross sections of endohedral and empty fullerenes, the endohedral excess cross section was inferred. This endohedral excess cross section is assumed to be purely caused by the oscillator strength of the encapsulated xenon atom and, thus, can be compared to the cross section of the free xenon atom reported by West et al. [69] as well as a variety of theoretical predictions dealing with the redistribution of oscillator strength of the xenon atom due to its encapsulation. In this context, Phaneuf et al. compared calculations published by Puska et al. [16], Amusia et al. [70], Dolmatov et al. [71], Madjet et al. [27], Chen et al. [72], Gorczyca et al. [29], and Li et al. [30] with their experimental results. Furthermore, Phaneuf et al. briefly introduced the theoretical models and highlighted their differences with an emphasis on the interplay of the fullerene geometry (e.g., shell thickness and inner radius) and the photoelectron wavelength. More details on the theoretical models can be found in the references provided above. Figure 5.1 shows an overview of the results compared with model calculations as published by Phaneuf et al. [1]. They found the sum of the four reaction channels in Eqs. 5.1a – 5.1d to account for an oscillator strength $f = 6.2 \pm 1.4$.

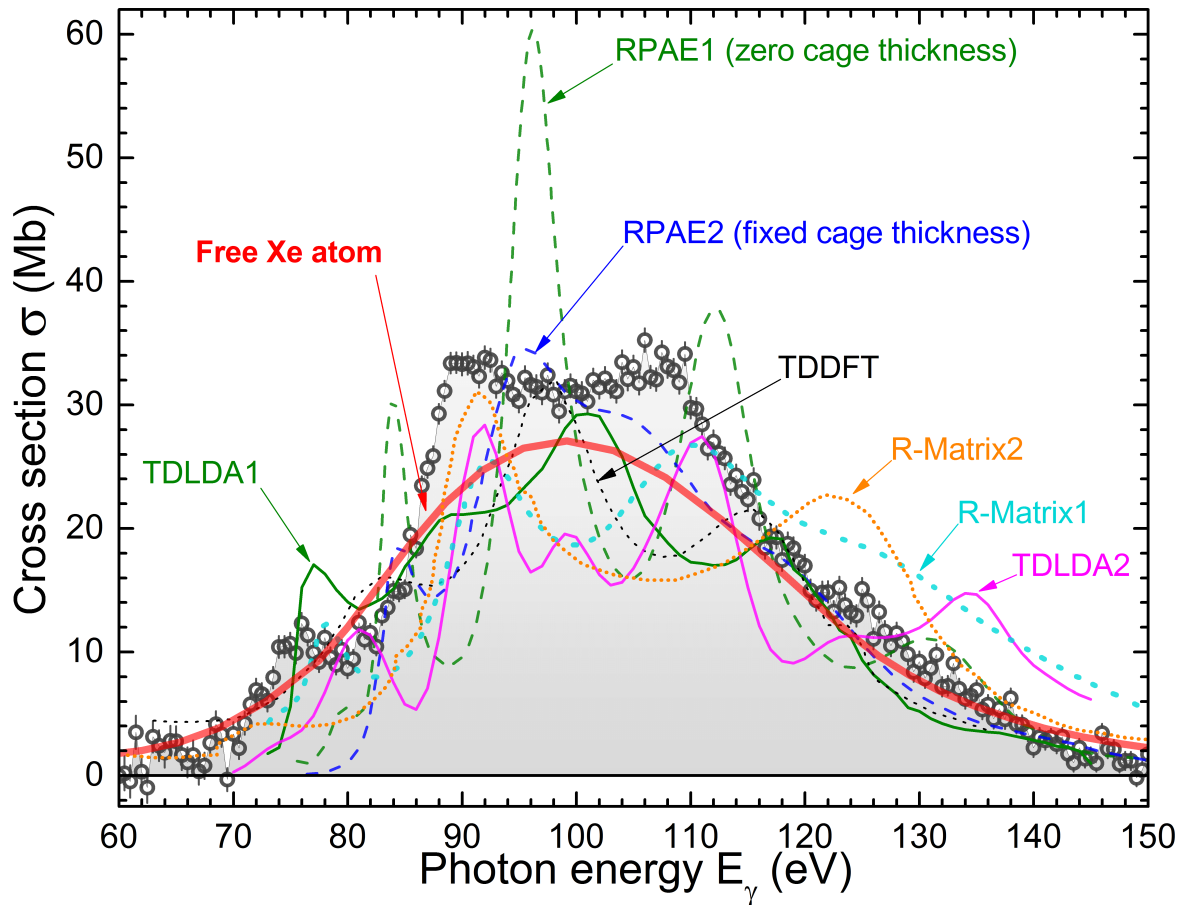


Figure 5.1.: Experimental data and theoretical calculations of the cross sections for photoionization of endohedral Xe@C₆₀ published by Phaneuf et al. [1]. The experimental endohedral-excess cross section (hollow black circles with error bars) represents the sum of the four reaction channels in Eqs. 5.1a – 5.1d and is scaled to match the total xenon 4d oscillator strength $f=10$ for the purpose of comparison in this figure. The various calculation models predict redistribution of Xe 4d oscillator strength due to confinement resonances using different approximations and are shown as solid and dashed lines: Time-dependent density functional theory (TDDFT) (dotted black curve) [16], random phase approximation with exchange (RPAE1) (dashed green curve) [70], RPAE2 (dashed blue curve) [71], time-dependent local density approximation (TDLDA1) (solid green curve) [27], TDLDA2 (solid magenta curve) [72], R-Matrix1 (dotted cyan curve) [29], and R-Matrix2 (dotted orange curve) [30]. The experimental sum cross section has to give an integral oscillator strength of 10 in the investigated energy region. For comparison, the photoionization cross section for the free Xe atom is shown as a thick solid red curve, as recommended by West and Morton [69].

5.1. Triple ionization of Xe@C_{60}^+

To start this section, similarities of and differences between the measured double and triple ionization processes are discussed. The idea is to illuminate the questions that motivated the investigation of triple ionization before the experimental results are shown.

Due to its slightly higher first ionization energy as compared to carbon, it can be assumed that xenon is present as a neutral atom encapsulated inside the Xe@C_{60}^+ parent ions. The photoionization reaction $\text{Xe@C}_{60}^+ \rightarrow \text{Xe@C}_{60}^{3+}$ (or $\text{Xe@C}_{60}^+ \rightarrow \text{Xe@C}_{60}^{4+}$, respectively) in the energy range of the xenon 4d resonance can be traced back to the double ionization of the encapsulated xenon atom $\text{Xe} \rightarrow \text{Xe}^{2+}$ (or to triple ionization $\text{Xe} \rightarrow \text{Xe}^{3+}$, respectively).

Since the probability for direct double ionization (and even more for direct triple ionization) is very small compared to the probability for single ionization, the present discussion will only deal with the net-double (or net-triple) ionization of xenon which is the result of two consecutive processes: First an electron is removed from the 4d subshell of the neutral xenon atom by direct photoionization. An Auger process is the second step. The 4d vacancy is filled with an outer-shell electron and the thereby gained energy leads to the simultaneous emission of another outer-shell electron from the xenon ion. In the case of triple ionization, two outer-shell electrons are detached either in two consecutive Auger processes or in a double-Auger process (see the investigations of Penent et al. [73]).

If these processes happen inside a charged fullerene, the oscillator strength of the 4d shape resonance ought to be preserved but possibly redistributed due to the confinement inside the carbon cage. Following this line of argument, the oscillator strength in double ionization vs. triple ionization channels of Xe@C_{60}^+ should match the known branching ratios of $\text{Xe} \rightarrow \text{Xe}^{2+}$ vs. $\text{Xe} \rightarrow \text{Xe}^{3+}$ as reported by Becker et al. [74].

So the **first question** is not related to the shape of the endohedral excess but to the distribution of its oscillator strength among different product channels: Does the branching ratio for double and triple ionization of Xe@C_{60}^+ match the branching ratio reported for double and triple ionization of neutral xenon?

The **second question** is related to the shape of the resonance structures present in the cross section spectra. Would one expect a different shape in triple ionization spectra as compared to double ionization? In the case of double ionization, the Auger electron carries a discrete energy. In the case of triple ionization, however, two Auger electrons are emitted. As stated above, there are two possibilities for the release of two electrons. If a double Auger process is responsible for the release of the electrons, the energy is distributed continuously among the two electrons (as demonstrated, e.g., for argon by Viefhaus et al. [75]). Otherwise, if two consecutive Auger processes occur, the

kinetic energy of each electron would be smaller than in the net-double ionization case. (See Penent et al [73] for the cascade of two consecutive Auger decays of xenon.) Now the question is if the shape of the triple photoionization cross-section spectra deviates from that of double ionization. Furthermore, could that possible deviation be explained considering the different energies of the Auger electrons involved? In other words: Would the sharp resonances visible in the double-ionization spectra be softened and washed out in triple ionization? Such a finding would support the conjecture that the confinement resonances are not only a result of the initial photoionization but also influenced by the successive Auger process - which involves an continuous Auger-electron energy distribution in the case of triple ionization.

5.2. Results for Xe@C₅₈⁺⁴ products

An earlier, preliminary study has briefly dealt with triple ionization of Xe@C₆₀⁺ in the fragmentation product channel



These data are shown below in Fig. 5.2 as published by N. Aryal [76]. For comparison with the present results, however, the data have been reanalyzed independently. Apart from Fig. 5.2, only the results of the new analysis will be used. In general, the previous results could be reproduced during the new analysis. Minor differences will be discussed in section 5.3.2.

The Xe@C₆₀⁺ → Xe@C₅₆⁴⁺ data have been recorded in an individual measurement sweeping the photon energy region 20 times with 0.5 eV increments. The IPB endstation was operated with the monochromator entry slit fixed to 56 μm and the exit slit fixed to with of 774 μm. The IPB endstation was operated in spectroscopy mode (no bias voltage applied to the interaction region, see section 4.2.1 for details on this mode). Parent-ion currents ranged from 1.9 to 2.9 pA. The accumulated integration time is 200 seconds at each photon energy. For this measurement, there was no on-line background determination but the background count rate has been investigated thoroughly immediately before starting the measurement: With a photon energy of 90 eV and a parent-ion current of 2.3 pA, a count rate of 0.35 Hz/pA was recorded for signal+background and 0.07 Hz/pA were counted with the photon beam flagged (counting 200 s each). Thus, a signal:background ratio of 4:1 was determined.

The endohedral spectrum was put to an absolute scale indirectly aided by absolute cross section measurements at three energies (90, 105, and 140 eV) and a triple ionization spectrum of the corresponding empty-cage photoreaction C₆₀⁺ → C₅₆⁴⁺. Apparently

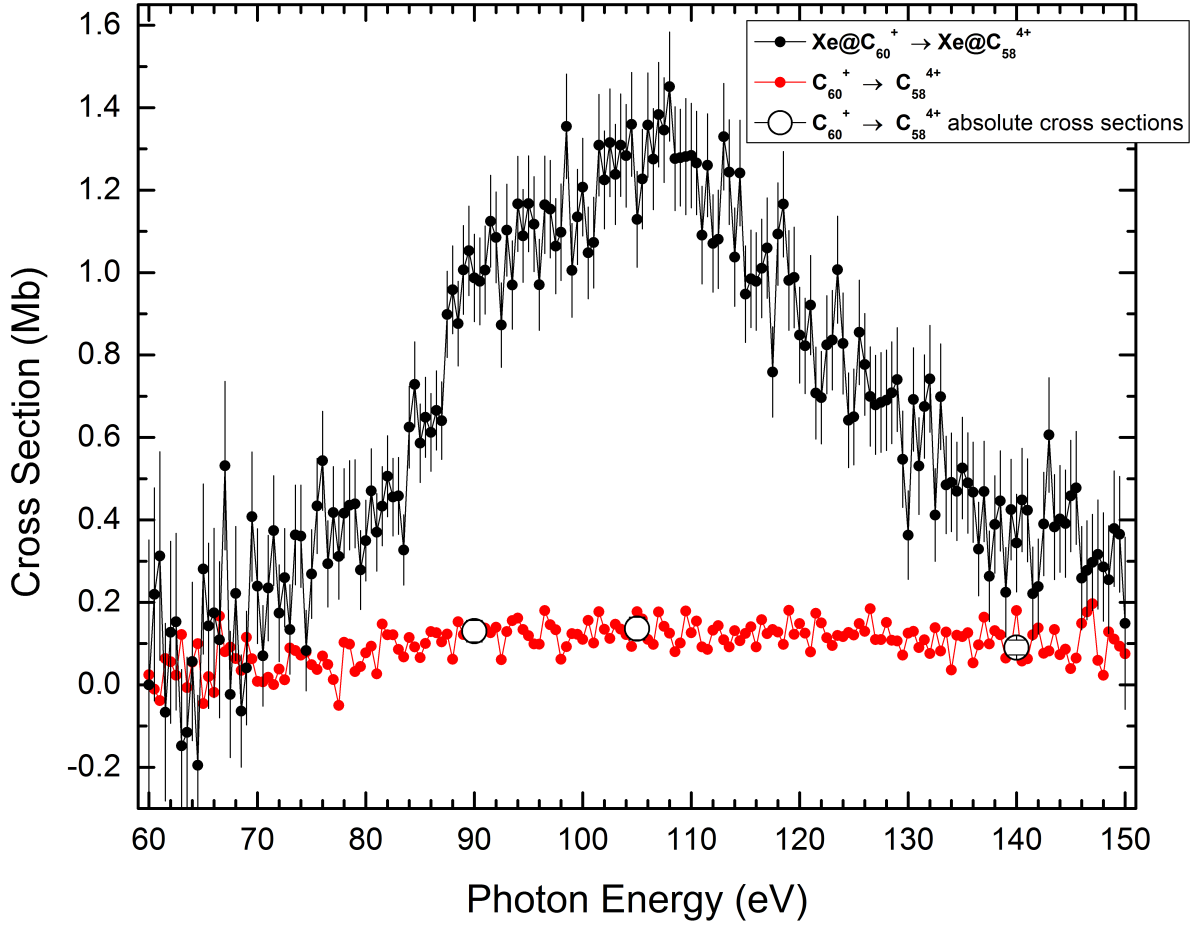


Figure 5.2.: Relative cross section of the photoreaction $\text{Xe}@C_{60}^{+} \rightarrow \text{Xe}@C_{58}^{4+}$ published by N. Aryal [76]. In this publication, the endohedral data were put to an absolute scale by matching the empty cage cross section around 70 and 140 eV. The corresponding empty cage was scaled to match three absolute points at 90, 105, and 140 eV.

the endohedral excess cross section dominates this photoreaction channel: Unlike observed in double ionization reaction channels, the cross section due to the empty cage contributes less than 14% in the energy range 70–150 eV. An oscillator strength $f = 0.47$ was attributed to the xenon-4d excess cross section in this reaction channel in the previous study (a total $f = 0.545$ minus $f = 0.078$ due to the cage). The new analysis found $f = 0.46 \pm 0.12$.

5.3. Results for Xe@C₅₆⁺⁴ products

During the present project, results were obtained for triple-ionization with fragmentation of Xe@C₆₀⁺ in the additional photoreaction channel



This is the first photoreaction channel of endohedral fullerenes for which an absolute cross section was measured. Accordingly, the relative spectrum could be put to an absolute scale directly. In all other cases and previously reported channels, normalization had been provided indirectly (as detailed above in the beginning of section 5.0.1). Figure 5.3 shows the summed scan data of seven files with on-line background

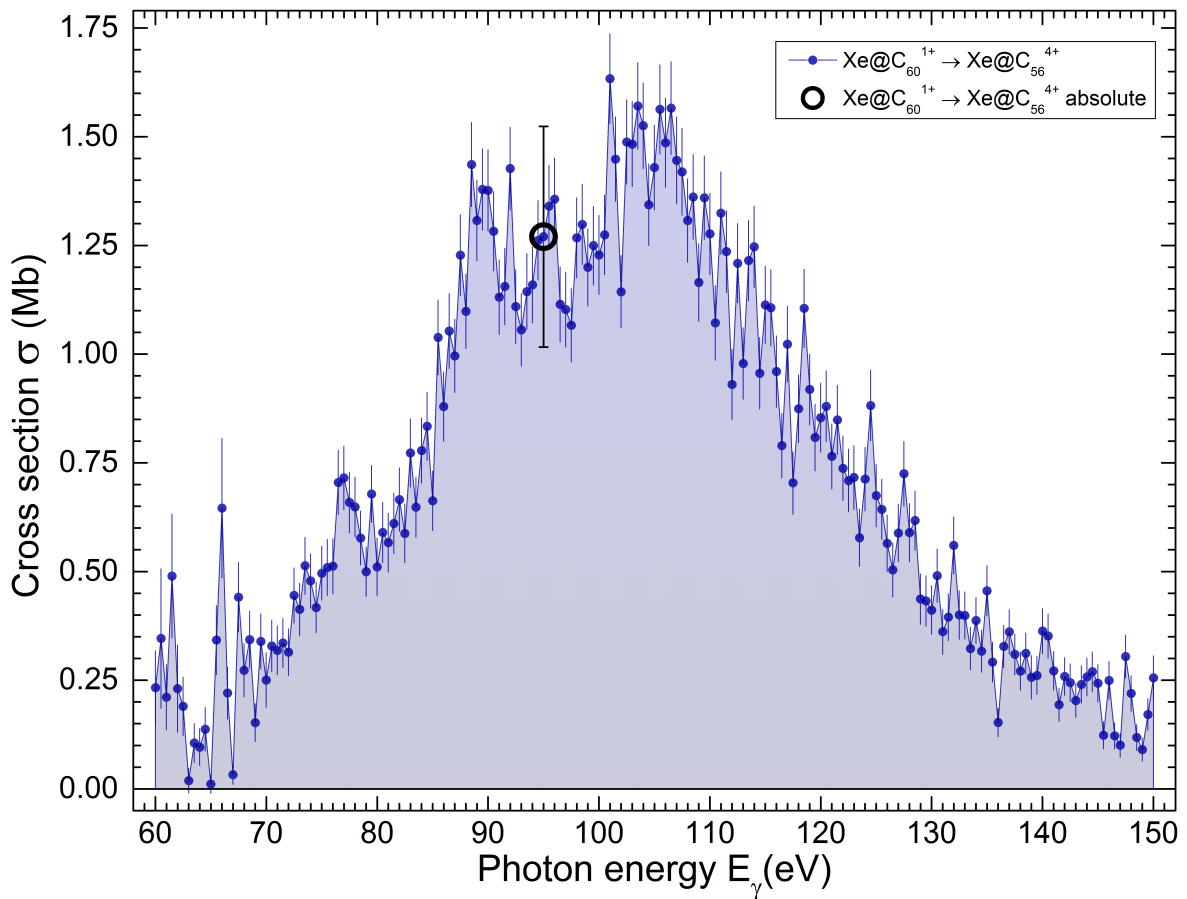


Figure 5.3.: Cross section for Xe@C₆₀⁺ → Xe@C₅₆⁴⁺ (solid blue circles with statistical error bars) are put to an absolute scale by normalization to an absolute measurement at 95 eV (open circle with total error bar). Besides two broad peak features at 90 and 105 eV, a smaller peak is evident at about 77 eV.

determination (mechanical chopping of the photon beam) and three files with manual background determination with a total measurement integration time per point of 375 s. The photon energy was scanned from 60 to 150 eV in 0.5 eV steps. For all seven measurement runs, the IPB endstation was operated with identical monochromator-slit settings for maximum photon flux. The entry slit was set to 58 μm and the exit slit was set to 1300 μm width. Averaged parent-ion currents were in the range of 2–8 pA. At 90 eV photon energy, a signal:background ratio of 2:1 was determined counting for 500 seconds each. The average parent-ion current was 1.4 pA during the determination of count rates. (153 counts were registered for signal+background opposed to 53 counts registered with the photon beam flagged. Accordingly, the signal rate was 0.142 Hz/pA and the background rate was 0.076 Hz/pA.) The scan measurements are put on an absolute scale by an absolute cross-section measurement at a photon energy E_γ 95 eV. The present experimental result for the channel Xe@C₆₀⁺ \rightarrow Xe@C₅₆⁴⁺ is compared with the extracted excess cross section of the encapsulated atom (Cross section of the endohedral fullerene minus cross section of the empty cage) in the corresponding reaction channel for double ionization with fragmentation which has been published previously [1].

Assuming the observed cross section contains no contributions from the carbon cage, one would obtain a xenon oscillator strength $f = 0.54 \pm 0.14$ in the investigated channel. Assuming the carbon cage to contribute about 14% like in the previously studied triple-ionization channel, one finds $f = 0.46 \pm 0.12$. Phaneuf et al. [1] found that the cross sections of reactions resulting Xe@C₅₆ fragments account for about 50% of the non-fragmentation cross section in double ionization and about 21% of the non-fragmentation cross section in single ionization. In the absence of triple-ionization fragmentation studies of the fullerene C₆₀, it is assumed the cage contributes about 7% (mean value of the range of 0–14%) to the cross section observed for Xe@C₆₀⁺ \rightarrow Xe@C₅₆⁴⁺ photoreactions in the energy range 70–150 eV. This assumption is accounted for in an increased uncertainty. As a result, an oscillator strength $f = 0.50 \pm 0.18$ is derived for the Xe@C₅₆⁴⁺ product channel.

This is less than what was found in the corresponding double-ionization channel yet with about 5% of the total xenon-4d oscillator strength $f = 10$, it is a significant fraction. The observation of ionization signals of the encapsulated xenon atom in a triple-ionization channel encourages further investigations in other triple-ionization reaction channels and possibly extending the scope to reaction channels with more highly charged final states.

From the observation that the photoreaction cross section for the triple-ionization channel looks like the endohedral-excess cross section extracted in the corresponding double-ionization channel (with fragmentation) of the same parent ion, one can conclude that the cage cross section does not play a dominant role in triple ionization.

5.3.1. Comparison with double ionization product channels

Remarkably, the two datasets shown in Fig. 5.4 look very similar: The overall shape is matched closely and peak-like structures at 77, 90, and 105 eV are distinguishable both in the double and triple-ionization spectrum. Furthermore, the rising slope in the energy range 70–90 eV and the falling slope in the energy range 110–150 eV are almost identical. A difference can be identified in the intensities of the two strongest peak features: While in the double-ionization spectrum the peak feature at 90 eV is about 10% stronger than the 105 eV peak feature, it is the other way round in the triple-ionization spectrum.

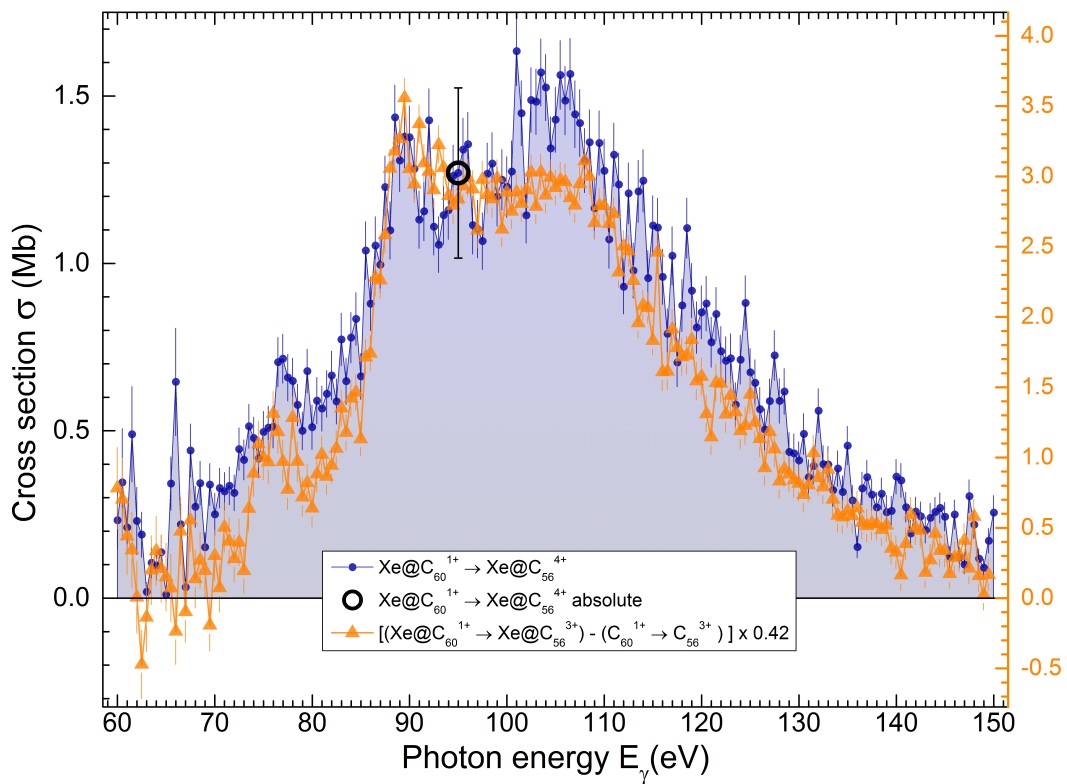


Figure 5.4.: Cross section for $\text{Xe@C}_{60}^{1+} \rightarrow \text{Xe@C}_{56}^{4+}$ triple ionization (solid blue circles with statistical error bars) put to an absolute scale by normalization to an absolute measurement at 95 eV (open circle with total error bar). The current measurement is compared to previously published data from the corresponding double-ionization reaction $\text{Xe@C}_{60}^{1+} \rightarrow \text{Xe@C}_{56}^{3+}$ (Phaneuf et al. [1]; solid orange triangles with statistical error bars). The double ionization data were scaled to 50% for easier comparison. Note that the present data represent the cross section of the whole endohedral system whereas for the previously published double-ionization data only the endohedral-excess cross section due to the presence of the encapsulated xenon atom is shown.

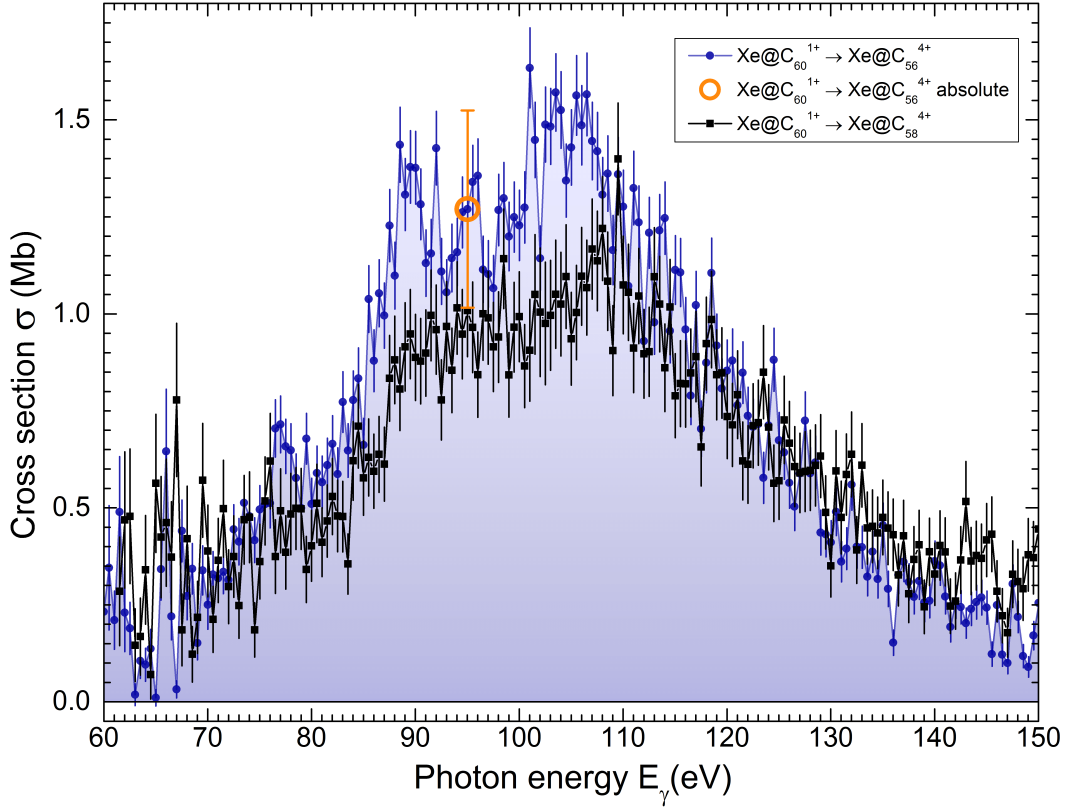
5.3.2. Comparing the Xe@C_{56}^{+} and Xe@C_{58}^{+} product channels

Figure 5.5.: Comparing the cross-section spectra of two triple-ionization photoreaction channels starting from the identical parent ion Xe@C_{60}^{+} . Cross section for $\text{Xe@C}_{60}^{+} \rightarrow \text{Xe@C}_{56}^{4+}$ triple ionization (solid blue circles with statistical error bars) put to an absolute scale by normalization to an absolute measurement at 95 eV (big hollow orange circle with total error bar). The current measurement is compared to newly analyzed data for $\text{Xe@C}_{60}^{+} \rightarrow \text{Xe@C}_{58}^{4+}$ reactions (solid black squares with statistical error bars) indirectly put to an absolute scale guided by a spectrum and absolute measurements shown in Fig. 5.2. A different previous analysis of these data has been published by N. Aryal [76].

Cross-section spectra for triple-ionization photoreactions with Xe@C_{56}^{4+} and Xe@C_{58}^{4+} product ions are compared in Fig. 5.5. The general impression is that two datasets look similar but resonance-like features (at about 77, 90, and 105 eV) are less pronounced in the Xe@C_{58}^{4+} data. In particular, the structure at 90 eV is not only strikingly present in the new Xe@C_{56}^{4+} product channel but it was found in the four double-ionization photoreaction channels ($\text{Xe@C}_{54,56,58,60}^{3+}$ products). The Xe@C_{58}^{4+} data have a bigger statistical uncertainty specifically at photon energies below 75 eV and above 130 eV.

5. Triple photoionization and photofragmentation of Xe@C₆₀

At lower photon energies, however, both spectra exhibit too little statistic accuracy for quantitative deductions while in the photon energy range 75–130 eV the statistical uncertainty is significantly smaller thus allowing for a comparison.

Since the discrepancies between the triple ionization spectra are slightly exceeding the variations found between double-ionization channels, several possibilities that could explain these minor discrepancies are discussed in the following.

1. The discrepancies may at first appear to big to be explained referring to the statistical uncertainty but the scatter of the data might misguide the eye. It is very well possible that the underlying endohedral-excess contributions in the two channels share the same shape.
2. From the experience with various photoreactions of both pristine and endohedral fullerenes, it appears to be very unlikely but it cannot be excluded that there is a difference in the structure of signal background in the two triple-ionization measurements: The measurement with Xe@C₅₈⁴⁺ products was conducted in spectroscopy mode (no bias voltage was applied to the interaction region) whereas the measurement with Xe@C₅₆⁴⁺ was carried out in the hybrid spectroscopy mode (a bias voltage was applied to the interaction region; for details on measurement modes see section 4.2.1). The bias voltage could have suppressed a specific background component.
3. So far, the triple-ionization investigations suggest that the fullerene-cage cross section is free from structures and only of the order of 10% of the endohedral-excess cross section. Investigations of the C₅₆⁴⁺ product channel have not reached the statistical accuracy to exclude smaller differences to the C₅₈⁴⁺ channel which are, however, not expected.
4. Finally, the difference in the observed endohedral-excess cross section might possibly be caused by difference between the processes resulting in Xe@C₅₈⁴⁺ products and all the other double-ionization and triple-ionization photoreaction channels investigated so far. This would be a surprising finding but at this point there is not enough evidence supporting such a novel effect.

The different photon-energy bandwidths employed for measuring the two reaction channels cannot provide an explanation for the discrepancies between these two spectra: The monochromator exit slit was opened to 1300 μm for Xe@C₅₆⁴⁺ product ion measurements and to 774 μm for Xe@C₅₈⁴⁺ product ion measurements which results in a reduced photon-energy bandwidth. Since the spectral features are broad in relation to the photon energy bandwidths, the features would only appear narrower and more pronounced in the Xe@C₅₈⁴⁺ channel but the opposite appears to be evident.

In conclusion, while the investigations on triple ionization in Xe@C₅₆⁴⁺ and Xe@C₅₈⁴⁺ product channels agree in general, minor discrepancies between the measurements of

these channels cannot be resolved unambiguously at this point but appear to be within the measurement uncertainty. The experimental results allow to derive Xe-4d oscillator strengths. The outcome that the same endohedral-excess cross-section shape was found in all studied photoreaction channels motivates studying further triple-ionization photoreaction channels.

5.4. Closing discussion on the triple ionization

The endohedral cross-section spectra for double and triple photoionization of $\text{Xe}@C_{60}^{n+}$ in the photon energy range 60 to 150 eV share a practically identical shape within the limits of experimental uncertainty. A Xe-4d oscillator-strength branching ratio of $(3.7 \pm 1.7):1$ between the double and triple ionization photoreactions is determined for endohedral fullerene fragments with 58 carbon atoms $\text{Xe}@C_{58}^{n+}$ neglecting the slightly different endohedral excess cross sections. For $\text{Xe}@C_{56}^{n+}$ fragments, a branching ratio of $(5.2 \pm 2.8):1$ is determined. Within the uncertainty limits, this matches the double / triple-ionization branching ratio of 2.5 ± 0.2 reported for atomic xenon by Becker et al. [74]. It might be argued, however, that not the branching ratio between individual fragmentation channels but rather the sum oscillator strength of all triple ionization reactions should be compared to the sum of double ionization channels.

Product ion	D.I. strength	T.I. strength	Ratio
Xe^{n+}	* 18.7 ± 0.7	* 7.0 ± 0.3	2.5:1 – 2.9:1
$\text{Xe}@C_{60}^{n+}$	1.71 ± 0.38		
$\text{Xe}@C_{58}^{n+}$	1.51 ± 0.33	0.46 ± 0.12	2.0:1 – 5.4:1
$\text{Xe}@C_{56}^{n+}$	2.10 ± 0.46	0.50 ± 0.18	2.4:1 – 8.0:1
$\text{Xe}@C_{54}^{n+}$	0.85 ± 0.19		

Table 5.1.: Branching ratios (double ionization D.I. : triple ionization T.I.) extracted from net Xe-4d oscillator strengths or cross sections observed for double and triple ionization photoreaction channels. The experimental results for atomic xenon are on an arbitrary scale. These values have been extracted from cross sections published by Becker et al. [74]. *: The cross sections have been extracted graphically from figures. Accordingly, the values and their errors are on an arbitrary scale and also reflect the inaccuracy resulting from the graphical extraction. The values for double-ionization oscillator strength of the different endohedral fullerenes $\text{Xe}@C_{54-60}^{n+}$ were reported by Phaneuf et al. [1].

5. Triple photoionization and photofragmentation of Xe@C₆₀

Observing practically the same shape for the endohedral-excess cross section in the spectra of double- and triple-ionization photoreactions of Xe@C₆₀⁺ parent ions, one can conclude that the shape and resonance distribution of the excess cross section is determined by the same primary process. This primary process involves the interference of the incident photon, the xenon-4d electron that is detached, and the (charged) fullerene cage. Assuming that the double- and triple-photoionization products are final states of reactions that both start with the single photoionization of the xenon-4d subshell, it is valid to sum up the oscillator strength in the excess cross section due to the xenon-4d 'giant' resonance found in all these channels. The result of adding the oscillator strength of the four double-ionization and two triple-ionization channels measured thus far (listed in Tab. 5.1) is a sum of (7.13 ± 1.66) of the total Xe-4d oscillator strength of 10.

The final charge states of the product ions, in contrast, are the results of different secondary processes. The most intuitive candidates for these secondary processes are Auger ionization processes. However, the successive Auger processes appear not to play a major role regarding the confinement resonances found in the endohedral excess cross section. (Differences between these processes can most probably be found, e.g., in the energy and angle distribution of the Auger electrons for which the present experiment is not sensitive.)

Apparently these two consecutive processes are disentangled: The energy of the incident photon is completely consumed by the xenon 4d ionization in the first step. The photon energy exceeding the binding energy of the electron is carried away by the photoelectron as kinetic energy. Consequently, the initial conditions of the different Auger processes that follow and result in net-double or net-triple ionization are identical and particularly independent of the incident photon energy. Hence, the meaning of the double- and triple-photoionization cross-section spectra of Xe@C₆₀⁺ presented in this study lies in the demonstration of the incident-photon-energy dependence for creating a 4d vacancy in a xenon atom that is embedded in the specific environment inside a charged C₆₀ fullerene cage.

6. Double photoionization and fragmentation of fullerene anions Xe@C_{60}^-

The investigations on negatively charged ions Xe@C_{60}^- , as stated above, have started with the more fundamental questions if a sufficiently intense beam of ions can be generated and if this negatively charged endohedral fullerene is stable enough to be used for measurements. Once this prerequisite was fulfilled, the central idea was to look for an endohedral-excess cross-section contribution in the double ionization of negatively charged Xe@C_{60}^- . A further question dealt with the potential effects of the change of the sign the expected xenon-4d feature in this situation otherwise symmetric to that of the established double ionization of Xe@C_{60}^+ . Would this new reaction channel show signs of confinement oscillations? How would these compare to the double ionization of the positively charged counterpart Xe@C_{60}^+ in terms of shape and in terms of absolute intensity?

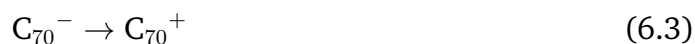
In the present study, double-ionization and double-ionization with fragmentation of negative endohedral fullerene ions have been investigated in the following photoreaction channels:



For extracting the excess in the photoreaction cross-section due to the presence of the encapsulated xenon atom, the respective empty-cage photoreactions have been measured:



Additionally, one photoreaction channel of the fullerene C_{70} has been scanned.



Studies investigating other photoreactions of negative fullerene ions have remained preliminary.

The majority of photoionization and photofragmentation measurements of $\text{Xe}@C_{60}$ ions presented in this chapter have been obtained using samples of endohedral fullerene material produced by Dr. A. L. David Kilcoyne at the ALS at Lawrence Berkeley National Laboratory. A minor part of the measurements were made using samples produced in Gießen (see section 4.1). All measurements with negative fullerene ions presented in this chapter were carried out at the IPB endstation (see chapter 4.2.2) of beamline 10.0.1 at the ALS in Berkeley and have been conducted in *fixed-slits* mode (for details on IPB operation modes, see section 4.2.2). It turned out that under the condition of the present fullerene studies, the photon beam did slightly change its spot size and/or position while the photon energy was scanned using the low-energy grating of the monochromator. These small variations did not only depend on the employed photon-resolution mode (fixed slits or constant resolution) but also on the selected photon energy bandwidth. As a consequence, the overlap of beams is exhibiting a weak but unwanted photon-energy dependence for some low-energy-grating data. The indirect influence of this beam-motion behavior is not fully quantified.

For empty-cage fullerene data, the conjunction of a smooth cross section and the availability of absolute cross-section measurements still allows the reconstruction of spectra covering the whole range of the medium and the low-energy grating. For endohedral fullerenes, however, the cross section is not as smooth, the statistical uncertainties are larger, and no absolute cross-section data are available. As a consequence, unambiguous reconstruction of two-grating spanning endohedral spectra was not possible at present. On the other hand, the medium-energy grating covers the entire photon-energy range in which the xenon endohedral excess cross section has been observed in other reaction channels. Consequently, low-energy-grating endohedral-fullerene data are not relevant for investigating confinement resonances and, thus, will not be treated in this study.

Working with negatively charged primary ions at the IPB endstation is more difficult than working with positive primary ions (which is the usual case). The ECR ion source and the associated extraction geometry of the ion beamline are designed for transporting positive ions. As a consequence, the intensity of negative ion currents that can be extracted from the source (in otherwise identical conditions) is reduced by a factor three to five as compared to extracting positive ions. Another consequence of working with negative ions is a reduced mass resolution at the first magnet due to the expanded ion-beam profile. Therefore, proper separation of the desired parent ion beam comes, again, at the cost of ion beam intensity. Under measurement conditions, a stable peak primary $\text{Xe}@C_{60}^-$ current of 3.2 pA could be transported to the interaction region. In summary, when conducting measurements with negative parent ions, the measurement times are considerably higher for reaching the statistical quality of the results reported for positive ions (see section 5.0.2 and reference [1]).

In this section, recent experimental results using the medium-energy grating are shown. Emphasis is put on the excess in the photoreaction cross-section due to the presence of

the encapsulated xenon atom and comparison with double-ionization photoreactions of the corresponding positive parent ions introduced in section 5.0.2. Endohedral-fullerene scan measurements were put on an absolute cross-section scale by first normalizing empty-cage fullerene scan measurements to an absolute scale provided by absolute cross-section measurements and scaling the endohedral measurements to the empty-cage scans afterwards (as detailed at the beginning of chapter 5.0.1).

6.1. Double ionization of Xe@C_{60}^- ions with fragmentation

Of the four double-ionization reaction channels of Xe@C_{60}^+ reported by Phaneuf et al. [1], the reaction channel $\text{Xe@C}_{60}^+ \rightarrow \text{Xe@C}_{56}^{3+}$ that involves the loss of two carbon dimers C_2 exhibits the strongest endohedral cross-section contribution. Consequently, investigating the corresponding reaction channel of negative fullerene primary ions was given the highest priority.

Figure 6.1 shows the experimental cross-section spectrum of $\text{Xe@C}_{60}^- \rightarrow \text{Xe@C}_{56}^+$ photoreactions. This spectrum has strong similarities to that of $\text{Xe@C}_{60}^+ \rightarrow \text{Xe@C}_{56}^{3+}$ data shown in Fig. 6.2.

Starting from negative ions, the endohedral excess cross section is overall only about half as strong as that for reactions starting from positive parent ions. In the photon energy range 85–100 eV, however, it appears that the cross section of the negative ions is also showing relatively less intensity as compared to the range 100–130 eV. In other words, the broad feature centered around 105 eV is more pronounced in relation to the feature at about 88 eV for the negative ions. For the reaction of positive ions, in contrast, the feature centered around 88 eV is more pronounced. Another remarkable difference is the presence of what appears to be a sharp and intense feature at 75 eV. To carve out the accurate shape of this feature and its true intensity, better statistics and possibly a smaller photon energy step size would be required. From the endohedral excess cross section present in the $\text{Xe@C}_{60}^- \rightarrow \text{Xe@C}_{56}^+$ photoreaction channel, an oscillator strength of $f = 0.66 \pm 0.17$ is inferred.

6. Double photoionization and fragmentation of fullerene anions Xe@C_{60}^-

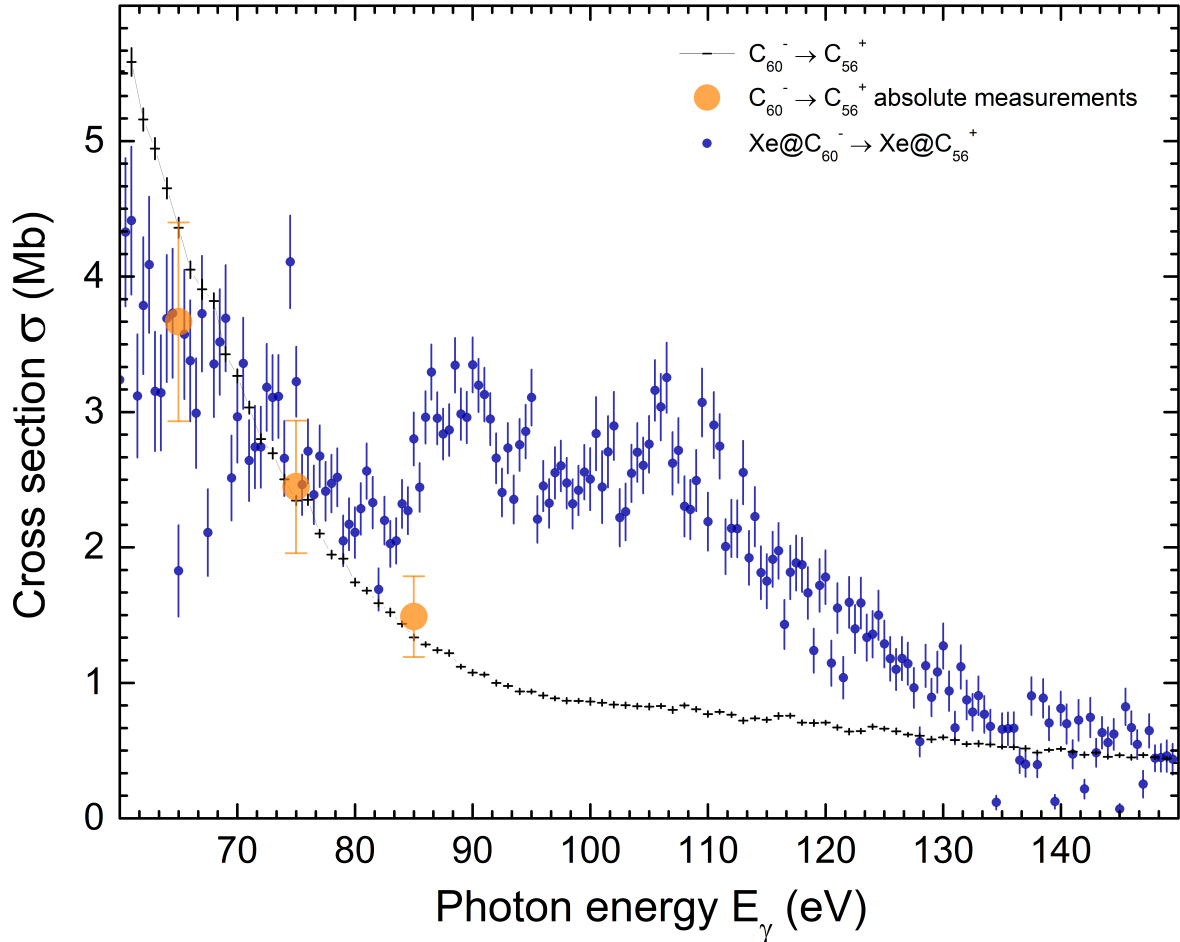


Figure 6.1.: Experimental cross-section data for double photoionization with fragmentation of endohedral fullerene ions $\text{Xe@C}_{60}^- \rightarrow \text{Xe@C}_{56}^+$ (solid blue circles with statistical error bars) put to an absolute scale by matching the cross-section spectrum of the corresponding empty-cage photoreaction $\text{C}_{60}^- \rightarrow \text{C}_{56}^+$ (black crosses with statistical error bars). The experimental empty-cage data are accompanied by the absolute measurements (large, solid orange circles with error bars) that were used in turn to normalize the empty-cage spectrum. As a consequence of low count rates, the statistical scatter of the spectral endohedral data is considerable outside the energy range 75–135 eV.

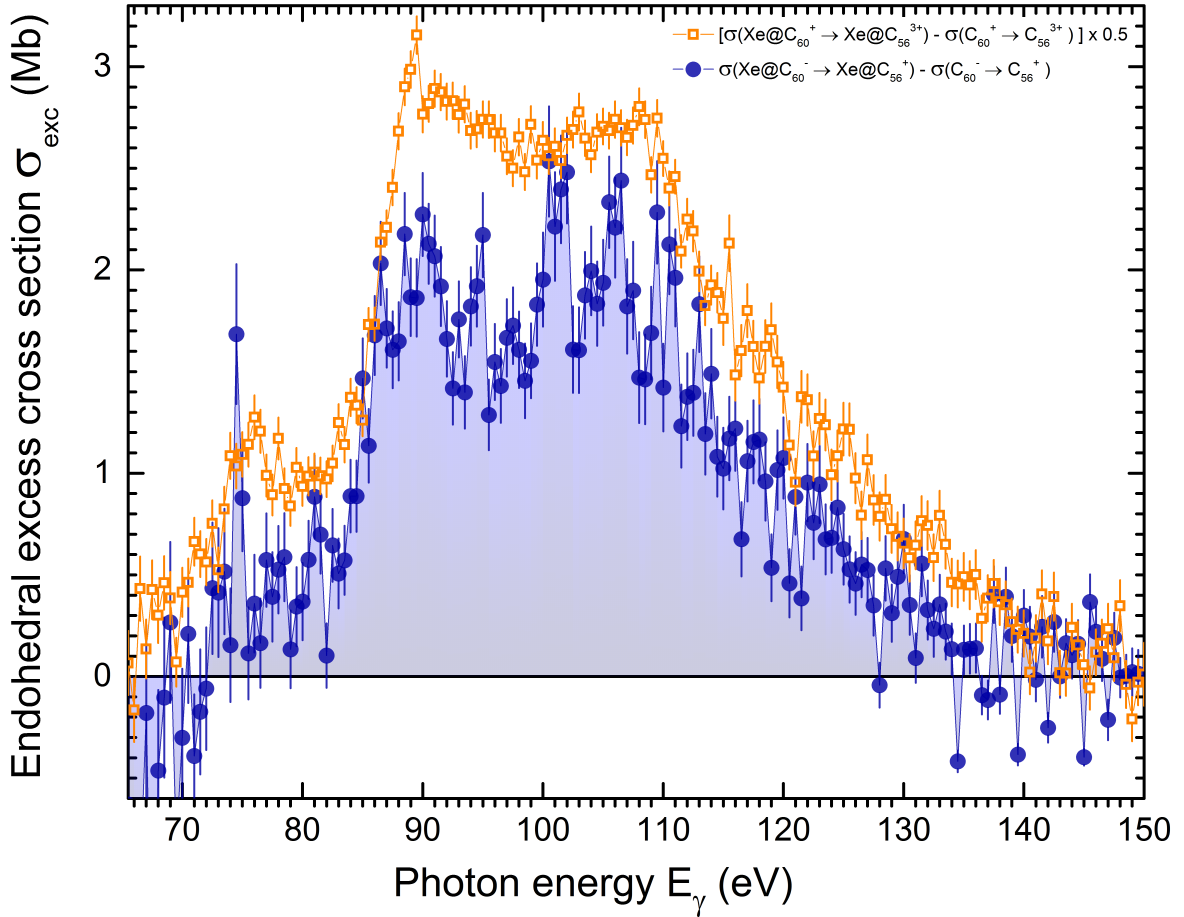


Figure 6.2.: Endohedral excess cross section (full blue circles with statistical error bars) in the $\text{Xe@C}_{60}^- \rightarrow \text{Xe@C}_{56}^+$ reaction channel obtained by subtracting the cross section of the corresponding empty-cage reaction $\text{C}_{60}^- \rightarrow \text{C}_{56}^+$ after putting both channels to an absolute scale. For comparison, the corresponding reaction channel (scaled down to 50% of the absolute scale) published by Phaneuf et al. [1] is also shown (hollow orange square symbols with statistical error bars).

6.2. Double ionization of Xe@C_{60}^- ions without fragmentation

Due to shorter integration times per photon energy, the statistical uncertainties in this reaction channel are larger than in the channel discussed in the previous subsection.

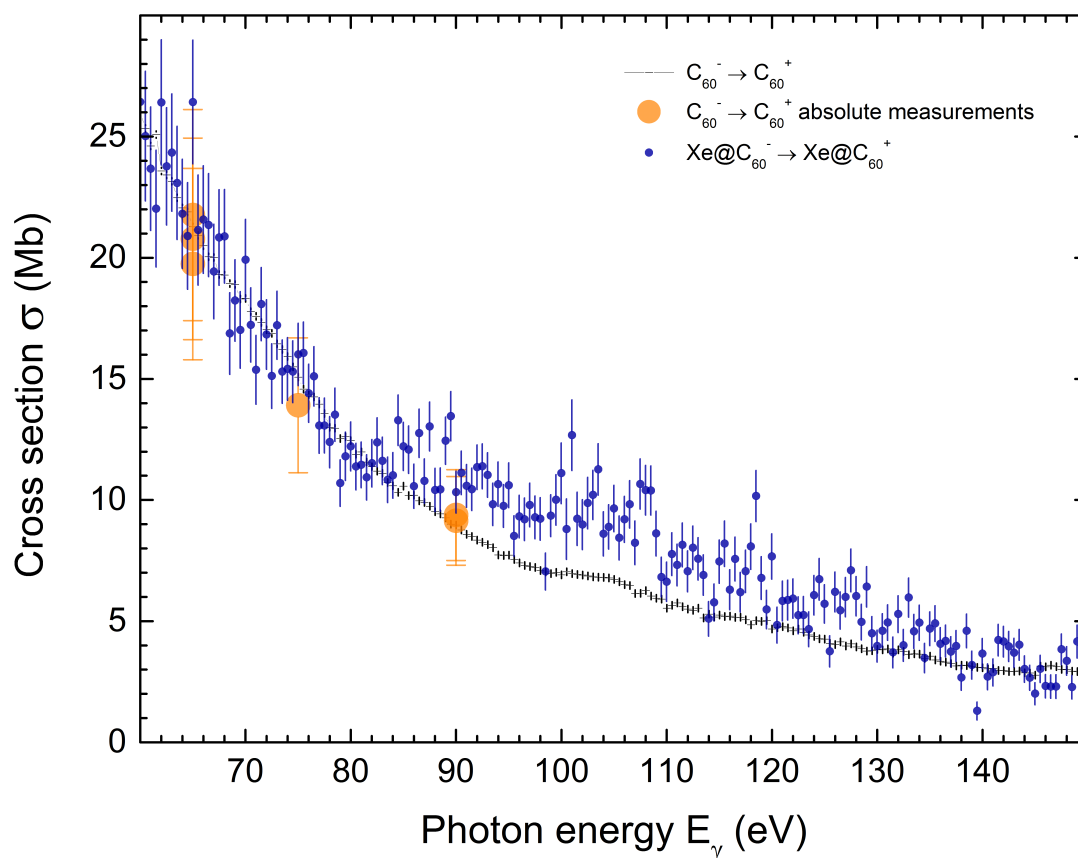


Figure 6.3.: Cross-section data for double photoionization of endohedral fullerene ions ($\text{Xe@C}_{60}^- \rightarrow \text{Xe@C}_{60}^+$, solid blue circles) scaled to match cross-section spectra of the corresponding empty-cage photoreaction ($\text{C}_{60}^- \rightarrow \text{C}_{60}^+$, black crosses). The empty-cage measurements are scaled to match absolute values (big, light grey circles) of the empty-cage photoreaction in turn.

The overall shape of the excess resembles the findings in the double ionization channel of positively charged primary ions published by Phaneuf et al. [1]. From the endohedral excess cross section in this photoreaction channel, an oscillator strength of $f=0.97\pm 0.17$ is inferred. In the case of negative ions, the non-fragmented double-ionization photoreaction channel appears to exhibit a xenon oscillator-strength contribution at least comparable to that in the Xe@C_{56}^{1+} product channel if not larger. This finding is in contrast to what was found studying double ionization photoreactions of positive ions: Here, the Xe@C_{56}^{3+} product channel shows the biggest xenon oscillator strength. Since the statistical accuracy of negative ion measurements is inferior to the corresponding positive ion data, this finding is not more than a hypothesis.

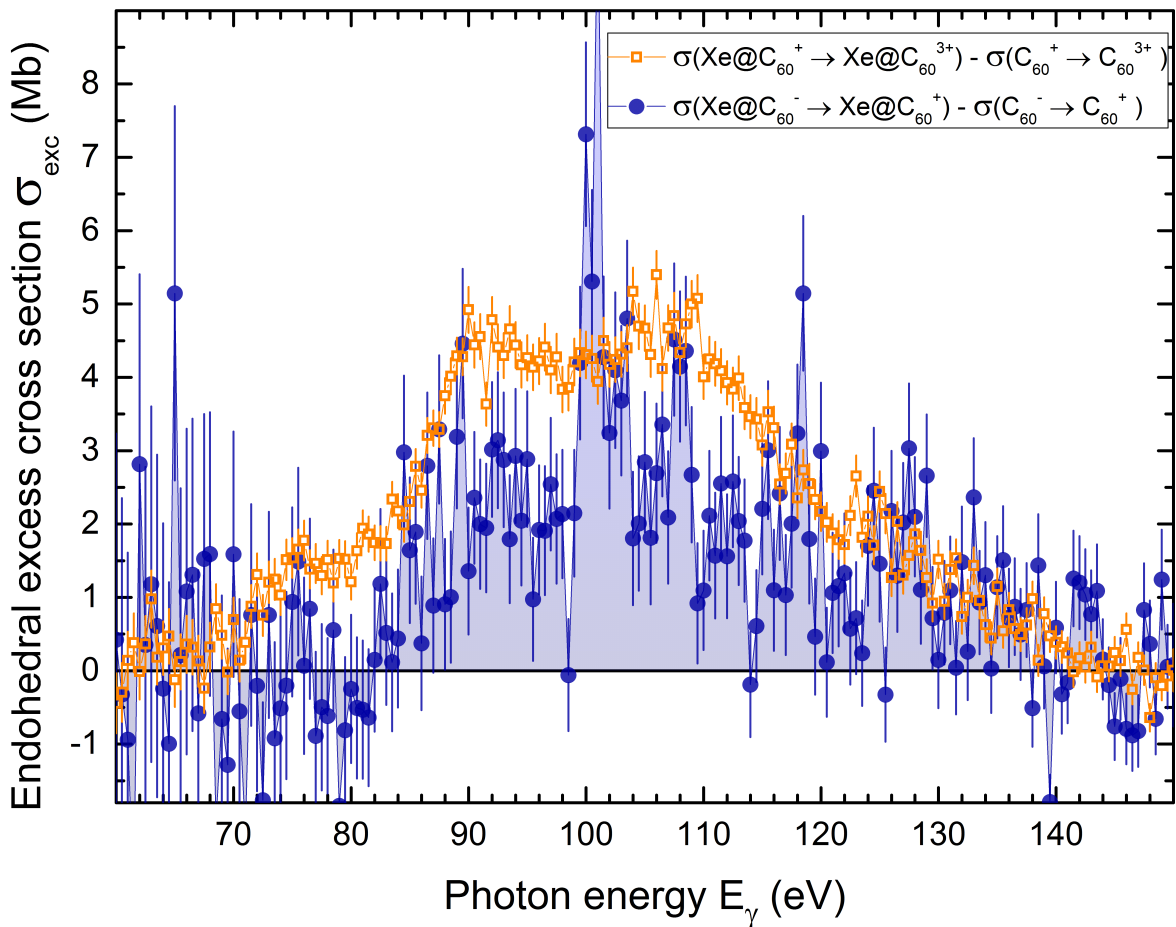


Figure 6.4.: Endohedral excess cross section (full blue circles) in the $\text{Xe@C}_{60}^- \rightarrow \text{Xe@C}_{60}^+$ reaction channel obtained by subtracting the cross section of the corresponding empty-cage reaction $\text{C}_{60}^- \rightarrow \text{C}_{60}^+$ after putting both channels to an absolute scale. For comparison, the corresponding reaction channel (also on an absolute scale) published by Phaneuf et al. [1] is also shown (hollow orange square symbols).

6.3. Double ionization of C_{70}^- ions

Besides endohedral and empty C_{60} fullerene species, one photoreaction channel of C_{70}^+ fullerene ions has been investigated. C_{70} is present as a contaminant in C_{60} sample material and with a molecular mass $u=840$ u it is found in relative proximity to $^{136}\text{Xe}@C_{60}$. Figure 6.5 shows scan measurements for double ionization of C_{70}^+ . As expected, the C_{70} cross section is smooth and similar to that of C_{60} in this photon energy range.

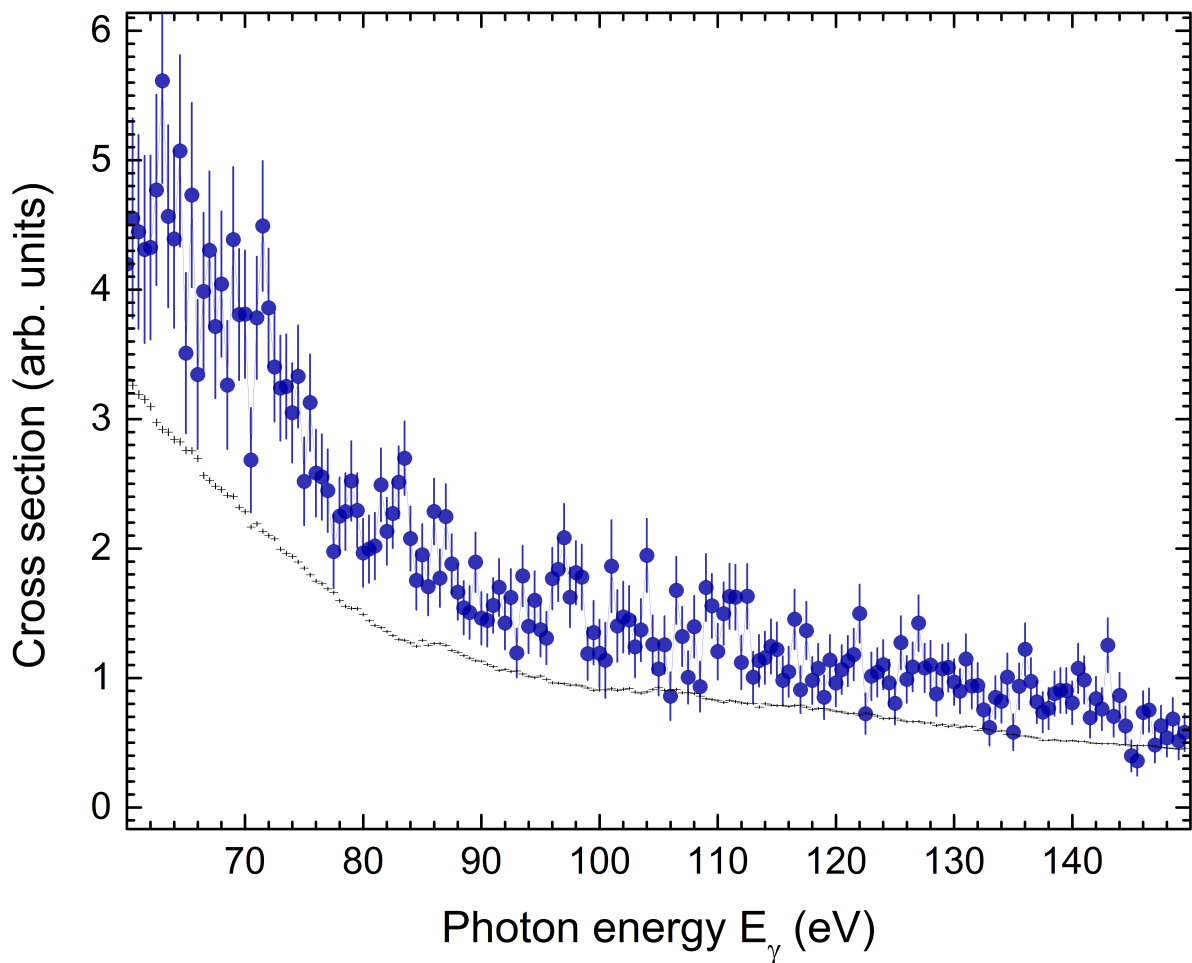


Figure 6.5.: Relative cross section for double photoionization of C_{70}^- primary ions (solid blue circles) in comparison with that of C_{60}^- (black crosses). In the absence of absolute measurements for C_{70} photoreactions, only qualitative conclusions can be drawn.

6.4. Closing discussion of the results for fullerene anions

A potential consequence of a change of the sign of the endohedral fullerene charge could be an energy shift of the onset of spectral features such as ionization thresholds and resonances of the xenon atom that is encapsulated inside the charged spherical fullerene cage. In the simplest approximation, the underlying idea is that the xenon atom is surrounded by the Coulomb potential of the charged spherical fullerene shell. As a consequence of this additional potential, the apparent ionization energy of the encapsulated xenon atom is shifted. However, when looking for a shift of the xenon-4d ionization onset one encounters several difficulties: First, the onset is not a sharp threshold like for direct ionization but the smooth boundary of a broad resonance. Second, with about 68 eV, the xenon-4d onset is found in an energy range where the statistical uncertainty of the measurements is substantial. Third, confinement oscillations cause the xenon-4d feature to change its shape. In conclusion, no energy shift of spectral xenon-4d features could be verified when comparing double ionization measurements for Xe@C_{60}^- and Xe@C_{60}^+ . On the other hand the statistical uncertainty of the experimental data does not allow to unambiguously exclude a potential small energy shift of spectral features (more detailed considerations on potential energy shifts of spectral features can be found in section 7.2.3).

The experimental studies demonstrated the presence of an endohedral signal in the double-ionization photoreaction cross sections of negatively charged endohedral fullerenes Xe@C_{60}^- . The overall shape of the cross-section spectra of the new data for these negative ions is close to the shape found for the corresponding photoreaction spectra of positive ions as published by Phaneuf et al. [1]. Since the accuracy of the measurements with negative ions is not superior to the published data for positive ions, the shape of the excess cross section could not be refined further. However, it is a remarkable finding that the xenon-4d excess cross section seems to show confinement oscillations identical to the observations made for reactions of positive ions within the statistical accuracy. One could conclude that the confinement resonances are not sensitive to the sign of the charge of the cage. On the other hand, the xenon-4d oscillator strength found in the double-ionization of negative fullerene ions Xe@C_{60}^- accounts to only about half the strength that Phaneuf et al. have reported for that reaction of their positively charged counterparts. The finding that the xenon 4d oscillator strength is apparently distributed unequally between positive and negative primary ions contradicts the assumption of symmetry in charge.

7. Photoionization and photofragmentation of $\text{Lu}_3\text{N}@C_{80}$

The idea behind the $\text{Lu}_3\text{N}@C_{80}$ investigations was to extend the photoionization studies on endohedral fullerenes towards another molecule species offering the prospect of finding both a cross-section signature of the encapsulated atoms and potentially also effects of the confinement on this signature. The investigations started with the search for a suitable species of endohedral fullerenes (see below). As a result, $\text{Lu}_3\text{N}@C_{80}$ was selected for the investigations. The first goal was to search for the predicted lutetium-3d threshold signature in the photoionization cross section spectra. Consecutive questions would address the potential modifications of the spectral shape of the encapsulated atoms due to confinement. However, the $\text{Lu}_3\text{N}@C_{80}$ study also wanted to answer the question how the carbon cage in turn is affected by the presence of the encapsulated atoms. For this purpose, the investigations dealing with this question focused on an energy range that comprises the carbon K-shell threshold. Based upon the photoionization cross section spectra at the carbon K-edge, the $\text{Lu}_3\text{N}@C_{80}$ behavior was to be compared with the carbon K-edge behavior of other fullerene species.

The nanoscale systems $\text{Sc}_3\text{N}@C_{80}$ and $\text{Lu}_3\text{N}@C_{80}$ are “members” of a category of endohedral fullerenes sometimes referred to as “trimetashpheres” (TMS), a subcategory of endohedral metallofullerenes (EMF). The most common TMS fullerene type consists of a trigonal, planar nitride molecule inside the almost-spherical 80-member fullerene C_{80} acting as a cage. The encapsulated trimetallic nitride molecules usually comprise three rare-earth-element (REE) atoms (e.g. Sc, Y, Gd, Tb, Dy, Ho, Er, Tm, Lu) centered around a nitrogen atom forming an endohedral fullerene $(\text{REE})_3\text{N}@C_{80}$. Stevenson et al. [77] have reported the synthesis of $\text{Sc}_3\text{N}@C_{80}$ in 1999. Dunsch et al. [78] have shown TMSs of all cage sizes with an even number of carbon atoms from C_{68} to C_{96} (with the exception of C_{72} , C_{74} , and C_{76}).



Figure 7.1.: Characteristic colors of fullerenes dissolved in toluene: $\text{Lu}_3\text{N}@C_{80}$ (on the left; yellowish-brownish) and C_{60} (on the right; purple).

The TMS-category endofullerenes exhibit a couple of characteristics which makes using them favorable over using other endohedral metallofullerenes like Li@C_{60} or Ce@C_{82} for both research and applications: First of all, TMSs are particularly stable; even more stable than C_{60} , the most stable pristine fullerene. However, Ross et al. [66] claim that both Lu_3N and C_{80} alone are unstable concluding that they cannot exist individually. In the case of C_{80} this is in contrast to the findings of Hennrich et al. [79]. These authors reported the isolation and purification of C_{80} and subsequent photoemission measurements using a solid C_{80} sample accompanied by a detailed investigation of the symmetry of C_{80} . Disregarding this controversy, one can state that $\text{Lu}_3\text{N@C}_{80}$ is far more stable than C_{80} because the additional molecule inside stabilizes the surrounding carbon cage from within by charge transfer [66,77]. Ge et al. have used this kinetic stability for otherwise impossible chemical enrichment of endohedral trimetallic nitride fullerenes [48]. Furthermore, with nuclear-magnetic-resonance measurements (NMR) it has been demonstrated that the nitride molecule moves freely inside the cage on μs timescales (see Stevenson et al. [77], Guha et al. [80], and references cited therein; NMR timescales have been tabulated by Bryant [81]). Consequently, the trinitride molecule cannot be located at a certain location inside the cage like in the case of, e.g., Li@C_{60} . The stability of the endohedral fullerene $(\text{REE})_3\text{N@C}_{80}$ in contrast to the instability of the separate C_{80} cage and the trimetallic nitride $(\text{REEN})_3\text{N}$ suggest the conjecture that these ingredients do not form stable exohedral fullerenes. The issue of exohedral fullerenes, particularly Li@C_{60} , was raised by Saunders et al. [56]. Stevenson et al. have presented a method for the separation of different isomers in which C_{80} can occur [82]. In conclusion, TMSs are a good choice for experiments with respect to sample production, purification, stability and commercial availability.

Few species of endohedral fullerenes are commercially available today. Restrictions are given by the stability of the endohedral fullerene (only certain combinations of cage and encapsulated particle are stable) and the availability of a process suitable for the synthesis of a desired species. Since the common production methods only yield small fractions of the desired endohedral fullerenes, purification is a further complication. For the present study, commercially available samples of endohedral $\text{Lu}_3\text{N@C}_{80}$ and $\text{Sc}_3\text{N@C}_{80}$ fullerene powder with a purity of 35% were used. Complete purification was achieved by in-situ mass separation (as described in section 4.2.4).

7.1. Ionization-threshold energy predictions

Henke et al. have semi-empirically determined predictions, among other quantities, for photoabsorption cross sections for an extensive set of elements and a wide range of photon energies based on the experimental data available in 1993 [83]. Their predictions give an idea at which energies to look for thresholds in the photoreaction channels observed. Figure 7.2 shows the prediction for $\text{Lu}_3\text{N}@C_{80}$.

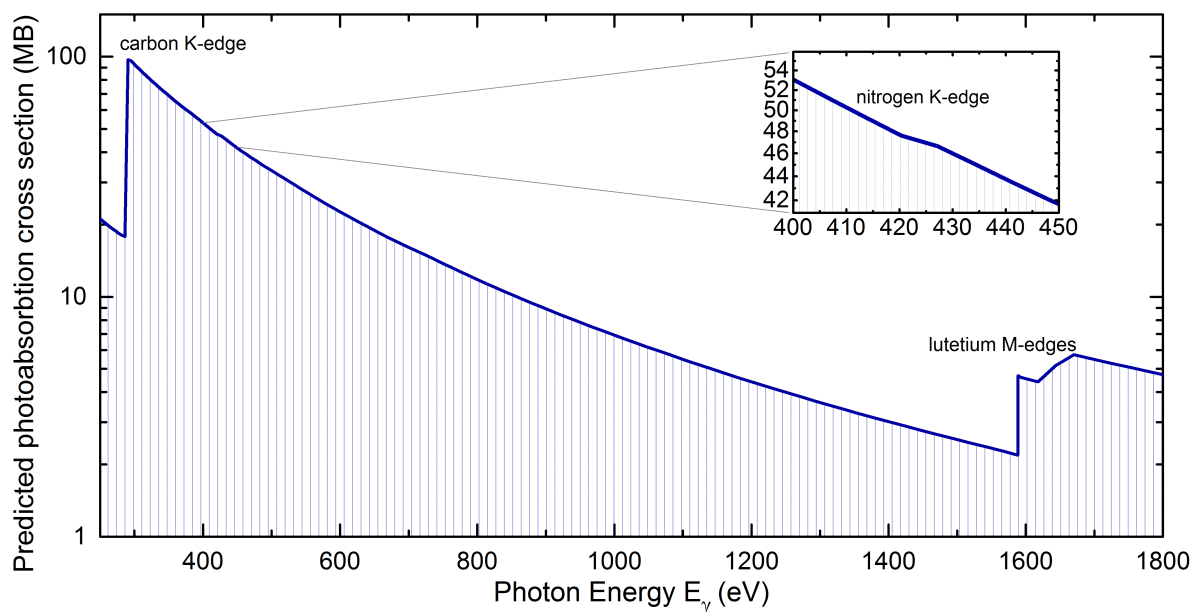
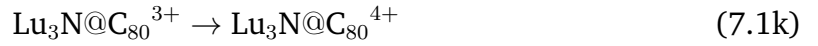
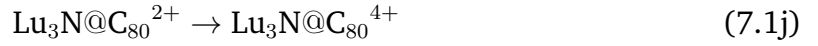
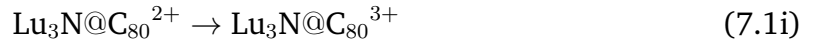


Figure 7.2.: $\text{Lu}_3\text{N}@C_{80}$ photoabsorption cross section estimate based on the tables provided by Henke et al. [83]: The plot shows the sum of the cross sections for carbon, lutetium, and nitrogen weighted according to their relative numbers in one endohedral fullerene molecule ($80\times\text{C}$, $3\times\text{Lu}$, and $1\times\text{N}$).

7.2. Photoreaction measurements of $\text{Lu}_3\text{N@C}_{80}$

Relative cross-sections for eleven different $\text{Lu}_3\text{N@C}_{80}^{q+}$ photoreaction channels at energies around the carbon K-shell threshold (280-330 eV), the nitrogen K-shell threshold (390-435 eV), and the lutetium M-shell threshold (1500-1700 eV) are presented. The ion beam preparation for these measurements has been detailed in section 4.2.4. In particular, relative cross sections for the production of the following heavy fragments (right) from the indicated primary particles (left) have been measured in selected photon energy ranges:



The procedures detailed in Ref. [46] were employed. The PIPE setup allows for the determination of absolute cross sections. However, for the present measurements, the beam-overlap factors which are required for obtaining absolute cross sections were not determined because of time constraints. Nevertheless, different product-ion yield spectra are still on the same relative cross section scale and can, therefore, be compared to one another quantitatively since the beam overlap is independent of the product channel investigated. Moreover, the beam overlap can safely be assumed to be independent of photon energy over the narrow photon energy ranges that were scanned within the $\text{Lu}_3\text{N@C}_{80}$ study. Consequently, the distribution of oscillator strength among the different product channels can be extracted from the measured spectra although they are not on an absolute scale.

7.2.1. Experimental conditions

For the photoionization measurements presented in this chapter, the photon-energy resolution varied between 100 meV and 220 meV with an uncertainty of ± 20 meV at a photon energy $E_\gamma = 300$ eV. Investigations showed that varying the resolution had no influence on the beam overlap in this energy region. Table 7.1 lists all photon flux values for monochromator slit settings and photon energies that have been used during the Lu₃N@C₈₀ beamtime including the first exploratory measurements. The actual measurements presented in section 7.2.2 and following have been carried out with a nominal exit slit width of 2000 μm .

The photon energy scale for the cross-section measurements described below was calibrated by first applying a Doppler correction to take care of the ion-velocity-related energy shift. Thereafter, the monochromator calibration was determined by separately measuring known resonances of C^{q+} and Ne⁺ and compared with literature values [84–86]. The resulting systematic uncertainty of the present energy scale is ± 0.05 eV [87].

E_γ	Slit Width	Photon Flux
285 eV	1500 μm	$3.78 \times 10^{12} \text{ s}^{-1}$
285 eV	2000 μm	$4.39 \times 10^{12} \text{ s}^{-1}$
285 eV	3000 μm	$4.51 \times 10^{12} \text{ s}^{-1}$
300 eV	2000 μm	$6.97 \times 10^{12} \text{ s}^{-1}$
300 eV	3000 μm	$7.08 \times 10^{12} \text{ s}^{-1}$
320 eV	2000 μm	$1.01 \times 10^{13} \text{ s}^{-1}$
400 eV	2000 μm	$1.69 \times 10^{12} \text{ s}^{-1}$
1600 eV	2000 μm	$1.35 \times 10^{12} \text{ s}^{-1}$

Table 7.1.: Photon flux values delivered to the PIPE endstation by PETRA III beam line P04 during the Lu₃N@C₈₀ beam time. The slit width refers to the nominal setting of the monochromator exit slit at the time of the present measurements. A proper calibration of the slit width became available later.

7.2.2. Results for photon energies 280 to 330 eV

In this section, relative cross sections in the photon energy range 280–330 eV are presented for seven reaction channels [Eqs. (6.1a)–(6.1d), (6.1i), (6.1j), and (6.1k)]. The investigated energy range comprises the carbon K-shell threshold.

The count rates for signal plus (s+b) background and background (b) were determined by independent measurements for each product channel individually. Table 7.2 lists count rates obtained for the relative scaling (described in section 4.2.1) of the different reaction channels and Fig. 7.3 illustrates the relative intensities visually. Signal-to-background ratios ranged from 4:1 up to 65:1.

The validity of the background rates measured for the relative calibration of the spectra was thoroughly investigated for the whole energy range. The cross-section spectra have been corrected for these background rates and an uncertainty of less than $\pm 20\%$ is estimated for the determined background intensity. Since the background is small in comparison to the signal, this background uncertainty does not significantly contribute to the uncertainty of the measured relative cross sections.

	I_{s+b}^+	s+b	I_b^+	b	E_γ	s/b
1+ → 2+	7.8	1594	7.6	176	292	7.84
** 1+ → 2+	2.5	68	2.8	12	300	4.85
1+ → 3+	5.9	1074	4.8	13	292	65.70
1+ → 4+	2.5	80	2.9	16	300	5.33
2+ → 3+	9.8	1102	9.3	137	292	6.58
2+ → 4+	13.7	930	12.6	77	301	10.10
* 3+ → 4+					*292	* 5.50

Table 7.2.: Signal and background determination: Counts for signal plus background (s+b) and background (b) in different product channels for a period of 100 s. The intensity in channel * was not recorded during the calibration measurements and, therefore, has a larger uncertainty. A fragmentation channel (Lu₃N@C₇₈ products) is denoted by **. I_{s+b}^+ and I_b^+ denote the primary ion current in units of pA at the time of the measurement for signal plus background and background only, respectively. The photon energy E_γ is given in units of eV.

7. Photoionization and photofragmentation of $\text{Lu}_3\text{N@C}_{80}$

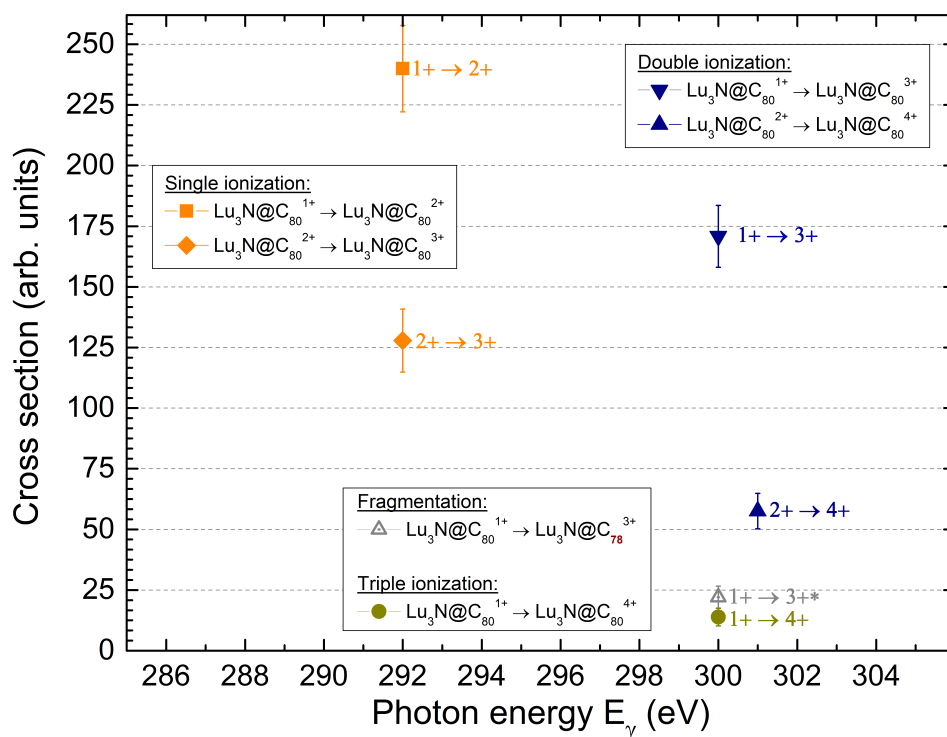


Figure 7.3.: Visual illustration of the relative calibration data points listed in Table 7.2.

Photoionization spectra

Figure 7.4 summarizes the results for singly charged primary ions [Eqs. (6.1a), (6.1b), and (6.1d)]. Fig. 7.5 shows data obtained with doubly and triply charged primary ions [Eqs. (6.1i), (6.1j), and (6.1k)] as well as a fragmentation channel [Eq. (6.1c)].

For the cross-section scale of the single ionization of the triply-charged primary ion $\text{Lu}_3\text{N@C}_{80}^{3+} \rightarrow \text{Lu}_3\text{N@C}_{80}^{4+}$, a larger uncertainty of (conservatively) up to $\pm 50\%$ has to be admitted. The reason is that this channel's intensity was not recorded during the calibration measurements. The associated spectrum is shown in panel (b) of Fig. 7.5.

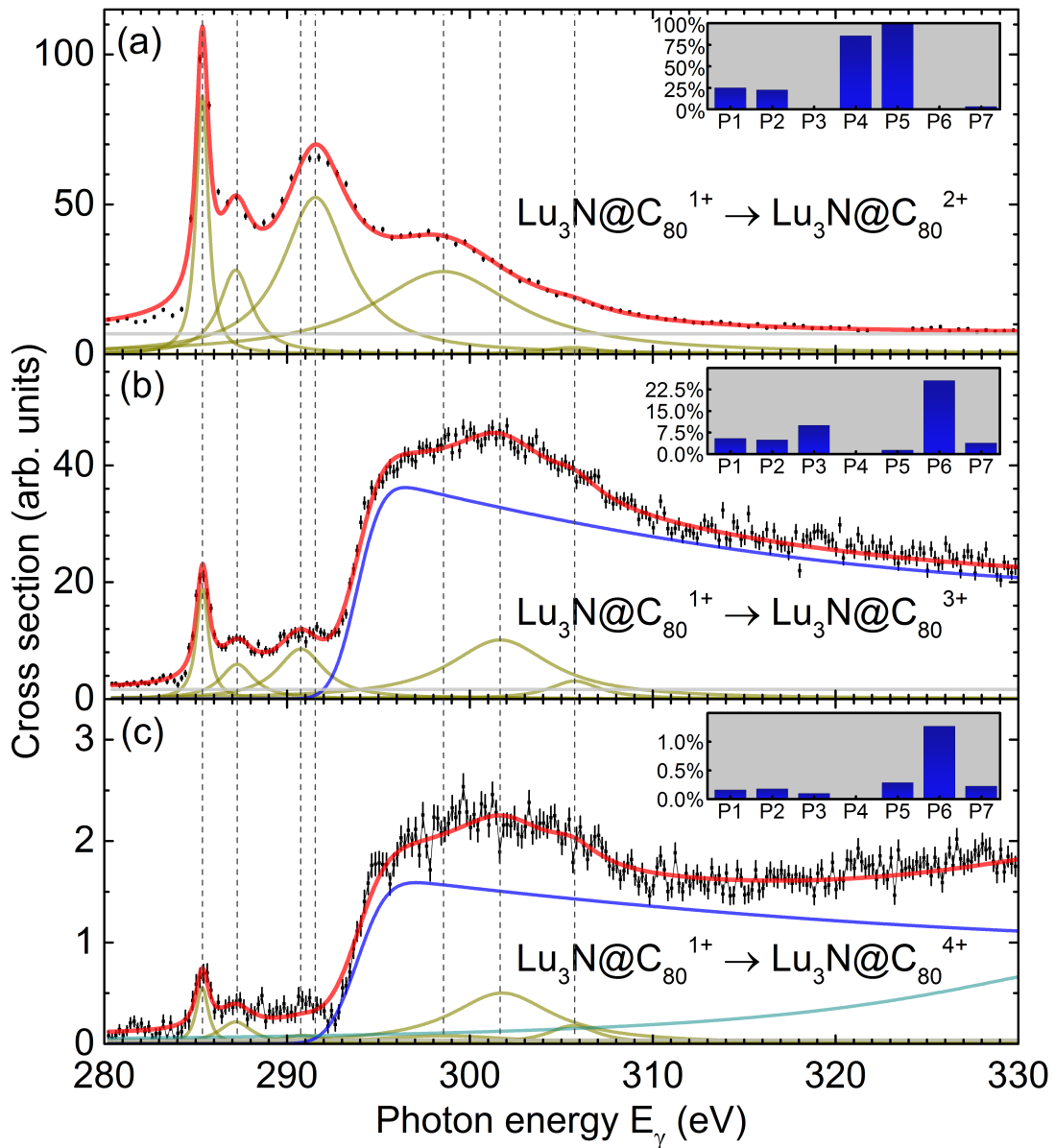


Figure 7.4.: Relative cross-sections for photoionization of $\text{Lu}_3\text{N@C}_{80}^+$ primary ions. (a) single ionization $\rightarrow \text{Lu}_3\text{N@C}_{80}^{2+}$, (b) double ionization $\rightarrow \text{Lu}_3\text{N@C}_{80}^{3+}$, (c) triple ionization $\rightarrow \text{Lu}_3\text{N@C}_{80}^{4+}$. Black square symbols with error bars represent the experimental data. Thick red lines correspond to fitting results composed of seven Voigt peak profiles (gold lines), a constant background (light grey line) and a 2nd order polynomial convoluted with a Gaussian (blue line) to model the K-shell threshold behavior. In the case of triple ionization, a wide eighth peak was needed for modeling (cyan line). Vertical dashed lines illustrate the peak positions. We observe the same peak positions in the different product channels. The insets show the relative contributions of each resonance to the different spectra. Table 7.3 lists the relations of peak areas.

7. Photoionization and photofragmentation of $\text{Lu}_3\text{N@C}_{80}$

A common set of resonances with individual widths and energies seems to make up for the most prominent structures in all spectra with the first and most outstanding resonance occurring at 285 eV. Therefore, it was attempted to model each spectrum of product ions with a common set of basis functions.

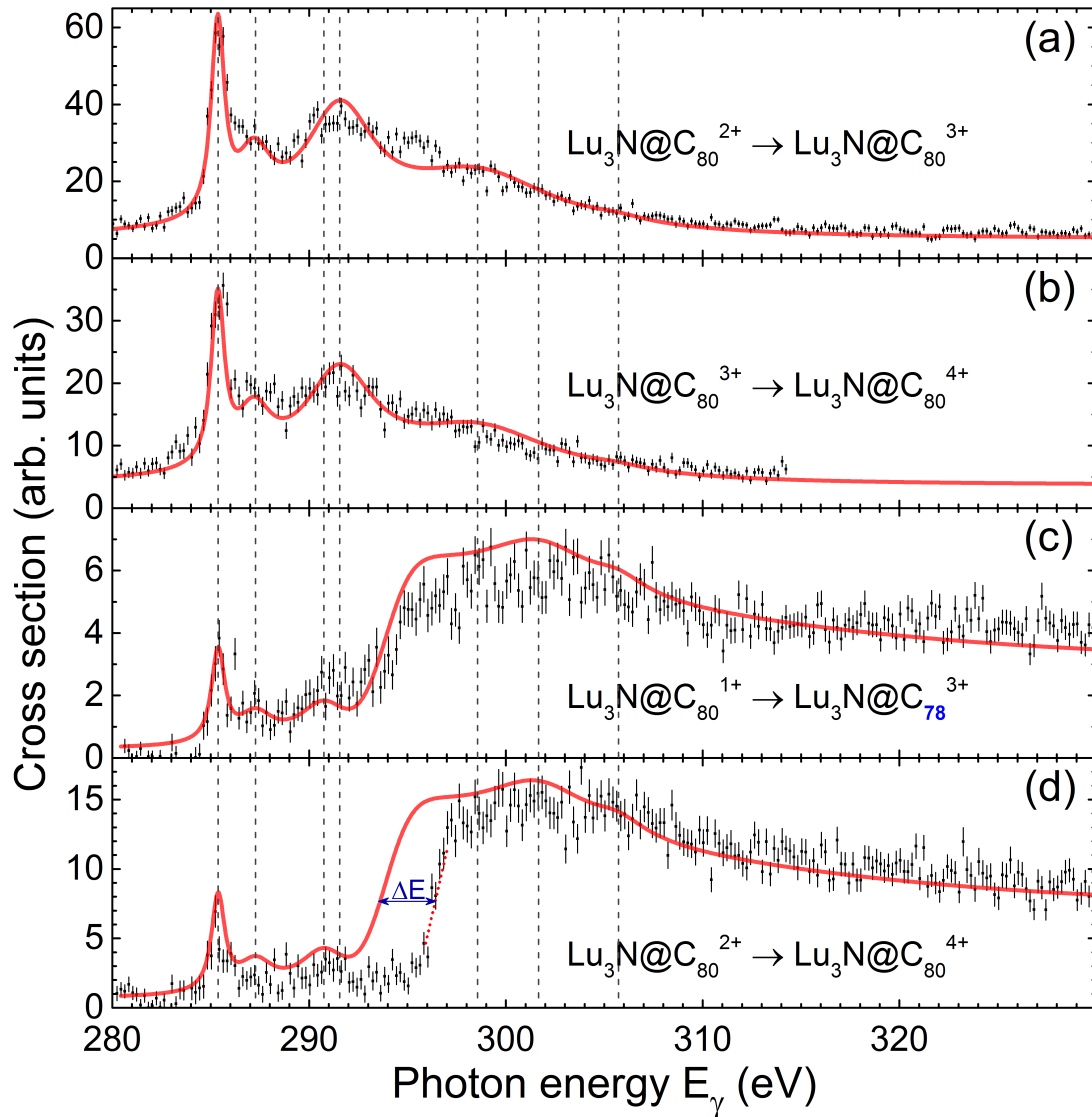


Figure 7.5.: Relative cross-sections of photoreactions for singly, doubly, and triply charged $\text{Lu}_3\text{N@C}_{80}$ ions: (a) $\text{Lu}_3\text{N@C}_{80}^{2+} \rightarrow \text{Lu}_3\text{N@C}_{80}^{3+}$, (b) $\text{Lu}_3\text{N@C}_{80}^{3+} \rightarrow \text{Lu}_3\text{N@C}_{80}^{4+}$, both accompanied by the scaled fitting result from Fig. 7.4(a); (c) $\text{Lu}_3\text{N@C}_{80}^{1+} \rightarrow \text{Lu}_3\text{N@C}_{78}^{3+}$ (fragmentation channel), (d) $\text{Lu}_3\text{N@C}_{80}^{2+} \rightarrow \text{Lu}_3\text{N@C}_{80}^{4+}$ (with the threshold shift highlighted) both accompanied by the individually scaled fitting results from Fig. 7.4(b). See text for scaling factors.

Fitting procedure

The product-ion spectra were modeled as a sum of seven peak features (Voigt profile resonances, solid amber lines in Fig. 7.4, see Table 7.3), a threshold feature (second order polynomial multiplied with a step function and convoluted with a Gaussian, blue line) and a constant background modeling the carbon L-shell contribution to the measured spectra (gray line). The relative strengths of the resonance peaks P1–P7 found in each spectrum are given by the vertical blue bars in the insets. In each inset the peak areas are normalized to the area of the strongest peak (P5) in Fig. 7.4(a).

In an iterative process, peak positions and natural widths were determined from the respective channels of their most prominent appearance. The parameters for P4 and P5 were determined from Fig. 7.4(a) data and the parameters for the other resonance features were determined from Fig. 7.4(b) data. Vertical lines (dashed) mark the peak positions (see Table 7.3).

For the construction of a suitable basis function representing the necessary threshold step contributions to the observed cross sections, the convolution of a step function with a 4-eV Gaussian was found to be appropriate. While the experimental bandwidth was smaller than 0.25 eV, a 0.25-eV Gaussian was chosen to conservatively simulate the experimental response function in the fitting procedure. The choice of this width had no significant influence on the results because all features P1–P7 are much broader than the assumed 250 meV bandwidth. To model triple ionization, another very wide feature was needed (light cyan, see Fig. 7.4(c)).

Fitting results and findings

The set of resonances that one can identify in every investigated reaction channel may be explained by resonant excitation of a K-shell electron and a subsequent Auger process that occurs when the hole in the K-shell is filled. An Auger process removing a single electron from the ion is more probable than an Auger process removing two electrons. As a result, these resonance peaks are more intense in single ionization [Fig. 7.4(a)] than in double ionization [Fig. 7.4(b)]. In the triple ionization channel [Fig. 7.4(c)] the intensity is much weaker than in double ionization.

In the double and triple ionization channels, one can observe a threshold at about 294 eV which is not visible for single ionization. This ionization threshold is expected to originate from direct photoionization of one of the carbon atoms. From the fact that there is no visible threshold in single ionization, one can conclude that the probability for the K-shell hole to decay via an Auger process is much larger than its probability for a radiative decay: Similar to K-vacancy production in a neutral carbon atom, the direct

7. Photoionization and photofragmentation of $\text{Lu}_3\text{N@C}_{80}$

	E_γ (eV)	FWHM (eV)	$A_{s.i.}$	$A_{d.i.}$	$A_{t.i.}$
P1	285.37 ± 0.52	0.58 ± 0.02	24.82%	5.45%	0.16%
P2	287.19 ± 0.45	2.71 ± 0.20	22.39%	4.91%	0.18%
P3	290.82 ± 1.14	* 2.91 ± 0.30	0.00%	10.02%	0.10%
P4	291.55 ± 0.21	* 4.37 ± 0.20	85.24%	0.02%	0.00%
P5	298.56 ± 0.99	9.72 ± 1.57	100.00%	1.37%	0.29%
P6	301.77 ± 0.51	* 6.76 ± 0.70	0.00%	25.55%	1.27%
P7	305.65 ± 1.40	3.65 ± 1.45	3.23%	3.89%	0.26%

Table 7.3.: Properties of the group of resonances used for fitting spectra of the seven investigated channels around the carbon K-threshold energy as shown in Figs. 7.4 and 7.5. The Lorentzian widths of the peaks marked with an asterisk were determined from a single reaction channel, whereas in all other cases the peaks were prominent in two or three channels and therefore their widths could be obtained by simultaneously fitting the results obtained for more than one channel. Columns $A_{s.i.}$, $A_{d.i.}$, and $A_{t.i.}$ list relations of the peak areas in the single-ionization [s.i., Fig. 7.4(a)], double-ionization [d.i., Fig. 7.4(b)], and triple-ionization [t.i., Fig. 7.4(c)] reaction channels, respectively. The area of the strongest peak was normalized to 100%.

K-shell ionization of one atom of the C_{80} carbon cage almost always removes two or more electrons. Hence, single ionization after K-shell photoionization is very unlikely. Higher order processes can result in the loss of further electrons.

The distribution of area among the peaks (insets of Fig. 7.4) in channels exhibiting a threshold behavior [namely, double (b) and triple ionization (c) channels] is similar. The area distribution for single ionization (a), however, is strikingly different from (b) and (c). In detail: For double and triple ionization, P6 is dominating by far. P4 is very weak and P5 and P7 areas just form a low pedestal to P6. However, the three features P1, P2, and P3 as a group are stronger in double ionization as compared to triple ionization. For single ionization, P3, P6, P7 are very weak but P4 and P5 are very strong yet similar in intensity. It is common to all channels that P2 covers a larger area than P1. The peaks P1, P2, and P5 are present in every channel.

The results shown in Fig. 7.5 were not individually modeled with a fit. Instead, the fitting results for single and double ionization of $\text{Lu}_3\text{N@C}_{80}^+$ from Fig. 7.4 are plotted together with the corresponding spectra in Fig. 7.5 after scaling with constant (i.e., energy-independent) factors: 7.5(a) uses 57% and 7.5(b) uses 32% of the fitting result in 7.4(a); 7.5(c) uses 15% and 7.5(d) uses 36% of the fitting result in 7.4(b).

Panels (a) and (b) in Fig. 7.5 show relative cross sections for single-ionization processes. The overall shape of single ionization of $\text{Lu}_3\text{N@C}_{80}^{2+}$ agrees quite well with the fitting result from Fig. 7.4(a). The data for single ionization of $\text{Lu}_3\text{N@C}_{80}^{3+}$ forming

$\text{Lu}_3\text{N@C}_{80}^{4+}$ [Fig. 7.5(b)] do not have as good statistics as the preceding channels but overall, the fitting results from Fig. 7.4(a) also fit single ionization of $\text{Lu}_3\text{N@C}_{80}^{3+}$.

Figure 7.5(c) shows a hint on how the spectrum is modified if double ionization of $\text{Lu}_3\text{N@C}_{80}^+$ is accompanied by the loss of a carbon dimer C_2 . It appears that in the fragmentation channel P1 is stronger in relation to the height of the ionization threshold. In addition, the fragmentation spectrum slightly deviates from the fitting curve at higher energies.

Figure 7.5(d) shows relative cross sections for double ionization of $\text{Lu}_3\text{N@C}_{80}^{2+}$ together with the fitting result for double ionization of $\text{Lu}_3\text{N@C}_{80}^+$. This comparison is discussed in more detail below.

7.2.3. Ionization threshold shift

An endohedral fullerene ion consists of a particle inside a charged shell. There are studies on the structure of C_{80} (see, e.g., Khamatgalimov et al. [88]) but due to its relative sparsity in comparison to other fullerenes, the level of detail regarding the electronic structure of C_{80} is limited. Since C_{60} is the most common fullerene and its electronic structure has been explored in several studies, the qualitative reasoning will be based on C_{60} as a substitute for C_{80} . In the case of C_{60} , four electrons of each carbon atom are delocalized due to partial hybridization of the atomic orbitals (see Verkhovtsev et al. [89, 90]). Out of the 240 delocalized, quasi-free electrons (constituted of the $2s^2$ and $2p^2$ carbon valence electrons), 60 electrons are bound particularly weakly (see calculations by Davidson [91] and experimental verification by Sohmen et al. [92]). The levels of these electrons are spread over a narrow energy range of ± 3 eV. If one of these outer electrons is removed from the fullerene, there are still numerous outer electrons in the delocalized cloud in a degenerate or very similar level. Therefore, a first-order approximation of the consequences of removing one outer-shell electron from a fullerene can be reduced to the change of net charge. As a result, fullerene photoionization reactions with the same number of electrons n_e ejected but different initial charge states of the fullerene ion F^{q+} , say $\text{F}^{1+} \rightarrow \text{F}^{3+}$ or $\text{F}^{3+} \rightarrow \text{F}^{5+}$, show the same qualitative behavior because the number of electrons ejected $n=2$ is identical. Due to this unique nature of fullerene gas targets, observations are possible which are prohibited for atomic or molecular ion targets: In the atomic case, the ejection of an electron results in a new configuration with different parameters like charge radius etc.

When comparing double ionization of the singly charged primary ion [Fig. 7.4(b)] with double ionization of the doubly charged primary ion [Fig. 7.5(d)], one finds the measured ionization threshold energy is shifted by $\Delta W = (2.90 \pm 0.24)$ eV. The higher charge of Lu₃N@C₈₀²⁺ primary ions results in an increase of the attractive Coulomb potential that the fullerene shell of Lu₃N@C₈₀^{q+} exerts on the electron leaving the fullerene from its surface. Based on the radial Coulomb potential W_{pot} and the energy shift ΔW_{pot} of the threshold, we can provide an estimate for the radius R of the endohedral fullerene Lu₃N@C₈₀ under the assumption of a spherically symmetric cage:

$$\Delta W_{pot} = \frac{e \Delta q}{4\pi\epsilon_0 R} \iff R = \frac{e \Delta q}{4\pi\epsilon_0 \Delta W_{pot}} \quad (7.2)$$

where e is the elementary charge, ϵ_0 the electrical constant and $\Delta q = 2e - 1e = e$. With the above mentioned energy shift, an endohedral-fullerene charge radius of $(5.0 \pm 0.4) \times 10^{-10}$ m is inferred.

As far as the K-shell ionization threshold behavior is concerned, single-ionization cross-section plots all look alike regardless of the initial charge state. In contrast, the discrete ionization threshold present in double and triple ionization is sensitive to the charge state of the primary ion.

No such threshold shifting behavior can be found for valence-shell ionization of fullerenes because of the differences in spatial extend of the involved orbitals: While carbon K-shell ionization involves the 1s orbitals which are basically atomic orbitals localized at the carbon atoms, the valence-shell ionization involves the far-stretching non-localized molecular orbitals of the outer electrons of the fullerene molecule. So an electron knocked off the K shell is fully enclosed in the charge distribution of the valence shell of a fullerene ion whereas an electron in the valence shell is not.

7.2.4. Comparison with other fullerene species

Figure 7.6 compares the photoabsorption of different fullerene species near the carbon K edge with results of the present study. Each cross section was individually scaled such that the highest feature represents 100%.

Panel (d) shows the present photoionization data whereas panels (a), (b), (c), and (e) show photoabsorption data: (a) data for C₆₀ in the gas phase (black squares) [93] and for a solid (violet squares) [94], (b) results for solid C₇₀ [94], (c) data for solid C₈₀ [95], (d) cross-section data for single ionization (blue circles) and double ionization (orange squares) of Lu₃N@C₈₀⁺. The solid lines in panel (d) represent the fitting results for these channels [see Fig. 7.4 panels (a) and (b)]. Panel (e) shows data for graphite [94]. Since our datasets are sensitive to individual ionization channels whereas absorption

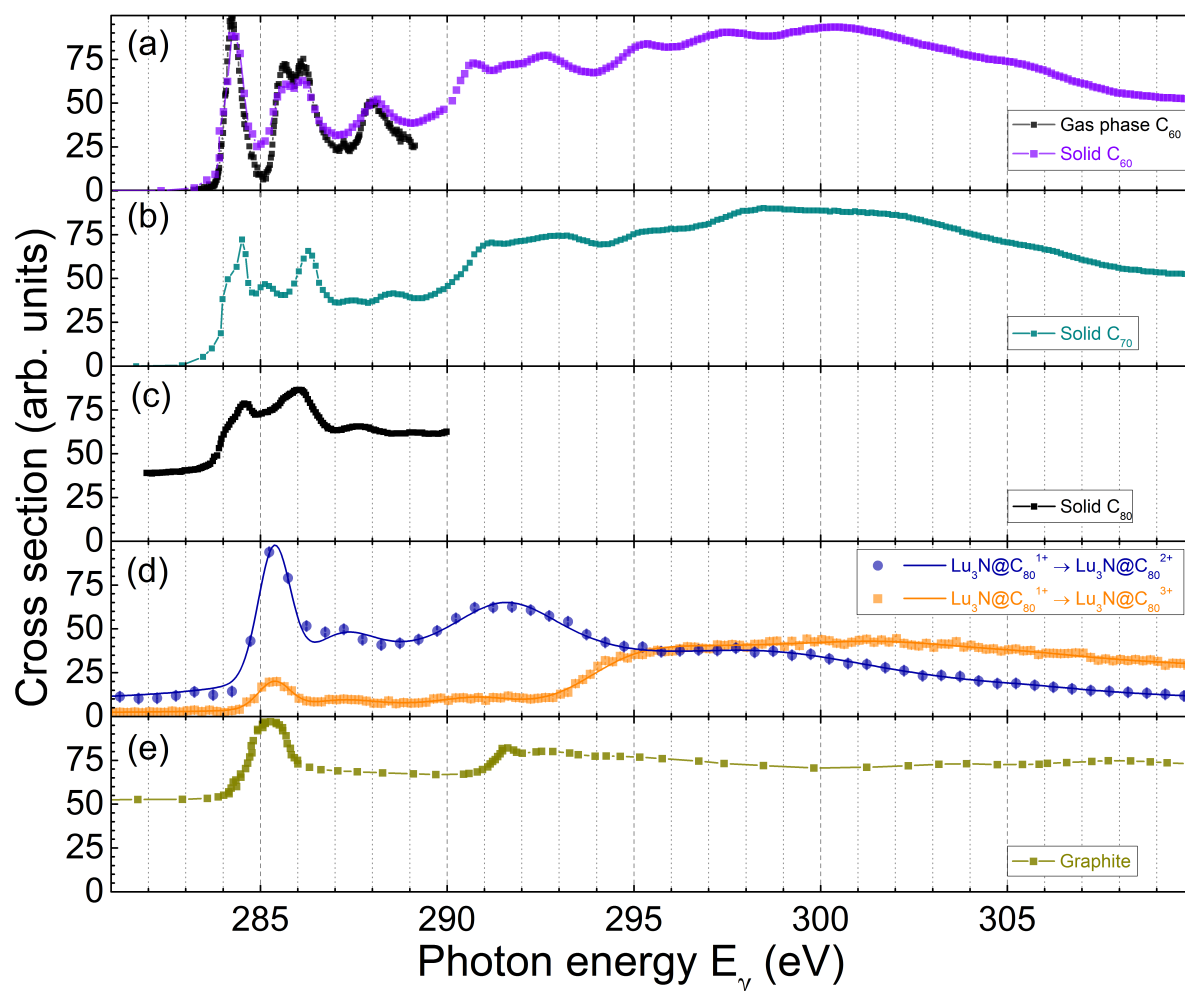


Figure 7.6.: Comparison of photoabsorption of a range of fullerene species around the carbon K-shell ionization threshold with cross-section data from the present study. Photoabsorption of (a) C_{60} in the gas phase (black squares) [93] and solid C_{60} (violet squares) [94], (b) solid C_{70} [94] (teal squares), (c) solid C_{80} [95] (black squares), (e) graphite [94] (amber squares). $\text{Lu}_3\text{N}@C_{80}^+$ cross-section data in panel (d): Single ionization (blue circles) and double ionization (orange squares).

spectra correspond to the sum of all possible channels for ionization, excitation etc., a quantitative comparison is meaningless. However, it is surprising that the spectra for the two strongest ionization channels seem to be closer to the absorption plot of graphite than to that of C_{80} .

We find the spectral onsets of $\text{Lu}_3\text{N}@C_{80}^+$ single and double ionization (associated with K-shell excitation) at a similar energy. Cummins et al. [95] reported 284.5 eV for C_{80} . We found 285.4 eV for single and double ionization of $\text{Lu}_3\text{N}@C_{80}^+$. Cummins

et al. [95] assign K-shell excitations to unoccupied π^* levels to the C_{80} features for photon energies $E_\gamma > 290$ eV and excitations into unoccupied σ^* levels to features with $E_\gamma < 290$ eV. Terminello et al. [94] found the same distinction for fullerenes (C_{60} , C_{70}) and Graphite based on semi-empirical Hückel calculations.

With these considerations in mind, the peak features P1 and P2 in the present data might be assigned to σ^* transitions and the other resonances (appearing at higher energies) to π^* transitions. However, with several eV width, features P5 and P6 (possibly also features P4 and P7) are candidates for plasmon excitations [39]. It is difficult to identify features in the absorption spectra corresponding to these wide peaks in the present data. For example, there is no feature like P4 (at 291.5 eV) visible for graphite. The reduction of the number of resonance features could indicate a change of symmetry of the system. With the available data it is not possible to draw a conclusion on the question if the presence of the encaged molecule reduces the symmetry of C_{80} so much that the electronic structure has more similarities to bulk graphite than to a C_{80} molecule.

7.2.5. Results for higher photon energies

Beyond the carbon K edge, the product channel ($\text{Lu}_3\text{N}@C_{80}^+ \rightarrow \text{Lu}_3\text{N}@C_{80}^{2+}$) was scanned in the photon-energy range 400–435 eV. This range comprises the K-shell ionization threshold of the encapsulated nitrogen atom. The measured cross section shows, however, no structures and decrease with increasing photon energies. Additionally, the cross sections for the reactions ($\text{Lu}_3\text{N}@C_{80}^+ \rightarrow \text{Lu}_3\text{N}@C_{80}^{3+,4+}$) have been measured in the energy range 390–420 eV. These data are shown in Fig. 7.7.

Furthermore, it was also searched for signs of the M-shell threshold of lutetium in several product channels: Reactions with a singly charged initial state and final states $\text{Lu}_3\text{N}@C_{80}^{3+}$, $\text{Lu}_3\text{N}@C_{80}^{4+}$, $\text{Lu}_3\text{N}@C_{80}^{5+}$, $\text{Lu}_3\text{N}@C_{72}^{5+}$, $\text{Lu}_3\text{N}@C_{80}^{6+}$, and $\text{Lu}_3\text{N}@C_{74}^{6+}$ have been investigated in the range 1500 to 1700 eV. Figure 7.8 shows an overview of the ion yields for the four channels with the lowest statistical uncertainties and a sum of the individual spectra. Similar to the situation near the nitrogen K edge, we found cross sections lacking structures such as resonances or threshold steps.

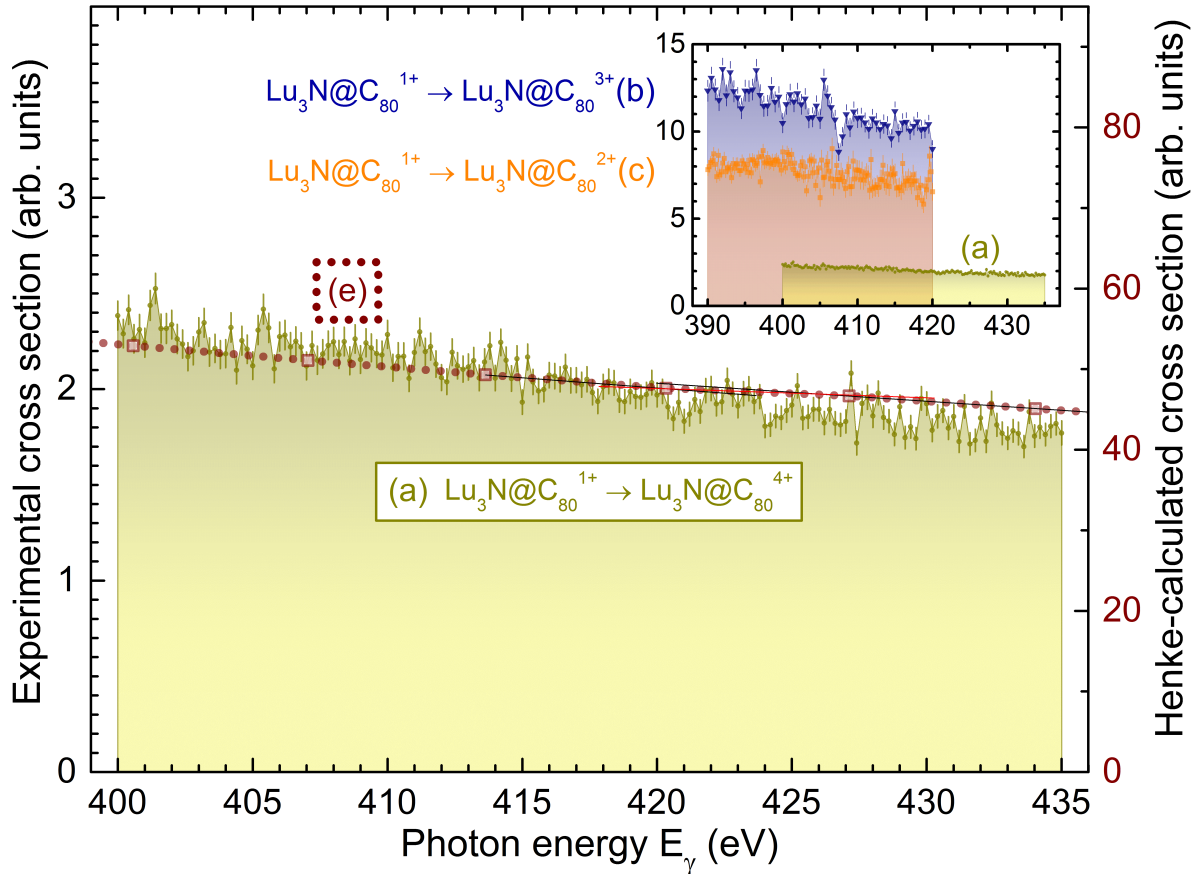


Figure 7.7.: Photoreaction cross-section spectrum for (a) $\text{Lu}_3\text{N@C}_{80}^{1+} \rightarrow \text{Lu}_3\text{N@C}_{80}^{4+}$ in the energy range 400–435 eV, amber solid circle symbols. The experimental result is compared with a prediction (e) for the nitrogen photoabsorption cross section near the K edge by Henke et al. [83] based on semiempirical calculations, dashed vine line. To guide the eye, straight lines are drawn on top of the Henke curve highlighting the mild step feature at about 420 eV. Since the height of the step feature is small, the accuracy of experimental data does not allow for a verification of the step feature associated to the nitrogen K edge. The inset shows spectra measured in further reaction channels (b) $\text{Lu}_3\text{N@C}_{80}^{1+} \rightarrow \text{Lu}_3\text{N@C}_{80}^{3+}$, blue triangle symbols, and (c) $\text{Lu}_3\text{N@C}_{80}^{1+} \rightarrow \text{Lu}_3\text{N@C}_{80}^{2+}$, orange square symbols, which cover the photon-energy range 390–420 eV.

7. Photoionization and photofragmentation of $\text{Lu}_3\text{N}@C_{80}$

The channels for finding the lutetium threshold are not exhausted: There are many ionization and/or fragmentation channels left for exploration and it is also possible that the threshold strength is distributed over many different channels including the channels we have already investigated. In consequence, the individual fraction of the total Lu M-shell oscillator strength contributing to any individual final channel of fragmentation and ionization of the primary endohedral fullerene might be too small to be easily detected.

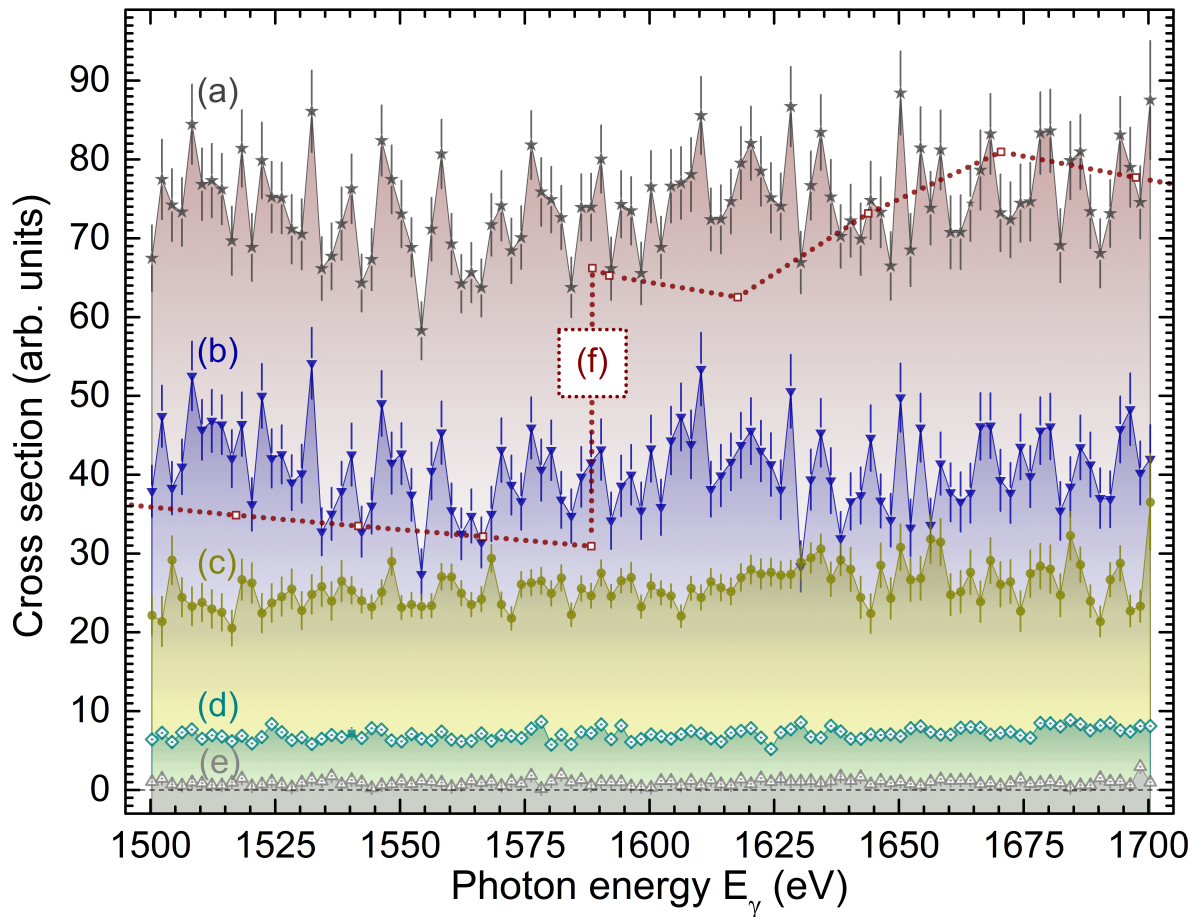


Figure 7.8.: Photoreaction cross-section spectra in the energy range 1500 to 1700 eV of the $\text{Lu}_3\text{N}@C_{80}^{1+}$ initial state. (a) gray stars: Sum of the four individual spectra b through e, (b) blue triangles: $\text{Lu}_3\text{N}@C_{80}^{3+}$ product ions, (c) amber circles: $\text{Lu}_3\text{N}@C_{80}^{4+}$ product ions, (d) hollow dark-cyan diamonds: $\text{Lu}_3\text{N}@C_{72}^{5+}$ product fragment ions, (e) hollow grey triangles: $\text{Lu}_3\text{N}@C_{74}^{6+}$ product fragment ions, and (f) dark red dotted line: Prediction for the $\text{Lu}_3\text{N}@C_{80}$ photoabsorption cross section near the M edge on the basis of the tables of Henke et al. [83]. In the measurement data there is no obvious step feature at about 1590 eV as suggested by the Henke curve.

7.2.6. Comparison with $\text{Sc}_3\text{N@C}_{80}$ measurements

In this section, photoreaction measurements of the endohedral fullerene $\text{Sc}_3\text{N@C}_{80}$ are compared to the above mentioned $\text{Lu}_3\text{N@C}_{80}$ data. The $\text{Sc}_3\text{N@C}_{80}$ photoreaction measurements were carried out at the IPB endstation using the high-energy grating in the photon energy range 275–320 eV. This energy range comprises the carbon K edge. The photon-energy resolution was 500 meV (constant resolution mode). Primary ion currents ranged from 2–8 nA. The following photoreaction channels were investigated:

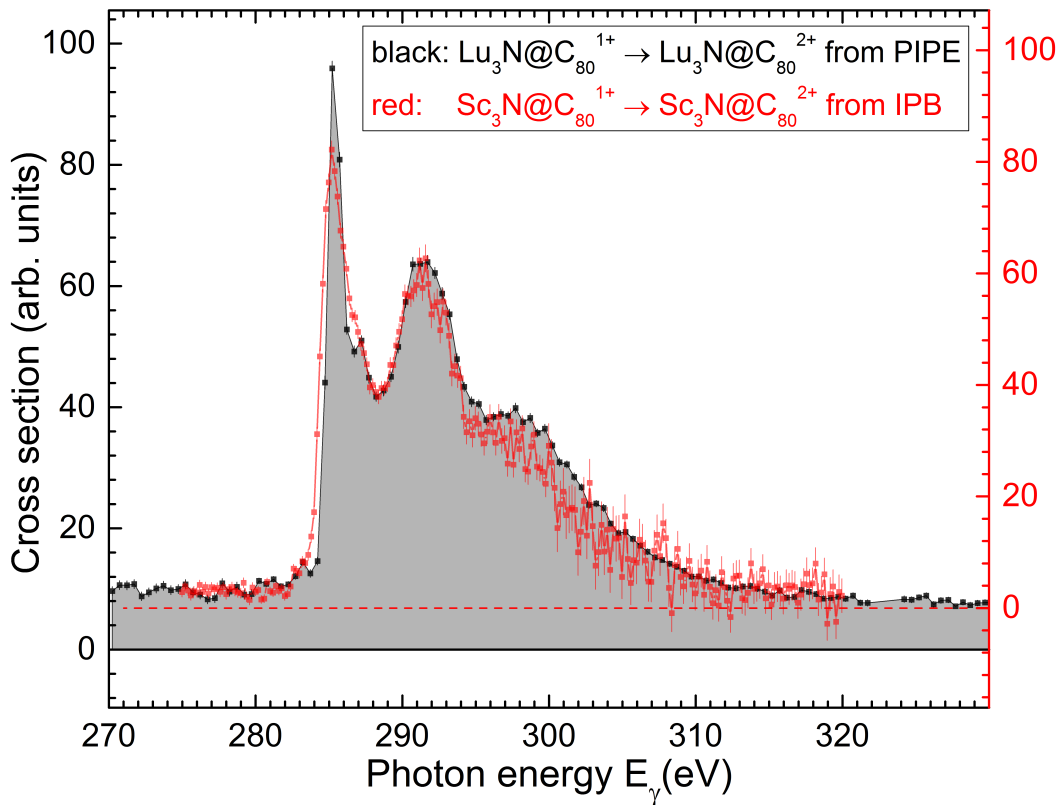
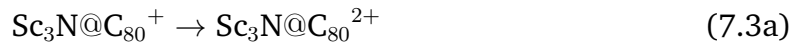


Figure 7.9.: Comparison of single photoionization cross-section spectra of $\text{Lu}_3\text{N@C}_{80}^{1+}$ measured at PIPE with $\text{Sc}_3\text{N@C}_{80}^{1+}$ measured at the IPB at photon energies around the carbon K edge. The left y axis (black) corresponds to the $\text{Lu}_3\text{N@C}_{80}^{1+}$ spectrum and the right y axis (red) corresponds to the $\text{Sc}_3\text{N@C}_{80}^{1+}$ spectrum. The horizontal dashed red line indicates $y=0$ in the $\text{Sc}_3\text{N@C}_{80}^{1+}$ spectrum.

7. Photoionization and photofragmentation of $\text{Lu}_3\text{N@C}_{80}$

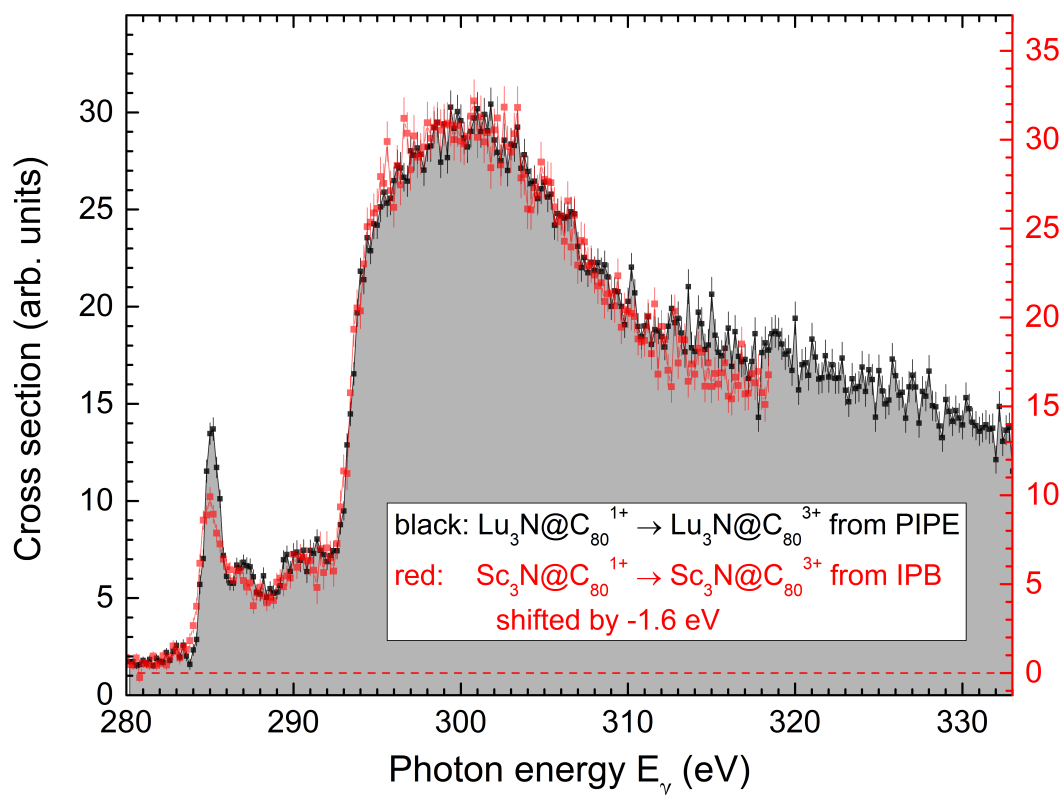


Figure 7.10.: Comparison of double photoionization cross-section spectra of $\text{Lu}_3\text{N@C}_{80}^{1+}$ measured at PIPE with $\text{Sc}_3\text{N@C}_{80}^{1+}$ measured at the IPB at photon energies around the carbon K edge. The left y axis (black) corresponds to the $\text{Lu}_3\text{N@C}_{80}^{1+}$ spectrum and the right y axis (red) corresponds to the $\text{Sc}_3\text{N@C}_{80}^{1+}$ spectrum. The horizontal dashed red line indicates $y=0$ in the $\text{Sc}_3\text{N@C}_{80}^{1+}$ spectrum.

The two strongest $\text{Sc}_3\text{N@C}_{80}$ reaction channels are shown in Figs. 7.9 and 7.10. It appears that photoionization spectra at energies around the carbon K edge are not sensitive to the type of rare-earth-element encapsulated inside the C_{80} cage. This finding supports the hypothesis that the rare-earth-element molecule is not bonding with the fullerene cage as mentioned at the beginning of this chapter and in references [77, 80]. The different widths of the peak structures at 285 eV in both reaction channels and at 292 eV in single-ionization only are a result of the different photon energy resolutions of the measurements: For the IPB measurements, the resolution was about 500 meV whereas for the PIPE measurements it was about 200 meV or better. Although the background counts have been measured separately and the data have been corrected accordingly, the cross-section offset in the photon-energy range below 284 eV is bigger for $\text{Lu}_3\text{N@C}_{80}$ photoreactions than for $\text{Sc}_3\text{N@C}_{80}$ reactions. At photon energies below the carbon K-edge, the system $\text{Lu}_3\text{N@C}_{80}$ could simply exhibit a different cross section than the system $\text{Sc}_3\text{N@C}_{80}$, thus explaining the different “background”.

8. Summary and conclusions

Synthesis of Xe@C₆₀

A subsidiary goal of the present project was to refine the means and methods for the synthesis of Xe@C₆₀ endohedral fullerene samples of the Gießen-based setup towards a more reliable production with increased endohedral fraction and process reproducibility. While the desired increase in reliability and reproducibility of the synthesis process was not fully achieved, the causes of the observed fluctuations opposing the efforts to improve the reliability have been identified. Employing a list of modifications to apparatus and methods for the synthesis, the endohedral fraction of the produced sample material could be increased by a factor of 30. The most crucial of these modifications appear to be keeping the deposited fullerene layer hot during ion bombardment on one hand and starting a sample production cycle by first depositing a visible amount of the pristine fullerenes on the substrate before starting the ion bombardment. Another crucial synthesis parameter is the kinetic ion energy which was found to be at optimum in respect to endohedral fullerene sample quality when in the range 115–140 eV. Furthermore it is expected that the usage of isotopically enriched ¹³⁶Xe and sublimed fullerene powder as starting substances for synthesis could result in an additional increase of the endohedral fraction in synthesized fullerene samples.

Triple ionization of Xe@C₆₀⁺

The investigations on triple ionization of Xe@C₆₀⁺ wanted to answer a number of questions: Is there an endohedral signature in the triple-photoionization cross section of Xe@C₆₀⁺ ions? Does this potential excess cross section exhibit confinement oscillations? How do these oscillations compare to the observations made for double photoionization of Xe@C₆₀⁺? Is the xenon-4d oscillator strength distributed among double and triple ionization of encapsulated xenon in the same proportions as it is distributed among double and triple ionization of free atomic xenon?

Triple-ionization cross-section measurements have been carried out for the reaction channels Xe@C₆₀⁺ → Xe@C₅₈⁺⁴ and Xe@C₆₀⁺ → Xe@C₅₆⁺⁴. While the shape of the endohedral-excess cross section in the latter reaction channel was found to resemble the shape common to all double-ionization reactions investigated thus far, the shape

8. Summary and conclusions

found for $\text{Xe}@C_{58}^{+4}$ products appears marginally different but practically identical within experimental uncertainty limits.

Comparing double- and triple-ionization reactions of $\text{Xe}@C_{60}^+$, one encounters a fundamental difference: For triple ionization there is hardly any cross-section contribution from the carbon cage whereas in the case of double ionization the cage contribution is roughly of the same order of magnitude as the xenon contribution in the energy range of the xenon-4d shape resonance.

With a Xe 4d oscillator strength $f = (0.46 \pm 0.12)$ in the $\text{Xe}@C_{60}^+ \rightarrow \text{Xe}@C_{58}^{+4}$ channel and almost the same amount $f = (0.50 \pm 0.18)$ in the channel $\text{Xe}@C_{60}^+ \rightarrow \text{Xe}@C_{56}^{+4}$, there was substantially less oscillator strength found in triple ionization photoreactions than what Phaneuf et al. have reported for double-ionization reactions of $\text{Xe}@C_{60}^+$ ions: The oscillator strengths of the two investigated triple ionization reaction channels account for about 25–40% of those of the corresponding (i.e., with the same degree of fragmentation) double ionization reaction channels. These branching ratios are in agreement with those reported by Becker et al. between double and triple ionization of neutral xenon. Altogether, the oscillator strength found in the six investigated photoionization reaction channels starting from $\text{Xe}@C_{60}^+$ (including one fragmentation-free reaction channel) adds up to (7.13 ± 1.66) of the total Xe 4d oscillator strength of 10.

Apparently the primary photoionization process is of crucial significance for the confinement oscillations while the secondary Auger processes resulting in, e.g., net-double or net-triple ionization are of minor relevance in this respect. That is, the confinement oscillations are the result of the interference between the incident photon, the charged carbon cage, and the xenon-4d electron emitted during the primary photoionization process.

Double ionization of $\text{Xe}@C_{60}^-$ fullerene anions

In contrast to triple ionization of $\text{Xe}@C_{60}^+$, investigations dealing with photoreactions of $\text{Xe}@C_{60}^-$ anions started with the more fundamental question if ion beams sufficiently intense for measuring cross sections could be generated and transported to the interaction region. In this situation which (apart from the sign of the charge of the parent ion) is symmetric to that of the established double ionization of $\text{Xe}@C_{60}^+$, a central question of the investigation was to look for effects of the change of the sign of the fullerene-cage charge.

Some of the further questions were in analogy to those motivating the investigation of triple ionization: Is there a signature of the encapsulated xenon atom in the cross section? How strong is the cross section in comparison to the published double ionization

results? Is the xenon cross section showing any signs of confinement oscillations? Is the shape of the cross section similar to that of the excess in double ionization?

Again closely linked to the sign of the charge: Is there an effect of due to the differently charged parent ions like, e.g., an energy shift of the cross section in comparison to the double ionization of positive ions?

Xe@C₆₀⁻ ion beams of up to 3.2 pA were generated and used for cross measurements in the reaction channels Xe@C₆₀⁻ → Xe@C₅₈⁺ and Xe@C₆₀⁻ → Xe@C₅₆⁺. The statistical quality of the measurements with endohedral fullerene anions has not reached that of positive ions. Within that accuracy, comparison with double ionization shows roughly same shape. In the reaction channel Xe@C₆₀⁻ → Xe@C₅₆⁺, a Xe-4d oscillator strength of $f = (0.66 \pm 0.17)$ was found whereas in the reaction channel Xe@C₆₀⁻ → Xe@C₆₀⁺ it accounted for $f = (0.97 \pm 0.17)$. Overall, the xenon-4d oscillator strength present in double-ionization reactions of negative fullerene ions accounts to about half the strength found in its counterparts starting with Xe@C₆₀⁺ as reported by Phaneuf et al.

While finding the same shape of the xenon-4d endohedral-excess cross section in double-ionization measurements of both positively and negatively charged Xe@C₆₀ parent ions supports the hypothesis of a charge symmetry of the system, a potential inequality in the absolute intensity of the oscillator strength opposes the symmetry hypothesis. Within the statistical uncertainty of the experimental data, an energy shift of spectral xenon-4d features could neither be verified nor could a small energy shift be unambiguously excluded when comparing double ionization measurements for Xe@C₆₀⁻ and Xe@C₆₀⁺.

On the '75-eV feature' present in various Xe@C₆₀ photoreaction channels

In all investigated photoreaction channels of both positive and negative Xe@C₆₀ endohedral fullerene ions that exhibit a signature of the encapsulated xenon, there appears to be a peak feature at a photon energy of about 75 eV. With a width of 3–5 eV, it is an order of magnitude narrower than the Xe 4d giant resonance observed for the photoionization of the free atom. This is a very prominent feature to demonstrate the redistribution of Xe oscillator strength due to its encapsulation and a benchmark for theoretical predictions. Most of the models referred to in section 5.0.2 and discussed by Phaneuf et al. [1] comprise such a feature. Phaneuf et al. were the first to demonstrate experimental evidence for the existence of this feature in double ionization with and without fragmentation of the carbon cage for Xe@C₆₀⁺ parent ions. The present experimental data for triple ionization of Xe@C₆₀⁺ and double ionization of negative fullerene ions Xe@C₆₀⁻ clearly suggest a resonance feature at 75 eV as well.

Lu₃N@C₈₀ reactions

The present work, besides the photoionization studies concentrating on Xe@C₆₀, aimed at extending the investigations towards another species of endohedral fullerenes looking for both signatures of the encapsulated atoms and their potential modifications due to the confinement inside the fullerene. The search for a suitable species of endohedral fullerenes resulted in the selection of Lu₃N@C₈₀ for the investigations. A central goal was to search for a signature of the encapsulated atoms in the photoionization cross section spectra, specifically a lutetium-3d threshold. Consecutive questions would address the potential modifications of the spectral shape of the encapsulated atoms due to confinement. Besides the effect of the confinement on the encapsulated atoms, the Lu₃N@C₈₀ study also addressed the question how the carbon cage in turn is affected by the presence of the encapsulated atoms. For this purpose, the investigations dealing with this question focused on an energy range that comprises the carbon K-shell threshold. Based upon the photoionization cross section spectra at the carbon K-edge, the Lu₃N@C₈₀ behavior was to be compared with the carbon K-edge behavior of other fullerene species.

Strong photoionization signals have been observed for single, double and triple ionization of Lu₃N@C₈₀^{+q} (q=1,2,3) in the energy region of the carbon K-shell ionization threshold (280-330 eV). To facilitate quantitative analysis of the spectral features, three prominent ionization channels (Lu₃N@C₈₀^{+1→2+,3+,4+}) have been modeled with a fitting function. A set of resonance peaks is present independently of the primary charge state but with strong variations of the intensity distribution among the peaks from channel to channel. Some of the resonances in the Lu₃N@C₈₀⁺ spectra are very broad thus indicating possible plasmonic origin.

In contrast, the ionization continuum threshold that is present in the double and triple ionization channels is shifted towards higher energies if the reaction starts from an ion in a higher charge state. Based upon the energy shift of the threshold for direct K-shell ionization, an estimate for the radius of the almost spherical Lu₃N@C₈₀ molecule could be provided: $R = (5.0 \pm 0.4) \times 10^{-10}$ m.

Comparing the present results with absorption spectra of various fullerene species in this energy range, it appears that photoionization spectra of Lu₃N@C₈₀⁺ have more similarities with the photoabsorption behavior of bulk graphite than with the photoabsorption behavior of C₈₀.

Furthermore, two reaction channels of Sc₃N@C₈₀⁺ at energies around the carbon K edge were measured at the ALS and compared to the corresponding Lu₃N@C₈₀⁺ results. Apart from the slightly deviating peak widths due to the different photon energy bandwidths during the measurements, the spectra are very similar. It appears that for photoionization of trimetaspere-type endofullerenes, the spectra at energies around

the carbon K edge are not sensitive to the type of rare-earth-element encapsulated inside the C₈₀ cage.

While carbon signatures are distinctly present, signals of the atoms encapsulated within the carbon cage could not be identified in the photoionization channels presently observed. The predicted nitrogen K-shell threshold could not be verified in the experimental data but the statistical uncertainty might conceal this weak threshold. On the other hand, several photoreaction channels with fragmented products have been scanned around the energy of the expected more pronounced lutetium M-shell threshold but the cross sections were small and free from structures. This finding supports the conjecture that possibly the whole molecular system disintegrates completely if a lutetium atom is excited by one energetic photon: Whenever a lutetium atom is M-shell excited, the amount of energy deposited and then released inside the fullerene is so big that the cage falls apart into many small fragments. Since there is a multitude of possible fragmentation channels to which the Lu M-shell oscillator strength is distributed, the lutetium contribution to each individual channel could be very small. Such a triggered radiation damage is of potential interest in various fields of applied research such as radiation biology or material science.

Outlook for Xe@C₆₀: (Conjecture) Could single ionization of endohedral ions be favored for fragmentation reactions involving the loss of three or more carbon dimers?

There are still more reaction channels of fullerenes to be explored. During the recent years, the efforts to investigate photoionization reactions of endohedral fullerenes Xe@C₆₀ mainly concentrated on double ionization channels of singly-charged positive and negative ions as well as triple ionization of singly-charged positive ions. Single ionization channels were mainly studied several years ago when the available endohedral fullerene samples yielded significantly less ion current. As a consequence of the very small primary ion currents these studies suffered from very poor statistics and did not yield significant results in the question of the ionization signatures of the encapsulated xenon atom. Furthermore, these initial studies have mainly concentrated on reaction channels without fragmentation; reaction channels involving the loss of one or two carbon dimers were only looked into very briefly while single ionization reactions accompanied by the loss of three or more carbon pairs were not studied.

An additional problem arising when studying single-ionization channels is the huge photoionization cross section of the carbon cage in these channels. Any cross-section signature of the encapsulated atom sits on top of a massive 'base line' from the cage cross section. Therefore, the relative significance of an endohedral signature can be considerably smaller in single ionization photoreaction channels than in the double

8. Summary and conclusions

and triple ionization channels shown above. If a xenon 4d feature was present in the single-ionization cross section, it would be sitting on top of a large cage cross section and would, thus, not have been easy to identify. Comparing different photoreactions of pristine fullerenes, however, one finds that the fullerene cage cross section intensities are significantly smaller in reaction channels involving the loss of more carbon pairs: The bigger the number of carbon pairs detached in a photoreaction, the smaller the fullerene cross section (Phaneuf et al. [1] have reported photoreaction cross section for intact C_{54-60} and the thesis of K. Baral [96] adds more fragments and single ionization reactions). Accordingly, investigating single ionization photoreactions of $Xe@C_{60}$ might have better prospects when focusing on channels involving the loss of several carbon pairs due to the substantially smaller cage cross section in these channels.

It is possible that single ionization might lead to new insights when looking into multiple-fragmentation reactions: Ionizing Xenon in the energy range of the 4d-giant resonance practically always results in an Auger process releasing at least one additional electron because the cross section for ionizing outer electrons is negligibly small in comparison to the (4)d-shell cross section. With the xenon atom not free but encapsulated, however, one could imagine the fullerene cage to absorb the Auger electron emitted by the xenon atom due to the high electron affinity of carbon. The energy of the absorbed electron might cause the separation of further carbon dimers C_2 from the fullerene cage.

In conclusion, it might be worth looking into single ionization photoreactions accompanied by the loss of several carbon pairs: The hope is that a reaction channel like, for example, $Xe@C_{60}^+ \rightarrow Xe@C_{52}^{2+}$ might exhibit a xenon signature on top of a comparatively small cage cross section.

9. Bibliography

- [1] R. A. Phaneuf, A. L. D. Kilcoyne, N. B. Aryal, K. K. Baral, D. A. Esteves-Macaluso, C. M. Thomas, J. Hellhund, R. Lomsadze, T. W. Gorczyca, C. P. Ballance, S. T. Manson, M. F. Hasoglu, S. Schippers, and A. Müller; *Probing confinement resonances by photoionizing Xe inside a C_{60}^+ molecular cage*. Phys. Rev. A 88 (2013) 053402.
- [2] J. Hellhund, A. Borovik, K. Holste, S. Klumpp, M. Martins, S. Ricz, S. Schippers, and A. Müller; *Photoionization and photofragmentation of multiply charged $Lu_3N@C_{80}$ ions*. Phys. Rev. A 92 (2015) 013413.
- [3] L. Horne; *Fuel for the metal worker: the role of charcoal and charcoal production in ancient metallurgy*. Expedition: The magazine of the University of Pennsylvania 25 (1982) 6–13.
- [4] P. Scharff; *New carbon materials for research and technology*. Carbon 36 (1998) 481 – 486. European Materials Research Society 1997 Meeting, Symposium A: Fullerenes and Carbon based Materials.
- [5] J. B. Howard, J. T. McKinnon, Y. Makarovsky, A. L. Lafleur, and M. E. Johnson; *Fullerenes C_{60} and C_{70} in flames*. Nature 352 (1991) 139 – 141.
- [6] H. Kroto; *Space, Stars, C_{60} , and Soot*. Science 242 (1988) 1139–1145.
- [7] E. K. Campbell, M. Holz, D. Gerlich, and J. P. Maier; *Laboratory confirmation of C_{60}^+ as the carrier of two diffuse interstellar bands*. Nature 523 (2015) 322–323.
- [8] L. Becker, R. J. Poreda, and T. E. Bunch; *Fullerenes: An extraterrestrial carbon carrier phase for noble gases*. Proc. Natl. Acad. Sci. 97 (2000) 2979–2983.
- [9] Becker, Th., Zanthier, J. v., Nevsky, A. Yu., Schwedes, Ch., Skvortsov, M. N., Walther, H., Peik, and E.; *High-resolution spectroscopy of a single In^+ ion: Progress towards an optical frequency standard*. Phys. Rev. A 63 (2001) 051802.
- [10] Y. Zhang, K. B. Ghiassi, Q. Deng, N. A. Samoylova, M. M. Olmstead, A. L. Balch, and A. A. Popov; *Synthesis and Structure of $LaSc_2N@C_s(\text{hept})-C_{80}$ with One Heptagon and Thirteen Pentagons*. Angew. Chem., Int. Ed. 54 (2015) 495–499.

9. Bibliography

- [11] J. Cioslowski and A. Nanayakkara; *Endohedral fullerites: A new class of ferroelectric materials*. Phys. Rev. Lett. 69 (1992) 2871–2873.
- [12] L. Becker, R. J. Poreda, A. G. Hunt, T. E. Bunch, and M. Rampino; *Impact event at the permian-triassic boundary: Evidence from extraterrestrial noble gases in fullerenes*. Science 291 (2001) 1530–1533.
- [13] A. Takeda, Y. Yokoyama, S. Ito, T. Miyazaki, H. Shimotani, K. Yakigaya, T. Kakiuchi, H. Sawa, H. Takagi, K. Kitazawa, and N. Dragoe; *Superconductivity of doped Ar@C₆₀*. Chem. Commun. 8 (2006) 912–914.
- [14] J. B. Melanko, M. E. Pearce, and A. K. Salem; *Nanotubes, nanorods, nanofibers, and fullerenes for nanoscale drug delivery*. In M. M. Villiers, P. Aramwit, and G. S. Kwon (eds.), *Nanotechnology in Drug Delivery*, vol. X of *Biotechnology: Pharmaceutical Aspects*, Springer New York, 105–127 (2009).
- [15] W. Harneit, C. Boehme, S. Schaefer, K. Huebener, K. Fostiropoulos, and K. Lips; *Room Temperature Electrical Detection of Spin Coherence in C₆₀*. Phys. Rev. Lett. 98 (2007) 216601.
- [16] M. J. Puska and R. M. Nieminen; *Photoabsorption of atoms inside C₆₀*. Phys. Rev. A 47 (1993) 1181–1186.
- [17] M. J. Puska and R. M. Nieminen; *Erratum: Photoabsorption of atoms inside C₆₀*. Phys. Rev. A 49 (1994) 629.
- [18] J. P. Connerade, V. K. Dolmatov, and S. T. Manson; *On the nature and origin of confinement resonances*. J. Phys. B 33 (2000) 2279–2285.
- [19] H. W. Kroto, J. R. Heath, S. C. O'Brien, R. F. Curl, and R. E. Smalley; *C₆₀: Buckminsterfullerene*. Nature 318 (1985) 162.
- [20] J. R. Heath, S. C. O'Brien, Q. Zhang, Y. Liu, R. F. Curl, F. K. Tittel, and R. E. Smalley; *Lanthanum complexes of spheroidal carbon shells*. J. Am. Chem. Soc. 107 (1985) 7779–7780.
- [21] Y. Chai, T. Guo, C. Jin, R. E. Haufler, L. P. F. Chibante, J. Fure, L. Wang, J. M. Alford, and R. E. Smalley; *Fullerenes with metals inside*. J. Phys. Chem. 95 (1991) 7564–7568.
- [22] M. Y. Amusia, A. S. Baltenkov, L. V. Chernysheva, Z. Felfli, and A. Z. Msezane; *Dramatic distortion of the 4d giant resonance by the C₆₀ fullerene shell*. J. Phys. B 38 (2005) L169–L173.
- [23] M. Y. Amusia; *Photoionization and vacancy decay of endohedral atoms*. J. Electron Spectrosc. Relat. Phenom. 161 (2007) 112 – 120.

- [24] M. Y. Amusia, A. S. Baltenkov, and L. V. Chernysheva; *Photoionization of Xe 3d electrons in molecule Xe@C₆₀: Interplay of intradoublet and confinement resonances*. Phys. Rev. A 75 (2007) 043201.
- [25] M. Amusia, A. Baltenkov, and L. Chernysheva; *Giant resonances of endohedral atoms*. JETP Letters 87 (2008) 200–203.
- [26] M. Y. Amusia, L. V. Chernysheva, and E. Z. Liverts; *Photoionization of two-shell endohedral atoms*. Phys. Rev. A 80 (2009) 032503.
- [27] M. E. Madjet, T. Renger, D. E. Hopper, M. A. McCune, H. S. Chakraborty, J.-M. Rost, and S. T. Manson; *Photoionization of Xe inside C₆₀: Atom-fullerene hybridization, giant cross-section enhancement, and correlation confinement resonances*. Phys. Rev. A 81 (2010) 013202.
- [28] Z. Chen and A. Z. Msezane; *Photoabsorption spectrum of the Sc₃N@C₈₀ molecule*. J. Phys. B 45 (2012) 235205.
- [29] T. W. Gorczyca, M. F. Hasoglu, and S. T. Manson; *Photoionization of endohedral atoms using r-matrix methods: Application to Xe@C₆₀*. Phys. Rev. A 86 (2012) 033204.
- [30] B. Li, G. O’Sullivan, and C. Dong; *Relativistic R-matrix calculation photoionization cross section of Xe and Xe@C₆₀*. J. Phys. B 46 (2013) 155203.
- [31] K. Mitsuke, T. Mori, J. Kou, Y. Haruyama, and Y. Kubozono; *4d → 4f Dipole Resonance of the Metal Atom Encapsulated in a Fullerene Cage: Ce@C₈₂*. J. Chem. Phys. 122 (2005) 064304.
- [32] K. Mitsuke, T. Mori, J. Kou, Y. Haruyama, Y. Takabayashi, and Y. Kubozono; *Photoion yield curves of Dy@C₈₂ in the vacuum UV region*. Int. J. Mass Spectrom. 243 (2005) 121 – 125.
- [33] A. Müller, S. Schippers, M. Habibi, D. Esteves, J. C. Wang, R. A. Phaneuf, A. L. D. Kilcoyne, A. Aguilar, and L. Dunsch; *Significant redistribution of Ce 4d oscillator strength observed in photoionization of endohedral Ce@C₈₂⁺ ions*. Phys. Rev. Lett. 101 (2008) 133001.
- [34] A. Müller, S. Schippers, R. A. Phaneuf, M. Habibi, D. Esteves, J. C. Wang, A. L. D. Kilcoyne, A. Aguilar, S. Yang, and L. Dunsch; *Photoionization of the endohedral fullerene ions Sc₃N@C₈₀⁺ and Ce@C₈₂⁺ by synchrotron radiation*. J. Phys.: Conf. Ser. 88 (2007) 012038.
- [35] A. Müller, S. Schippers, R. A. Phaneuf, S. Scully, E. D. Emmons, M. F. Gharaibeh, M. Habibi, A. L. D. Kilcoyne, A. Aguilar, A. S. Schlachter, L. Dunsch, S. Yang, H. S. Chakraborty, M. E. Madjet, and J. M. Rost; *Photoionization and -fragmentation of fullerene ions*. In J.-P. Connerade and A. V. Solov’yov (eds.), *Latest Advances in*

9. Bibliography

- Atomic Cluster Collisions: Structure and Dynamics from the Nuclear to the Biological Scale*. Imperial College Press, London, UK, 177–186 (2008).
- [36] A. Müller, S. Schippers, D. Esteves, M. Habibi, R. A. Phaneuf, A. L. D. Kilcoyne, A. Aguilar, and L. Dunsch; *Fullerene-encapsulated atoms in the light of synchrotron radiation*. In *AIP Conf. Proc.*, vol. 1197. vol. 1197, 103–110 (2009).
- [37] A. V. Korol and A. V. Solov'yov; *Confinement resonances in the photoionization of endohedral atoms: myth or reality?* *J. Phys. B* 43 (2010) 201004.
- [38] A. L. D. Kilcoyne, A. Aguilar, A. Müller, S. Schippers, C. Cisneros, G. Alna'Washi, N. B. Aryal, K. K. Baral, D. A. Esteves, C. M. Thomas, and R. A. Phaneuf; *Confinement Resonances in Photoionization of $Xe@C_{60}^+$* . *Phys. Rev. Lett.* 105 (2010) 213001.
- [39] S. W. J. Scully, E. D. Emmons, M. F. Gharaibeh, R. A. Phaneuf, A. L. D. Kilcoyne, A. S. Schlachter, S. Schippers, A. Müller, H. S. Chakraborty, M. E. Madjet, and J. M. Rost; *Photoexcitation of a volume plasmon in C_{60} ions*. *Phys. Rev. Lett.* 94 (2005) 065503.
- [40] S. W. J. Scully, E. D. Emmons, M. F. Gharaibeh, R. A. Phaneuf, A. L. D. Kilcoyne, A. S. Schlachter, S. Schippers, A. Müller, H. S. Chakraborty, M. E. Madjet, and J. M. Rost; *Scully et al. reply to Comment on "Photoexcitation of a volume plasmon in C_{60} ions"*. *Phys. Rev. Lett.* 98 (2007) 179602.
- [41] R. C. Bilodeau, N. D. Gibson, C. W. Walter, D. A. Esteves-Macaluso, S. Schippers, A. Müller, R. A. Phaneuf, A. Aguilar, M. Hoener, J. M. Rost, and N. Berrah; *Single-photon multiple detachment in Fullerene negative ions: Absolute ionization cross sections and the role of the extra electron*. *Phys. Rev. Lett.* 111 (2013) 043003.
- [42] R. A. Phaneuf, A. L. D. Kilcoyne, A. Müller, S. Schippers, N. Aryal, K. Baral, J. Hellhund, A. Aguilar, D. A. Esteves-Macaluso, and R. Lomsadze; *Cross-section measurements with interacting beams*. *AIP Conf. Proc.* 1545 (2013) 72–78.
- [43] A. M. Covington, A. Aguilar, I. R. Covington, M. F. Gharaibeh, G. Hinojosa, C. A. Shirley, R. A. Phaneuf, I. Álvarez, C. Cisneros, I. Dominguez-Lopez, M. M. Sant'Anna, A. S. Schlachter, B. M. McLaughlin, and A. Dalgarno; *Photoionization of Ne^+ using synchrotron radiation*. *Phys. Rev. A* 66 (2002) 062710.
- [44] G. A. Alna'washi, M. Lu, M. Habibi, R. A. Phaneuf, A. L. D. Kilcoyne, A. S. Schlachter, C. Cisneros, and B. M. McLaughlin; *Valence-shell photoionization of the chlorine-like Ca^{3+} ion*. *Phys. Rev. A* 81 (2010) 053416.
- [45] J. Bozek, A. Robinson, and S. Kellar; *New ALS beamline for high-resolution electron spectroscopy below 340 eV*. *Synchrotron Radiation News* 12 (1999) 37–39.

- [46] S. Schippers, S. Ricz, T. Buhr, A. Borovik, Jr., J. Hellhund, K. Holste, K. Huber, H.-J. Schäfer, D. Schury, S. Klumpp, K. Mertens, M. Martins, R. Flesch, G. Ulrich, E. Rühl, T. Jahnke, J. Lower, D. Metz, L. P. H. Schmidt, M. Schöffler, J. B. Williams, L. Glaser, F. Scholz, J. Seltmann, J. Viefhaus, A. Dorn, A. Wolf, J. Ullrich, and A. Müller; *Absolute cross sections for photoionization of Xe^{q+} ions ($1 \leq q \leq 5$) at the 3d ionization threshold*. J. Phys. B 47 (2014) 115602.
- [47] J. Viefhaus, F. Scholz, S. Deinert, L. Glaser, M. Ilchen, J. Seltmann, P. Walter, and F. Siewert; *The variable polarization XUV beamline P04 at PETRA III: Optics, mechanics and their performance*. Nucl. Instrum. Methods A 710 (2013) 151 – 154.
- [48] Z. Ge, J. C. Duchamp, T. Cai, H. W. Gibson, and H. C. Dorn; *Purification of Endohedral Trimetallic Nitride Fullerenes in a Single, Facile Step*. J. Am. Chem. Soc. 127 (2005) 16292–16298.
- [49] M. Saunders and R. J. Cross; *Putting Nonmetals into Fullerenes*. Springer (2003).
- [50] R. Tellgmann, N. Krawez, S.-H. Lin, I. V. Hertel, and E. E. B. Campbell; *Endohedral fullerene production*. Nature 382 (1996) 407–408.
- [51] R. Shimshi, R. J. Cross, and M. Saunders; *Beam Implantation: A New Method for Preparing Cage Molecules Containing Atoms at High Incorporation Levels*. Journal of the American Chemical Society 119 (1997) 1163–1164.
- [52] J. Rausch; *An Experimental Setup for Producing Endohedral Fullerenes: Generation of Intense Ion Beams*. Master's thesis, Justus-Liebig-Universität Gießen (2011).
- [53] J. Hellhund; *An Experimental Setup for Producing Endohedral Fullerenes: Fullerene Deposition and Infrastructure*. Master's thesis, Justus-Liebig-Universität Gießen (2011).
- [54] P. Scholz; *Testen von Betriebsparametern zur Implantation und Analyse endohedraler Fullerene*. Modulbericht (2014).
- [55] Copyright with Alban Voss; *Communication Designer*. alban.voss@mac.com Offenbach am Main, Germany (2015).
- [56] M. Saunders, H. A. Jiménez-Vázquez, R. J. Cross, and R. J. Poreda; *Stable Compounds of Helium and Neon: $He@C_{60}$ and $Ne@C_{60}$* . Science 259 (1993) 1428–1430.
- [57] R. L. Murry and G. E. Scuseria; *Theoretical Evidence for a C_{60} Window Mechanism*. Science 263 (1994) 791–793.
- [58] M. Saunders, R. J. Cross, H. A. Jiménez-Vázquez, R. Shimshi, and A. Khong; *Noble Gas Atoms Inside Fullerenes*. Science 271 (1996) 1693.

9. Bibliography

- [59] E. Campbell, R. Tellgmann, N. Krawez, and I. Hertel; *Production and LDMS characterisation of endohedral alkalifullerene films*. Journal of Physics and Chemistry of Solids 58 (1997) 1763 – 1769.
- [60] T. R. Campbell Eleanor, Hertel Ingolf; *Patent: Process for preparing endohedral fullerenes or fullerene derivatives* (1997).
- [61] I. C. Lyon, B. Peart, J. B. West, and K. Dolder; *Measurements of absolute cross sections for the photoionisation of Ba⁺ ions*. J. Phys. B 19 (1986) 4137–4147.
- [62] R. A. Phaneuf, C. C. Havener, G. H. Dunn, and A. Müller; *Merged-beams experiments in atomic and molecular physics*. Rep. Prog. Phys. 62 (1999) 1143–1180.
- [63] A. M. Covington, A. Aguilar, I. R. Covington, M. F. Gharaibeh, G. Hinojosa, C. A. Shirley, R. A. Phaneuf, I. Álvarez, C. Cisneros, I. Dominguez-Lopez, M. M. Sant’Anna, A. S. Schlachter, B. M. McLaughlin, and A. Dalgarno; *Photoionization of Ne⁺ using synchrotron radiation*. Phys. Rev. A 66 (2002) 062710.
- [64] A. Müller, S. Schippers, D. Esteves-Macaluso, M. Habibi, A. Aguilar, A. L. D. Kilcoyne, R. A. Phaneuf, C. P. Ballance, and B. M. McLaughlin; *Valence-shell photoionization of Ag-like Xe⁷⁺ ions: experiment and theory*. J. Phys. B 47 (2014) 215202.
- [65] R. Trassl; *ECR ion sources*. In F. Currell (ed.), *The Physics of Multiply and Highly Charged Ions, Vol. 1*, Kluwer Academic Publishers, Dordrecht, 3–37 (2003).
- [66] R. B. Ross, C. M. Cardona, D. M. Guldi, S. G. Sankaranarayanan, M. O. Reese, N. Kopidakis, J. Peet, B. Walker, G. C. Bazan, E. V. Keuren, B. C. Holloway, and M. Drees; *Endohedral fullerenes for organic photovoltaic devices*. Nat. Mater. 8 (2009) 208–212.
- [67] J. Fricke, A. Müller, and E. Salzborn; *Single particle counting of heavy ions with a channeltron detector*. Nucl. Instrum. Methods 175 (1980) 379–384.
- [68] K. Rinn, A. Müller, H. Eichenauer, and E. Salzborn; *Development of single-particle detectors for keV ions*. Rev. Sci. Instrum. 53 (1982) 829–837.
- [69] J. B. West and J. Morton; *Absolute photoionization cross-section tables for xenon in the VUV and the soft x-ray regions*. At. Data Nucl. Data Tables 22 (1978) 103–107.
- [70] M. Y. Amusia, A. S. Baltenkov, L. V. Chernysheva, Z. Felfli, and A. Z. Msezane; *Dramatic distortion of the 4d giant resonance by the C₆₀ fullerene shell*. J. Phys. B 38 (2005) L169–L173.
- [71] V. K. Dolmatov and S. T. Manson; *Correlation confinement resonances in photoionization of endohedral atoms: Xe@C₆₀*. J. Phys. B 41 (2008) 165001.

- [72] Z. Chen and A. Msezane; *Photoabsorption spectrum of the Xe@C₆₀ endohedral fullerene*. Eur. Phys. J. D 66 (2012) 184.
- [73] F. Penent, J. Palaudoux, P. Lablanquie, L. Andric, R. Feifel, and J. H. D. Eland; *Multielectron Spectroscopy: The Xenon 4d Hole Double Auger Decay*. Phys. Rev. Lett. 95 (2005) 083002.
- [74] U. Becker, D. Szostak, H. G. Kerkhoff, M. Kupsch, B. Langer, R. Wehlitz, A. Yagishita, and T. Hayaishi; *Subshell photoionization of Xe between 40 and 1000 eV*. Phys. Rev. A 39 (1989) 3902–3911.
- [75] J. Viefhaus, S. Cvejanović, B. Langer, T. Lischke, G. Prümper, D. Rolles, A. V. Golovin, A. N. Grum-Grzhimailo, N. M. Kabachnik, and U. Becker; *Energy and Angular Distributions of Electrons Emitted by Direct Double Auger Decay*. Phys. Rev. Lett. 92 (2004) 083001.
- [76] N. B. Aryal; *Photoionization and Photofragmentation of the Endohedral Xe@C₆₀⁺ Molecular Ion*. Ph.D. thesis, University of Nevada, Reno (2013).
- [77] S. Stevenson, G. Rice, T. Glass, K. Harich, F. Cromer, M. R. Jordan, J. Craft, E. Hadju, R. Bible, M. M. Olmstead, K. Maitra, A. J. Fisher, A. L. Balch, and H. C. Dorn; *Small-bandgap endohedral metallofullerenes in high yield and purity*. Nature 401 (1999) 55–57.
- [78] L. Dunsch and S. Yang; *Metal Nitride Cluster Fullerenes: Their Current State and Future Prospects*. Small 3 (2007) 1298–1320.
- [79] F. H. Hennrich, R. H. Michel, A. Fischer, S. Richard-Schneider, S. Gilb, M. M. Kappes, D. Fuchs, M. Bürk, K. Kobayashi, and S. Nagase; *Isolierung und Charakterisierung von C₈₀*. Angew. Chem. 108 (1996) 1839–1841.
- [80] S. Guha and K. Nakamoto; *Electronic structures and spectral properties of endohedral fullerenes*. Coordination chemistry reviews 249 (2005) 1111–1132.
- [81] R. G. Bryant; *The NMR time scale*. Journal of Chemical Education 60 (1983) 933.
- [82] S. Stevenson, M. A. Mackey, C. E. Coumbe, J. P. Phillips, B. Elliott, and L. Echegoyen; *Rapid Removal of D_{5h} Isomer Using the “Stir and Filter Approach” and Isolation of Large Quantities of Isomerically Pure Sc₃N@C₈₀ Metallic Nitride Fullerenes*. J. Am. Chem. Soc. 129 (2007) 6072–6073.
- [83] B. Henke, E. Gullikson, and J. Davis; *X-ray interactions: Photoabsorption, scattering, transmission, and reflection at e = 50 – 30,000 eV, z = 1 – 92*. At. Data Nucl. Data Tables 54 (1993) 181 – 342.

9. Bibliography

- [84] A. S. Schlachter, M. M. Sant'Anna, A. M. Covington, A. Aguilar, M. F. Gharaibeh, E. D. Emmons, S. W. J. Scully, R. A. Phaneuf, G. Hinojosa, I. Álvarez, C. Cisneros, A. Müller, and B. M. McLaughlin; *Lifetime of a K-shell vacancy in atomic carbon created by $1s \rightarrow 2p$ photoexcitation of C^+* . J. Phys. B 37 (2004) L103–L109.
- [85] A. Müller, S. Schippers, R. A. Phaneuf, S. W. J. Scully, A. Aguilar, A. M. Covington, I. Álvarez, C. Cisneros, E. D. Emmons, M. F. Gharaibeh, G. Hinojosa, A. S. Schlachter, and B. M. McLaughlin; *K-shell photoionization of ground-state Li-like carbon ions [C^{3+}]: Experiment, theory and comparison with time-reversed photorecombination*. J. Phys. B 42 (2009) 235602.
- [86] M. Oura; *Study of Inner-Shell Excitation and Relaxation Processes in Atomic and Ionic Neon by Means of Soft X-Ray Spectroscopy*. Plasma Sci. Technol. 12 (2010) 353.
- [87] A. Müller, A. Borovik, T. Buhr, J. Hellhund, K. Holste, L. D. Kilcoyne, A. S. Klumpp, M. Martins, S. Ricz, J. Viefhaus, and S. Schippers; *Observation of a Four-Electron Auger Process in Near-K-Edge Photoionization of Singly Charged Carbon Ions*. Phys. Rev. Lett. 114 (2015) 013002.
- [88] A. R. Khamatgalimov and V. I. Kovalenko; *Electronic Structure and Stability of C_{80} Fullerene IPR Isomers*. Fullerenes, Nanotubes and Carbon Nanostructures 19 (2011) 599–604.
- [89] A. V. Verkhovtsev, A. V. Korol, and A. V. Solov'yov; *Plasmon excitations in photo- and electron impact ionization of fullerenes*. J. Phys.: Conf. Ser. 438 (2013) 012011.
- [90] A. V. Verkhovtsev, A. V. Korol, and A. V. Solov'yov; *Quantum and classical features of the photoionization spectrum of C_{60}* . Phys. Rev. A 88 (2013) 043201.
- [91] R. A. Davidson; *Spectral analysis of graphs by cyclic automorphism subgroups*. Theor. Chim. Acta 58 (1981) 193–231.
- [92] E. Sohmen, J. Fink, and W. Krätschmer; *Electron energy-loss spectroscopy studies on C_{60} and C_{70} fullerite*. Z. Phys. B: Condens. Matter 86 (1992) 87–92.
- [93] S. Krummacher, M. Biermann, M. Neeb, A. Liebsch, and W. Eberhardt; *Close similarity of the electronic structure and electron correlation in gas-phase and solid C_{60}* . Phys. Rev. B 48 (1993) 8424–8429.
- [94] L. Terminello, D. Shuh, F. Himpsel, D. Lapiano-Smith, J. Stöhr, D. Bethune, and G. Meijer; *Unfilled orbitals of C_{60} and C_{70} from carbon K-shell X-ray absorption fine structure*. Chem. Phys. Lett. 182 (1991) 491 – 496.
- [95] T. R. Cummins, M. Bürk, M. Schmidt, J. F. Armbruster, D. Fuchs, P. Adelman, S. Schuppler, R. H. Michel, and M. M. Kappes; *Electronic states and molecular symmetry of the higher fullerene C_{80}* . Chem. Phys. Lett. 261 (1996) 228–233.

- [96] K. K. Baral; *Photoionization and Photofragmentation of Carbon Fullerene Molecular Ions*. Ph.D. thesis, University of Nevada, Reno (2013).

A. Appendix

Overview of endohedral fullerene samples produced

The earlier samples (Nos. 4 through 21) from this project have been discussed by Pascal Scholz [54]. Between his report and the present results, the setup was equipped with a new grid array at the thruster, a new thruster support, and new substrates. The modification enabling fast-paced substrate rotation had been finished before synthesis of sample No. 21. During testing, for none of the samples Nos. 4 through 21 an endohedral-fullerene ion current could be extracted.

Table A.1 gives a compact overview over the most important changes in operational parameters of the synthesis process and endohedral-fullerene ion currents that could be extracted from some of the samples. All successful synthesis operations have been carried out after modifying the thruster to a three-grid, 7 extraction-hole layout. Since testing of samples is time consuming, not all samples were tested.

Sample No.	Acc. voltage	Hot target	Evap. first	^{136}Xe	I_{max} ($\text{Xe}@C_{60}^+$)	I_{max} ($\text{Xe}@C_{60}^-$)
03	220 V				$\lesssim 90$ fA	n.a.
4-21	180 V				nothing	n.a.
22	81 V					n.a.
23	79 V	✓				n.a.
24	80 V	✓	✓			n.a.
25	90 V	✓	✓		** 200 fA	n.a.
26	100 V	✓	✓		* 3250 fA	980 fA
28	95 V	✓	✓		* † 21400 fA	
29	80 V	✓	✓	✓		n.a.
30	100 V	✓	✓	✓		n.a.
31	100 V	✓	✓	✓		nothing
32	95 V	✓	✓	✓		n.a.
33	95 V	✓	✓	✓	* 220 fA	320 fA
34	100 V	✓	✓	✓	* 950 fA	600 fA
35	90 V	✓	✓	✓	* ~ 100 fA	n.a.
36	85 V	✓	✓	✓		n.a.

Table A.1.: Important synthesis parameters and testing results for samples No. 22 through 36. Endohedral production run No. 27 was aborted and, therefore, not listed. When switching to using isotopically purified xenon, it was also switched to using sublimed fullerenes at the same time and, thus, is not listed separately.

*: Test results obtained with small quantities for testing.

** : The test run could not be finished due to technical issues. Therefore, the maximum test current could not be determined.

† : This result has been obtained at the ion-source test bench located in Gießen. Direct comparison to the other results is not valid.

Acknowledgements

Funding of research projects

I would like to thank the federal state of Hesse for financial support (LOEWE-Schwerpunkt ELCH). Furthermore, part of the thesis research was supported by Deutsche Forschungsgemeinschaft through grant number Mu-1068/22-1. Substantial funding from the German ministry for education and research (BMBF) has made construction and building of the PIPE setup possible. (Contracts 05KS7RG1, 05K10RG1, 05KS7GU2, and 05K10GUB within the 'Verbundforschung' funding scheme.) Furthermore, parts of this research was supported by the Chemical Sciences, Geosciences and Biosciences Division, Office of Basic Energy Sciences, Office of Science, US Department of Energy under Grant No.DE-FG02-03ER15424. Additional funding was provided by the Office of Basic Energy Sciences, US Department of Energy under Contract No. DE-AC03-76SF0098.

Synchrotron facilities

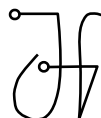
Parts of this research were carried out at the light source PETRA III at DESY, a member of the Helmholtz Association (HGF). I would like to thank J. Viefhaus, L. Glaser, F. Scholz, and J. Seltmann for assistance in using beamline P04. Furthermore, parts of this research were carried out at the Advanced Light Source at LBNL. I would like to thank David Kilcoyne and Alejandro Aguilar for their active support in using beamline BL10.0.1 and endstation BL10.0.1.1.

Closing remarks

It has been a fantastic experience and a great honor to be part of such an active research collaboration and to work and learn from outstanding researchers on both sides of the Atlantic Ocean. I would like to express my deepest gratitude towards this “constellation of four” who form the very essence of the collaboration and made the project possible. It is difficult for me to fathom and the more difficult to put in words in how many ways this experience shaped me and made me grow personally.

First I want to thank my principal doctoral advisor Prof. Dr. Alfred Müller from the Justus-Liebig-University, Gießen with whom the project commenced and who continuously supported me with infinite endurance. Furthermore I give thanks to my secondary doctoral advisor Prof. Dr. Stefan Schippers from the Justus-Liebig-University, Gießen who invaluabley guided me during the project especially in the final phase and with whom I had many inspiring conversations during numerous night shifts in Berkeley. Next I would like to thank Prof. Dr. Ron Phaneuf from the University of Nevada, Reno whose holistic support stretched far from my time in Reno. Finally I would like to thank Dr. David Kilcoyne from the Advanced Light Source, Berkeley who taught me that every problem can be tackled without hesitation and is a genius with any device. Like stated above, I have difficulties to put my gratitude into words and this list hardly is a scratch on the surface.

Additionally I would like to thank my colleagues Dr. Alexander Borovik (Jr.), M.Sc. Pascal Scholz, Dr. Jan Dreismann, Dr. Dietrich Bernhard, and Dr. Kristof Holste at the IAMP in Gießen as well as my colleagues Dr. Nagendra Aryal and Dr. Kiran Baral at UNR physics. Working with you was a pleasure! Moreover, my thanks go to Heinz-Jürgen Schäfer who zealously and actively contributed in all technical questions at the laboratory. In addition, I would like to thank the staff of the machine shop Yvonne Kluckert, Wolfgang Schmidt, Klaus Feldbusch, Peter Schneider, Joachim Weigel for the continuous collaboration. Besides, I would like to thank the administrative staff at the universities as well as at ALS and DESY front desks for smooth transitions and trouble free working, to name a few: Mercy Balderrama, Marvin Wakefield, Issa Beekun, Iris Rathgeber, Jiselle Jiles, Angel Hernandez, Barry Bain and Mark Hafner. Finally I would like to thank Alban Voss for the wonderful figures he created for this dissertation.



Versicherung

Ich erkläre:

Ich habe die vorgelegte Dissertation selbständig und ohne unerlaubte fremde Hilfe und nur mit den Hilfen angefertigt, die ich in der Dissertation angegeben habe. Alle Textstellen, die wörtlich oder sinngemäß aus veröffentlichten Schriften entnommen sind, und alle Angaben, die auf mündlichen Auskünften beruhen, sind als solche kenntlich gemacht.

Bei den von mir durchgeführten und in der Dissertation erwähnten Untersuchungen habe ich die Grundsätze guter wissenschaftlicher Praxis, wie sie in der „Satzung der Justus-Liebig-Universität Gießen zur Sicherung guter wissenschaftlicher Praxis“ niedergelegt sind, eingehalten.

Jonas Hellhund